The Role of Cd and Ga in the $Cu(In,Ga)S_2$/CdS Heterojunction Studied with X-Ray Spectroscopic Methods

vorgelegt von

Diplom-Physiker

Benjamin E. Johnson

aus Anchorage, Alaska, USA

Von der Fakultät II-Mathematik und Naturwissenschaften
der Technischen Universität Berlin
zur Erlangung des Akademischen Grades

Doktor der Naturwissenschaften
Dr. rer. nat.

genehmigte Dissertation

Promotionsausschuss:

Vorsitzende: Prof. Dr. Birgit Kanngießer
Gutachter: Prof. Dr. Norbert Esser
Gutachter: Dr. Iver Lauermann
Gutachter: Prof. Dr. rer. nat. habil. Recardo Manzke

Tag der wissenschaftlichen Aussprache: 30. August 2010

Berlin 2010

D 83

Contents

1 Introduction **5**

2 Experimental Objectives **8**

3 Details of Experimental Methods **10**
3.1 The Photoelectric Effect . . . 10
3.2 Photoelectron Spectroscopy . . . 10
3.2.1 X-Ray Photoelectron Spectroscopy . . . 10
3.2.2 Peak Positions: Chemical Shifts and Band Bending . . . 11
3.2.3 HAXPES and UPS . . . 12
3.2.4 The Electron Detector and the Work Function . . . 13
3.2.5 Analysis of Valence Band Edges measured with UPS . . . 14
3.2.6 Constant Final State . . . 15
3.2.7 Quantitative X-Ray Photoelectron Spectroscopy . . . 16
3.3 Fluorescence and Auger Processes . . . 17
3.4 X-Ray Absorption . . . 18
3.5 Inverse Photoelectron Spectroscopy . . . 22
3.6 The CISSY . . . 23
3.7 Synchrotron Radiation and BESSY II . . . 24

4 Heterojunctions and Solar Cell Basics **26**
4.1 The Schottky Contact . . . 26
4.1.1 Band Bending . . . 26
4.1.2 Fermi Level Pinning . . . 27
4.2 The Semiconductor Heterojunction . . . 28
4.2.1 Electron Affinity Rule (Anderson Model) . . . 31
4.2.2 Common Ion Rule . . . 32
4.3 The Photovoltaic Cell . . . 32
4.3.1 The Photovoltaic Cell Based on the Homojunction . . . 33
4.3.2 The Origin of the Open Circuit Voltage . . . 35
4.3.3 Solar Cell Characteristics Based on the Diode Equation . . . 36
4.3.4 The Photovoltaic Cell Based on the Heterojunction . . . 38
4.4 The Cu(In,Ga)S_2/CdS Junction and Cu(In,Ga)S_2 Thin Layer Solar Cells . 40

Results and Discussion **44**

5 $CuInS_2$-CdS Junction Formation **44**
5.1 Cd and Cu Diffusion During Chemical Bath Deposition . . . 45
5.1.1 Etching with HCl . . . 45
5.1.2 Diffusion: XPS/UPS Investigation . . . 46
5.1.3 Diffusion: HAXPES Investigation . . . 51
5.1.4 Diffusion: X-Ray Absorption Investigation . . . 55
5.1.5 Diffusion: Further Absorption and Fluorescence Experiments . . . 57
5.2 CBD-Induced Band Bending and Cd Doping in $CuInS_2$ . . . 58
5.3 Conclusions about Junction Formation . . . 65

6 $CuInS_2$ and CdS Valence Bands and the Valence Band Offset 67
6.1 The Direct and Indirect Methods of Valence Band Offset Determination (XPS/UPS and CFS) . . . 68
6.2 Linear Extrapolation . . . 70
6.3 Logarithmic Analysis . . . 74
6.4 Preliminary Cu(In,Ga)S_2-CdS and $CuGaS_2$-CdS Band Offset Investigation 76
6.5 Conclusions about the Measured Valence Band Offsets . . . 77

7 The Cu(In,Ga)S_2 Conduction Band 78
7.1 The Accessibility of the Conduction Band to Measurements . . . 78
7.2 NEXAFS . . . 79
7.2.1 Mirror Current . . . 80
7.2.2 Complementary Valence Band Meausrements . . . 80
7.3 NEXAFS Measurements . . . 82
7.3.1 Raw NEXAFS Data . . . 83
7.3.2 Material Specific Analysis . . . 84
7.3.3 Element Specific Analysis . . . 86
7.3.4 The Cu L_3 Edge After CdS Deposition . . . 94
7.4 Inverse Photoelectron Spectroscopy (IPES) . . . 95
7.5 Evidence for charging with IPES . . . 96
7.6 Conclusions About the Methods NEXAFS and IPES . . . 98
7.7 Conclusions About the Conduction Band . . . 98

8 General Aspects of Valence Band Measurements and Analysis 100
8.1 The Parabolic Band Approximation in a Semiconductor . . . 101
8.2 The Convolution . . . 104
8.3 Valence Band Comparison: He I, He II, Mg Kα and Synchrotron Radiation 107
8.3.1 XPS Au Fermi Level Measurements . . . 107
8.3.2 Mg Kα and Synchrotron Radiation . . . 109
8.3.3 Mg Kα and Ultraviolet Radiation . . . 113
8.4 Surface Photovoltage . . . 115
8.5 Conclusion: Valence Band Form . . . 117

9 Conclusion 119
9.1 Summary . . . 119
9.2 Outlook . . . 122

Appendices 124

A Raw Data for measured [Cu]/[In] Ratios During HCl etching 124

B XPS investigation of HCl-etched CIS after CdS deposition: Al Kα versus Mg Kα Excitation Energies 125

C Details of the Density Functional Calculation of Cd in CIS 126

D Logarithmic Analysis of the CIS/CdS Valence Band Offset: Inconclusive Measurements 127

The Role of Cd and Ga in the Cu(In,Ga)S_2/CdS Heterojunction Studied with X-Ray Spectroscopic Methods

Benjamin E. Johnson

Photovoltaische Zellen mit dem Aufbau Glas/Mo/Cu(In,Ga)S_2/CdS/i-ZnO/n^+-ZnO gehören zur Zeit zu den erfolgreichsten Dünnschicht Solarzellen. Dabei dient das Cu(In,Ga)S_2 (CIS) als Absorber, das CdS als Pufferschicht und das ZnO als Fensterschicht.

Das Ziel dieser Arbeit ist die Untersuchung des Cu(In,Ga)S_2/CdS Halbleiter-Heteroüberganges sowohl als Komponente dieser Solarzelle wie auch als isoliertes Materialsystem. Die Eigenschaften dieses Überganges wurden während des Herstellungsprozesses mittels chemischer Badabscheidung und nach Fertigstellung untersucht.

Dem Cu(In,Ga)S_2/CdS Übergang werden innerhalb der Solarzelle verschiedene Effekte zugeschrieben: Gitter- oder Bandanpassung zwischen Absorber und Fensterschicht, chemische Oberflächenpassivierung des Absorbers durch die Abscheidung von CdS auf CIS, wobei die Oberflächendefektdichte reduziert wird. Das Cd könnte auch das Fermi Niveau an der CIS Oberfläche fixieren oder zu einer Typinversion an der Oberfläche von p-Typ nach n-Typ führen.

Um dies zu untersuchen, wurden neben herkömmlichen Methoden wie Röntgen- und Ultraviolett-Photoelektronenspektroskopie und inverser Photoelektronenspektroskopie, auch neue Methoden zum ersten Mal auf das System angewandt. Diese waren near-UV constant final state yield spectroscopy für die Valenzbanddiskontinuität an der Grenzfläche zwischen CIS und CdS und Near Edge X-ray Absorption Fine Structure, um die Entwicklung der Lage der CIGS Leitungsbandkante mit zunehmendem Ga-Gehalt zu verfolgen. Dazu wurden die Vor- und Nachteile der etablierten und neuen Methoden gegenübergestellt und diskutiert.

Es wurde festgestellt, dass die Deposition von CdS weder das Fermi Niveau an einer Position der CIS Oberfläche fixiert, die wichtig ist für die Solarzelle, noch die Oberfläche dotiert obwohl eine Cd-haltige CIS Schicht (CIS:Cd) durch die Abscheidung gebildet wird. Da sie in HCl unlöslich ist, kann es sich nicht um CdS handeln. Weil vermutet wird, dass sich Cd im CIS auf Kationenplätzen befindet, höchstwahrscheinlich auf Cu-Leerstellen, sollten die Cd-S Bindungen im CIS anders als im CdS sein, weil sich CdS in HCl leicht lösen lässt. Weitere Experimente konnten nicht ausschließen, dass Cd in das CIS hineindiffundiert, konnten aber wohl zeigen, dass Cu vom CIS in das CdS hineindiffundiert, die Oberfläche einer normalen $\sim$35 nm CdS Pufferschicht aber nicht erreicht.

Die Valenzbanddiskontinutität zwischen CIGS und CdS war unabhängig von Ga-Gehalt und betrug 1.35 eV$\pm$0.20 eV. Die Lage des Leitungsbandes wies wiederum eine Ga-Abhängigkeit auf und verschob sich zu niedrigeren Bindungsenergien hin mit zunehmendem Ga-Gehalt. $\sim$8% Ga an der CIGS Oberfläche weitete die Oberflächenbandlücke des Materials um $\sim$150 meV auf, bezogen auf reines CIS. Diese Bandaufweitung verschlechtert die Leitungsbandanpassung zwischen CIGS und CdS, obwohl die Beimischung von Ga die Leerlaufspannung der Solarzelle um $\sim$100 mV erhöht.

1 Introduction

The most promising solar cells currently in production and which are also the subject of much scientific research are thin layer solar cells composed of two, three, or in certain cases even more semiconductor layers of thickness ranging from nm to μm. In these cells, the metallurgical junctions between the layers are most often heterojunctions and are of supreme importance to the solar cell, as they often define many of the cell's characteristics [1]. An understanding of how these junctions are formed and how they function is, therefore, vital to the understanding of the entire cell. And the characteristics of these junctions are, in turn, defined by the surfaces of the semiconductors forming them and require a surface sensitive measuring tool for their investigation. Photoelectron spectroscopy (PES) lends itself well to this purpose because both electronic and stoichiometric information can be obtained in a single measurement, allowing the direct correlation of the observed characteristics of the system.

The investigation of semiconductor heterojunctions with PES and related methods for solar cell applications, therefore, contains elements of three different, yet complimentary fields. Material science, photoelectron spectroscopy and solar energy, while all individually influential and important fields, stand to become even more interesting and relevant as a subject of scientific attention when combined. This means that a subject fusing these elements is both of pure scientific interest: what is a semiconductor heterojunction and how does it work? What is PES and what are we actually measuring when we perform measurements? And of immediate practical use: understanding and improving solar cells.

But why thin layer solar cells?

The reasons why new energy sources which take us away from oil, gas and coal need to be investigated and developed are many and can be found daily in any media source of choice. Alternatives include wind, wave and solar energy, each of which has unique characteristics leading to different energy sources being suitable for different situations. It is, therefore, undeniable that we need a mix of these energy sources to cover our current and future needs. That is, of course, barring the discovery of the miracle energy source such as a highly efficient mechanism for splitting water [2, 3].

The current effort to produce these energy sources revolves around two objectives: Efficiency up. Costs down.

And the field of solar energy is no exception. Research on thin layer solar cells has led to progress in both of these aspects, although mostly to the lowering of costs as the efficiency of thin layer solar cells have only recently become comparable to that of crystalline Si solar cells [4, 5]. While some thin layer solar cells benefit from simple production, all conventional thin layer solar cells have one advantage over Si: reduced material costs due to the smaller amounts of material needed. This usually stems from a very high optical absorption coefficient, due in part to many thin film absorbers possessing a direct band gap.

The subject of this thesis, the thin layer solar cell with the structure Glass/Mo/$CuInS_2$/CdS/i-

ZnO/n^+-ZnO supports this trend. And although other chalcopyrite-based solar cells consistently outperform this one in terms of efficiency, most notably the cell based on $Cu(In,Ga)Se_2$ technology, the costs and ease of preparation of the $Cu(In,Ga)S_2$-based solar cells, especially in light of the 11% efficiency attainable with them, keeps them competitive in the marketplace.

But therein lies, again, the beauty of the combination of the three fields involved in this thesis. The research presented here was not only done to improve the $Cu(In,Ga)S_2$-based solar cell, but also to understand why this cell does not work as well as its counterparts. To many in industry, the moderate efficiency of this cell has rendered it uninteresting. However, from a research standpoint, the reason why the cell does not work as well as its counterparts, although it has a band gap close to the theoretical optimum for a solar cell [6], is exactly the reason *why it is* interesting.

For this reason one of the two main semiconductor heterojunctions found in the $Cu(In,Ga)S_2$-based solar cell, the $Cu(In,Ga)S_2$/CdS junction, is the focus of this thesis. The following chapters explain how the junction forms and what diffusion processes take place between the constituent parts and what influence they have on the completed junction. This is covered by the ability of PES to investigate elemental concentrations and changes in them. Also, the electronic changes of the semiconductor surfaces comprising the junction during this formation are studied by the electronic sensitivity of PES.

After formation, the ability of the junction to function within the solar cell is investigated by looking at the positions of the conduction and valence bands on each side of the interface and attempting to correlate them with stoichiometric changes in $Cu(In,Ga)S_2$.

But make no mistake, the observation of this junction as a component of a solar cell or as an object of interest for material science are intertwined. It has not been attempted here to favor one field of study over the other. There are results which have no current application to solar cells but are purely of interest from a material science stand point. These results may find value in other projects unrelated to solar cells, but where it is vital to understand how one complicated material system, a semiconductor surface, interacts with another semiconductor surface to form a transition from one material to another.

The remaining field of study mentioned above is photoelectron spectroscopy. This field of study, as with the other two, has its own distinct points of intrigue and difficulties.

What actually happens during a PES experiment is not clarified. We make a measurement of a system in an excited (ionized) state and yet wish to know the characteristics of the ground state of the material. How does the excited state of the system effect the binding energies of the measured core levels? Are all core levels effected in the same way? To what extent are we justified in applying our results to other experiments where the information is obtained from a different excited state of the material?

In this spirit, a considerable amount of this work is dedicated to comparing a single system studied with several different PES methods in order to observe which differences emerge. As with the aspects of material science, these experiments are performed on the

$Cu(In,Ga)S_2/CdS$ junction, but the results and implications are not meant to be contained within the arena of this system. They are meant instead to explore the method of PES itself.

As will be seen in the following chapters, one of the greatest challenges during this thesis was the known non-reproducibility of the $Cu(In,Ga)S_2/CdS$ junction, stemming from both the $Cu(In,Ga)S_2$ absorber surfaces and the method of junction production as well as the previously mentioned difficulties with the interpretation of PES experiments. This reality often leads to qualitative results as specific values may be correct for a certain sample, but they do not describe the system as a general entity. This reality had to be accepted and dealt with for what it was, but does, at times, lead to disappointing conclusions when specific values would lead to answers to important questions about the nature of the junction.

In spite of this, progress was made in the understanding of the $Cu(In,Ga)S_2/CdS$ as a semiconductor heterojunction as well as a component of a thin layer solar cell. In addition, progress was also made in understanding the method of photoelectron spectroscopy as pertains to this system, but also as a method unto itself.

On this note, however, the funding for this project as well as the reason for its creation comes directly from the field of solar energy and our need for alternative energy sources. It must be said then, that human greed and man's inability to regulate himself have so far done more to drive us into this dire situation than research such as this has been able to do to get us out.

As unwilling as many are to face this reality, it does mean that the way forward must not only consist of painstaking scientific research, but must also come from the knowledge that the largest steps forward which we can take are already available to us.

The next section describes in more scientific detail the experimental objectives of the investigation of the $CuInS_2/CdS$ junction during and after formation as well as its function in the solar cell.

2 Experimental Objectives

The main experimental objectives of this thesis are:

1) To investigate which diffusion processes are at work during the formation of the $CuInS_2$/CdS junction formed through chemical bath deposition of the CdS and the extent to which these processes effect the characteristics of the junction (Chapter 5).

2) To determine the valence band offsets between Cu(In,Ga)S_2 and CdS and whether Ga has an effect on this offset. An improvement on accuracy of already existing measurements is also sought (Chapter 6).

3) To determine the conduction band offsets between Cu(In,Ga)S_2 and CdS and whether Ga has an effect on this offset (Chapter 7).

4) To offer a new picture of the Cu(In,Ga)S_2/CdS junction under consideration of the above three points.

As of now, it is thought that Cu diffuses into the CdS during the formation of the Cu(In,Ga)S_2/CdS junction and that Cd may diffuse into the Cu(In,Ga)S_2, although the depth of the diffusion has yet to be ascertained. Experiments have already shown that in the Cu(In,Ga)Se_2/CdS system, a Cd-containing layer is deposited on the Cu(In,Ga)Se_2 surface during junction formation which, unlike CdS, cannot be etched away in HCl. For the system under study here, this is of interest because it is thought that Cd occupies a Cu lattice position when in or on the Cu(In,Ga)S_2, meaning that the Cd is also bound to the Cu(In,Ga)S_2 surface through a Cd-S bond. These Cd-S bonds would be different than those found in CdS if a similar non-soluble layer is found on Cu(In,Ga)S_2.

The actual role of the Cd after it has bonded to the Cu(In,Ga)S_2 surface or diffused into the Cu(In,Ga)S_2 is not known. One possibility is that the Cd dopes the Cu(In,Ga)S_2 n-type. This would be very plausible if the Cd indeed occupied a Cu lattice position in the Cu(In,Ga)S_2. The Cu species found in Cu(In,Ga)S_2 is Cu(I), whereas the Cd in CdS is Cd(II), meaning that Cd would act as a donor after being incorporated into the Cu(In,Ga)S_2 lattice.

Another possibility is that Cd forms a thin layer on the Cu(In,Ga)S_2 surface and pins the Cu(In,Ga)S_2 surface, thereby forcing the Fermi Level to a certain electronic position. This would influence the band bending on the Cu(In,Ga)S_2 surface and may determine where the position n=p is in the solar cell, thereby influencing recombination mechanisms in the completed solar cell.

Any surface band bending, whether it is caused by Cd or another component of the chemical bath during deposition, such as NH_3, may also effect the band offsets.

It is known that the valence band offset between the two materials is in the range 1.20 eV, causing a step in the conduction band edge, assuming bulk band gap values for the surface. The conduction band offset is of prime importance because the absorber in this solar cell is p-type, making the electrons, which are transported in the conduction band, the minority carriers which determine the characteristics of a solar cell. Therefore, of necessity when trying to understand the solar cell based on Cu(In,Ga)S_2 is whether the Ga concentration at the junction effects the position of the Cu(In,Ga)S_2 valence and/or conduction band edges and whether these changes influence the offsets between either band edge at the Cu(In,Ga)S_2/CdS interface. Also, the addition of Ga raises the open circuit voltage (V_{oc}) of the solar cell by $\sim$100 mV.

The conventional method of determining valence band offsets is cumbersome and involves many measurements of valence band edges and core levels leading to mounting error with each measurement. This is especially critical for the Cu(In,Ga)S_2/CdS system because it is known that the reproducibility of both materials is problematic. Of great value then, would be a method which could probe the valence band edge positions of both materials with a single measurement, thereby determining the valence band offset directly. The problem here, though, is to ensure complete coverage of the Cu(In,Ga)S_2, a relatively thick CdS layer ($\sim$5 nm) is needed, at which point conventional UPS excitation energies can no longer be used to probe the substrate. However, because the inelastic mean free path of electrons grows with decreasing electron kinetic energies after a minimum around 50 eV, depending on the material, a method using low excitation energies could be employed.

While optical and quantum efficiency measurements have shown a widening of the Cu(In,Ga)S_2 band gap by about 125 meV, it is not yet known which band edge accommodates this change. In the Cu(In,Ga)Se_2 system, most of the change in band gap with Ga concentration has been attributed to a shift in the position of the conduction band edge and, thus, effects mostly the conduction band offset.

Because conduction band offsets are often determined by adding the materials' bulk band gaps to valence band offsets, it would be beneficial to measure the position of the conduction bands with surface sensitive methods. This is of great importance for Cu(In,Ga)S_2, where concentration gradients are known to exist which have been shown to affect an opening of the band gap from bulk to surface. However, because the conduction band contains unoccupied states, it cannot be measured easily. Furthermore, the methods available using photoelectron spectroscopy to probe the conduction band states may bring the system noticeably out of the ground state, adding uncertainty to the measurements because an inference back to the ground state must be made. It may, however, be possible in certain cases where the excited states of two materials are similar to see real relative changes in the position of the conduction band with these methods. Although the absolute position of the conduction band edge is more desirable, any relative change should be able to be correlated to relative changes in solar cells made with the corresponding materials. Specifically, changes in E_g should effect the V_{oc}.

If this correlation is not possible, it may be necessary to offer a new electronic and stoichiometric picture of the Cu(In,Ga)S_2/CdS junction.

3 Details of Experimental Methods

3.1 The Photoelectric Effect

Most every experimental method used in this thesis revolves in some way around photoelectron ionization (photoelectric effect), described first by Einstein through the following equation, shown here in modern form [7]:

$$E_K = h\nu - E_B - \Phi \tag{1}$$

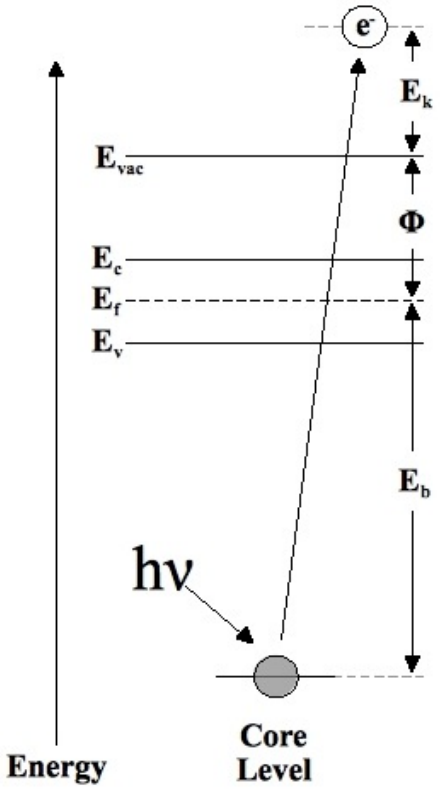


Figure 1: Schematic diagram of the photoelectric effect and XPS. See text for explanation.

Energy is thus imparted to a bound electron through the absorption of an impinging photon with energy hν. If the photon energy is high enough to fully ionize the atom, the resulting kinetic energy (E_K) of the photoelectron can be calculated by subtracting the binding energy, E_B, of the electron and the work function, Φ, of the material of interest from the photon energy, $h\nu$ (fig. 1). It is shown, however, in [8] for example, that the work function effecting the energetic positions of the spectral features in experiments involving photoelectron spectroscopy is that of the detector itself; the work function of the sample only effects the position of the secondary electron edge. This makes it possible to directly compare spectra of samples (when displayed in binding energy) with different work functions because the only value in eq. 1 which changes is E_B, which is, of course, the value of interest when doing electronic experiments.

Due to the fact that a vast source of literature on the subject of photoelectron spectroscopy already exists, there is no need to go into detail here, although the exact methods used in this work will be shortly discussed below. Essential experimental details pertaining to the experiments themselves and why a certain method was chosen for a particular experiment will be discussed at the beginning of each results section. Further details pertaining to photoelectron spectroscopic methods can be found in [9, 10, 11].

3.2 Photoelectron Spectroscopy

3.2.1 X-Ray Photoelectron Spectroscopy

The direct detection of the photoelectrons leaving a solid is referred to as X-ray photoelectron spectroscopy (XPS) or simply photoelectron spectroscopy (PES). These electrons, in

order to be analyzed using eq. 1, cannot lose kinetic energy when traveling to the surface of the solid, that is, they may only engage in elastic collisions with other (quasi)particles in the solid before entering the electron analyzer. Electrons suffering random inelastic collisions will contribute only to background. The average distance covered by an electron before being scattered inelastically is given by the electron mean free path (MFP) and is defined to be the distance in a solid after which a signal is reduced by a factor of $1/e$. The MFPs in this work were calculated using the computer program Quases-Tourgaard [12]. The information depth, on the other hand, is the depth out of which 90% of the detected signal comes. Thus, the information depth is equal to approximately 2 times the MFP, although it must be kept in mind that the overwhelming majority of the signal comes from the sample surface.

In the laboratory, two excitation energies are generally available for XPS from an X-ray tube: Mg Kα (1253.6 eV) and Al Kα (1486.6 eV). The maximum electron inelastic mean free paths using these two energies are, for both CIS and CdS, about 2.4 and 2.8 nm, respectively [12]. It is thereby seen, that spectroscopic experiments using excitation energies in this range (100-2000 eV), sometimes referred to as soft X-rays, are relatively surface sensitive.

The energy resolution of these two sources is in the sub eV range. Specifically, the line widths for Mg Kα and Al Kα are 0.68 eV and 0.83 eV, respectively, although monochromators can be used to reduce these values to under 0.20 eV [9, 10].

Other energies in the soft X-ray regime available through the use of synchrotrons, such as on the U41 at BESSY (sec. 3.7), may have slightly higher or lower resolutions depending on the chosen settings of the beam line. Like with Mg Kα and Al Kα, the overall resolution of a measurement depends on the line width of the excitation energy, that of the electron analyzer and the intrinsic line width of the measured peak in the following way, assuming all contributions are Gaussian in form:

$$\Delta E \sim (\Delta E_{ex}^2 + \Delta E_{an}^2 + \Delta E_{in}^2)^{1/2} \tag{2}$$

ΔE_{ex}, ΔE_{an} and ΔE_{in} being the line width of the excitation energy, of the analyzer and intrinsic line width of the measured peak, respectively. ΔE_{an} can often be neglected with modern detectors, making ΔE_{ex} all the more important because ΔE_{in} obviously cannot be changed [9].

Eq. 2 and the measured peak shape are more fully discussed in chapter 8.

3.2.2 Peak Positions: Chemical Shifts and Band Bending

Because of the chemically and electronically sensitive nature of XPS as well as it's surface sensitivity, the method is very well suited for semiconductor surface and junction analysis including band bending (discussed in sec. 4.1) taking place during junction formation. The changes in band bending are often brought about by a surface treatment such as a wet chemical deposition of another semiconductor allowing charge transfer to take place. It is

often the case, however, that this same deposition will also change the surface stoichiometry and, therefore, the surface chemistry of the sample. Because the local chemistry of a material determines the binding energies of the elements in that region, band bending caused by a wet chemical deposition process may also be accompanied by a change in binding energies due to the change in the local chemistry of the sample. In this case the two changes in binding energy from band bending and chemical shifts will be overlapped and may be very difficult to disentangle.

The compromise between resolution and information depth of soft X-rays makes XPS suitable for investigations involving concentrations on sample surfaces by using integrated peak areas (see sec. 3.2.7) or electronics, including band bending and chemical shifts due to surface treatments, by monitoring peak positions and shifts. Moreover, the integrated peak area and the peak position are both contained in one XPS measurement making possible the direct correlation of these two values as well as their mutual evolution.

A complete investigation of these characteristics, however, often demands an expanded use of PES.

3.2.3 HAXPES and UPS

Energetically above and below the soft X-rays are two slightly different realms of PES.

Experiments using higher energies (>2000 eV) are often referred to as hard X-ray photoelectron spectroscopy (HAXPES). Results presented here involving energies between 2030 eV and 6000 eV were made on the HIKE end station at the KMC-1 beamline at the BESSY II synchrotron in Berlin (sec. 3.7). HAXPES measurements boast an increased information depth due to the resulting high kinetic energies of the photoelectrons. Information depths up to ∼20 nm can be reached and thereby depth dependent information such as concentration profiles (see sec. 3.2.7) can be measured. The cost of the high energies is usually a loss of resolution, making the acquisition of electronic information sometimes difficult. However, special high energy beam lines are available which have resolutions of several hundred meV or less at distinct excitation energies, making these hard X-ray apertures very competitive, especially because the high energies allow access to an increased number of core levels (see HIKE, sec. 3.7) [13].

Energies lower than 100 eV mark the ultraviolet (UV) range of PES, the method using this range being referred to commonly as ultraviolet photoelectron spectroscopy (UPS). In contrast to HAXPES, this range of energies is marked by very low information depths, yet often very high resolutions. The most common energies in this region are 21.22 eV and 40.82 eV from He I and He II emission lines, obtainable from a common UV lamp. The resolution of the He I and He II sources are 3 meV and 17 meV, respectively, allowing for very exact measurements of the valence region, especially of the valence band edge [10]. Although all but the most shallow core levels lie too deep to be measured with these energies, much chemical and electronic information can be gleaned from valence band measurements.

Similarly to the soft X-ray region, tunable UV light is available at many synchrotrons with somewhat wider line shapes.

3.2.4 The Electron Detector and the Work Function

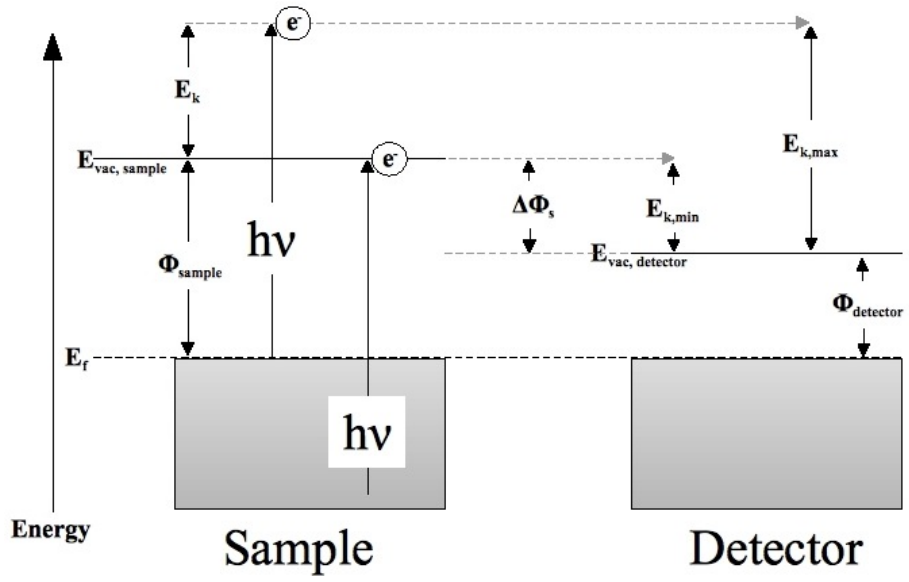


Figure 2: Schematic diagram showing the photoionization process and the resulting photoelectron entering the detector [8]

UPS can also be used to directly measure the work function, Φ, of a material. The reason for this, as discussed in [8], is that although all electrons are affected by the difference between the work functions of the sample and the detector, $\Delta\Phi_s = \Phi_{sample} - \Phi_{detector}$, in that they gain kinetic energy by an amount equal to $\Delta\Phi_s$, all photoelectrons from a single sample above the secondary electron edge will be effected in the same way ensuring that all spectral features remain fixed relative to one another. This can be seen in fig. 2 for the simplified case of a metal.

When comparing two different samples, the electrons with the same binding energy, independent of the sample and its work function, will have the same amount of kinetic energy, $E = E_k + \Delta\Phi_s$ with $E_{k,min} \leq E \leq E_{k,max}$, after entering the detector. $\Delta\Phi_s$ is different for all samples having different work functions and thus compensates for the difference in E_k between electrons having the same binding energy but coming from samples with different work functions.

This makes the comparison of spectra (in binding energy) from different samples possible because binding energy is defined in reference to the Fermi Level and the electrons making up the Fermi Level have the highest kinetic energy when leaving the sample and will always have energy $E_{k,max}$ (sample independent!) after entering the detector.

It can be seen then, that the electrons of the secondary electron edge, which is made up of electrons leaving the sample with zero kinetic energy, are also effected by $\Delta\Phi_s$, keeping them energetically at the correct position relative to other spectral features. The position of the edge itself, however, is determined by the sample's work function alone: the electrons must first leave the solid in order to be effected by the difference in work functions, that is, to gain the energy $\Delta\Phi_s$.

The equation for the calculation of a sample's work function is (independent of the detector work function!):

$$\Phi_{sample} = E_{cutoff} + h\nu - E_f - V_{bias} \tag{3}$$

where E_{cutoff} is the position of the secondary electron cutoff, $h\nu$ the excitation energy, E_f the Fermi Level and V_{bias} a potential often applied to the sample to improve the UPS signal by "drawing out" the low kinetic energy electrons, especially those making up the secondary electron cutoff.

3.2.5 Analysis of Valence Band Edges measured with UPS

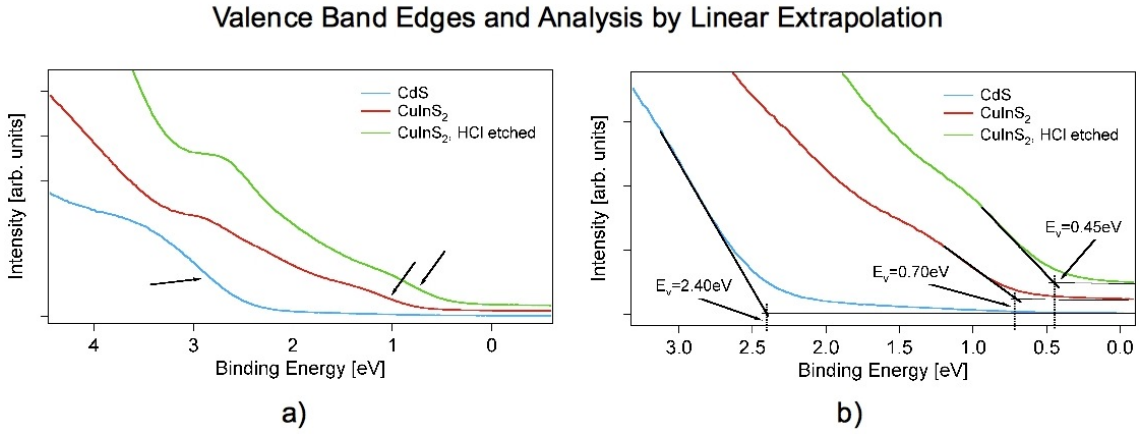


Figure 3: The valence band edges of CdS, $CuInS_2$ and HCl-etched $CuInS_2$ measured with He I. In a) a general view of the bands are shown with arrows indicating the linear portion of the band considered to be the valence band edge. b) shows a detail of the band edges with the linear extrapolation method used to determine the binding energy of the valence band edge.

The valence band edges of CIS and CdS, most often measured with UPS, were measured and analyzed in this thesis many times under different conditions. The method of determination of the position of the band edge was to extrapolate the last linear portion of the band as shown in fig. 3. The position at which the extrapolated line crossed a linear extrapolation of the background signal was the position of the valence band edge. Although this method is routinely found in literature, there are physical reasons which

can both justify and denounce its use. Some of the these reasons are discussed in the thesis, especially in secs. 6.2, 6.3 and chapter 8, where other methods of analysis are explored.

Figs. 3 a) and b) show the valence band edges of CIS and CdS with a blow-up of the actual edge region to show exactly which structure was used to determine the position of the valence band edge of each material.

Due to the sensitivity of band shape and signal intensity to the geometry between the sample and electron analyzer, it was necessary to normalize valence band spectra in figures containing more than one valence band in such away that all important features of all spectra could be clearly seen. Because valence band spectra were not used for quantitative studies the normalization has no effect on the information contained in the spectra because electronic positions remain unaffected. Although in the rest of the thesis, all valence band spectra have a common background signal, an additional vertical shift has been added to fig. 3 for clarity.

3.2.6 Constant Final State

An exception to the above remark about the low information depths in UPS can be seen immediately in fig. 4. At an excitation energy of about 10 eV, the MFP of the photoelectrons is equal to that of Mg Kα and Al Kα and continues to rise toward lower excitation energies. Although at these energies one is only able to measure the valence band edges of semiconductors, the energy is high enough, when combined with the high information depth, to make direct measurements of valence band offsets in semiconductor junctions (see chapter 6). The reason for the rising MFP is that the electrons have fewer interactions at these low energies with the surrounding lattice (plasmons).

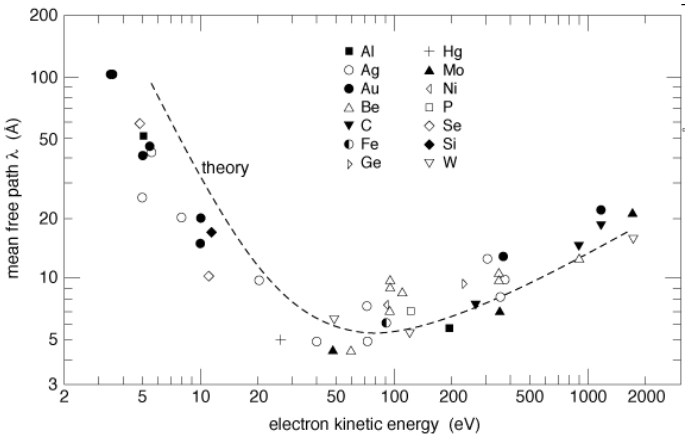


Figure 4: The universal curve of electron mean free paths taken from [14]. The deviation from the theoretical curve can clearly be seen.

One method which directly exploits the low kinetic energy/high information depth side of the universal curve of electron mean free paths, fig. 4, is near-UV constant final state yield spectroscopy (CFS). The name refers to the fact that as the excitation energy is changed the detector energy stays constant, i.e. the kinetic energy of the detected photoelectrons is always the same.

This method uses a xenon high-pressure lamp in combination with a grating monochromator to produce continuously varying radiation between 7.5 and 4.0 eV.

CFS is ideal for valence band and band offset investigations because of the high information depth offered by the resulting kinetic energies and because the constant final state allows for an investigation of the valence band densities of states without a convolution with the conduction band. This will be discussed further in sec 6.1.

3.2.7 Quantitative X-Ray Photoelectron Spectroscopy

Quantitative XPS refers to an analysis method of XPS. As mentioned already, the integrated peak area from an XPS spectrum contains information about the concentrations of each element in a sample. The signal is, however, augmented in several ways and must therefore be corrected using the following factors:

n: the number of scans or slices, n, done during a measurement will not only smooth the peak, but will also increase the perceived intensity of the signal.

I_0: this signal is a measure of the primary beam strength during the measurement. For example, the ring current in a synchrotron steadily declines after injection and measurements done at different times can only be compared after they are normalized with I_0. This signal is obtained in different ways on different beam lines. For XPS experiments using the beam line U41 with the CISSY aperture at BESSY (see description, sec 3.6, 3.7), I_0 was recorded as a mirror current from the ionization on the last re-focusing mirror, whereas with HAXPES experiments on HIKE (sec. 3.7), I_0 was recorded using a N_2 ionization chamber.

$1/\alpha$: if α is the absorption length of an electron with a certain energy, then $1/\alpha = MFP$, the mean free path of the electron. As discussed previously, electrons with different binding energies, when excited with light of the same wavelength, will have different resulting kinetic energies and will thus be able to travel different distances in a solid without suffering an inelastic collision. Normalizing peak intensities with the MFP helps to account for the fact that electrons with lower binding energies are able to come from a larger volume of the solid. Tricks can be made using different excitation energies so that the resulting photoelectrons have the same kinetic energy and thereby the same MFP. The MFPs in this thesis were calculated theoretically using the program Quases-Tourgaard [12].

T(E): the transmission function of the analyzer describes how the analyzer is more sensitive to certain energies than others. This function is not trivial to determine although it is sometimes possible to find experimentally or can be described by a polynomial. By changing excitation energies, the resulting kinetic energy of photoelectrons can be tuned so that electrons with different binding energies will be effected in the same way by the transmission function.

$\sigma(\theta)$: the angle dependent ionization cross section describes the probability that a photon of a certain energy will be absorbed by an electron in a certain shell of a certain atom, the angle dependence referring to the angle of electron emission. The cross sections used in this thesis were calculated from [15] which defines ways of calculating $\sigma(\theta)$ for non-polarized, linearly polarized, elliptically polarized and circularly polarized light in the dipole and quadrupole approximations for XPS and HAXPES experiments, respectively.

Other reliable calculations can also be found in [16]. The general formula of the cross sections are given in terms of four factors, σ, β,γ and δ. γ and δ only appear in the quadrupole approximation and the terms containing these variables are zero when using the HIKE end station due to the right angle between X-ray beam and electron analyzer and will, for that reason, be excluded here.

The dipole equation for unpolarized light is [15]:

$$d\sigma_i/d\Omega = \sigma_i/4\pi[1 + \beta/2(3cos^2(\theta) - 1)] \tag{4}$$

where $d\sigma_i/d\Omega$ is the differential cross section per solid angle and θ is the angle between the wave vectors, k, of the incoming photon and the emitted photoelectron. Because the electron contributing to the photoelectron count rate must necessarily be detected by the electron analyzer, the direction of the k vector of the electron must correspond to the position of the analyzer itself.

If $\theta = 54.76°$, the angle is referred to as the "magic angle" because the term in parenthesis in eq. 4 is equal to zero. In the case of the CISSY (sec. 3.6), the angle between X-ray source and detector is approximately the magic angle.

After these five values have been obtained, the normalized peak intensity is simply calculated by the equation:

$$I_{Norm} = I_{Meas} \cdot (\alpha/I_0 \cdot n \cdot T(E) \cdot d\sigma_i/d\Omega) \tag{5}$$

where I_{Meas} is the measured peak intensity obtained through fitting (see chapter 8)

The normalized peak intensities can then be analyzed as ratios in order to determine sample stoichiometry.

3.3 Fluorescence and Auger Processes

After the absorption of a photon, the excited electron leaves behind a positively charged core hole which can result in several processes. One of the electrons bound at a lower binding energy can, through a dipole transition, relax into the hole, causing the release of a photon whose energy is equal to the difference between the two states: $h\nu = E_f - E_i$.

This photon can then be absorbed by another electron, referred to as a secondary electron, which is, in turn, excited out of the system as an Auger electron. These secondary photoelectrons, because they are excited by a photon with the same energy from a system-internal relaxation, will always have the same resulting kinetic energy, independent of the primary excitation energy. If photoelectron spectra from one sample taken with increasing excitation energies are plotted versus kinetic energy as most raw data are, the Auger structures, having always the same kinetic energy, will remain at one position while the

features corresponding to fixed electronic states will move to higher kinetic energies because of the increased excitation energy. If then, the spectra are plotted versus binding energy by subtracting the kinetic energy from the excitation energy, as per eq. 1, the features corresponding to fixed electronic states will naturally remain at their corresponding binding energies in the plots, while the Auger features will be seen to "wander" to ever higher binding energies. This is of course an artifact because the Auger structures have, strictly speaking, no binding energy. Nevertheless, a binding energy can be calculated with eq. 1.

Auger processes are very chemically sensitive since they involve in many cases an electron from the valence band as well as a core level position.

Alternatively, the photon, $h\nu = E_i - E_f$, can itself leave the system without being absorbed, a process referred to as X-ray emission or fluorescence. Due to the fact that X-rays interact with matter much less than do electrons, the MFP of the photon is much larger than that of an electron. Fluorescence signals can be used to probe samples to depths of $1.5\,\mu$m at photon energies of 1500 eV [17].

An important point can be made here:

> *The limited information depth of XPS is due to the limited MFP of the electrons and not of the impinging photons.*

When making measurements using both fluorescence and electron signals, one can immediately draw conclusions as to the homogeneity of the elemental concentrations being measured. Although fluorescence only found limited use in this project, the process of creating a core hole leads to another experimental method used in several sections of this thesis.

3.4 X-Ray Absorption

Until now, the absorption of an impinging photon on an atom has led to the ionization of the atom with the resulting primary photoelectron leaving the system and contributing to a PES signal. However, the absorption of photons, and thus, the excitation of atoms in a system can begin before the primary photoelectrons can reach the vacuum level if the sample has unoccupied states below E_{vac}. In a semiconductor these states build the conduction band. The experimental method charged with analyzing absorption process is referred to as X-Ray Absorption Spectroscopy (XAS).

The most general form of XAS is to use transmission. Here, the impinging beam intensity is measured directly before and after the sample, the difference in the intensities being the absorption due to the sample at a specific photon energy.

There are, however, other methods of detection available. In this work, two signal sources were routinely used, the first being fluorescence, the origin of which was described in the

previous section. The second signal source was sample current, or total electron yield and measures all electrons which leave the solid, primary and secondary. The common characteristic linking transmission, fluorescence and sample current is that they all begin when a core hole is created by the absorption of a photon and for this reason, they are all proportional to the absorption in a sample.

Sample current is more surface sensitive than fluorescence and varies with excitation energy because of the much lower MFP of electrons in condensed matter, even when allowing the electrons to suffer inelastic collisions. The estimated information depth will be discussed with every experiment.

Another possibility for measuring absorption is to use the electron analyzer. Either one can set the detection energy to the corresponding Auger energy of the excitation in question, the information depth being determined by the kinetic energy of the auger electron, or one can vary the detected kinetic energy. High kinetic energies (the Auger energy being the maximum kinetic energy) will be surface sensitive because the electrons can lose but little energy before exiting the solid. As the detection energy is lowered the electrons will be able to suffer more and more inelastic collisions while still being able to exit the sample and be counted by the analyzer, thereby increasing the information depth. Although this detection signal is theoretically possible, its practical feasibility is another matter.

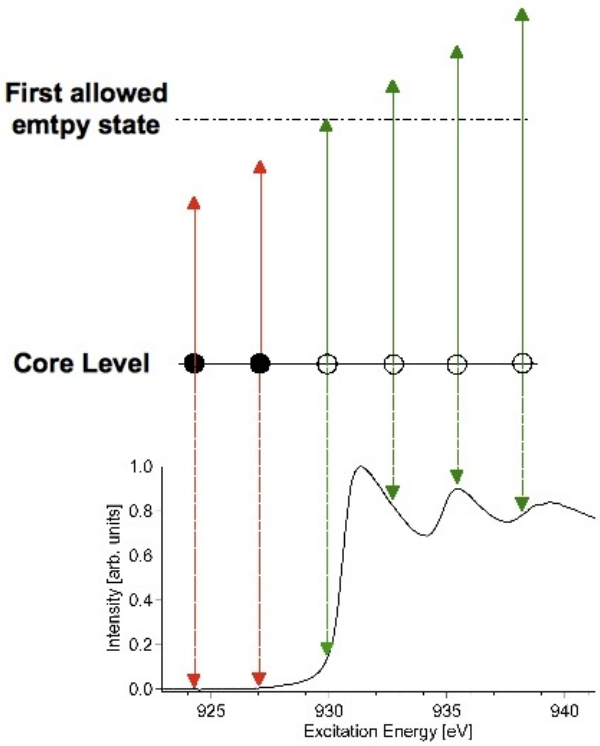


Figure 5: Schematic diagram of the absorption process leading to a NEXAFS spectrum: as the excitation energy is increased a core level electron is excited into the first allowed, empty state, the green arrows indicating a photon energy able to affect the excitation. The core hole left behind after the absorption allows Auger processes to create a heightened background, detectable in total electron yield mode.

Spectra resulting from these signals can generally be broken down into two regions. The first contains the absorption edge itself together with the immediate region after the edge and is called near-edge X-ray absorption fine structure (NEXAFS), seen schematically in fig. 5. After the NEXAFS region comes a region referred to as extended X-ray absorption fine structure (EXAFS). The boundary separating the two regions is somewhat arbitrary and varies between elements and absorption edges. In many cases the boundary between NEXAFS and EXAFS is set by the goal of the measurement itself.

NEXAFS is very sensitive to the chemical state of the system, the position of the absorption edge equaling the energy difference between the excited core level and the first

allowed, empty state of the conduction band. Thus, NEXAFS is a powerful tool for identifying an element in a specific phase which may not be easily determined with, for example, XPS. A good example of this is Cu_2S and CuS, discussed in more detail in chapter 5 and in [18].

Studies of electronic states can also be performed with NEXAFS, most importantly the unoccupied states of the conduction band. A duo of rules formulated by [19, 20] called the *initial state rule* and *final state rule* helps to illuminate this. First, however it is important to define what "initial" and "final" states refer to when considering NEXAFS.

NEXAFS is the absorption of a photon and the excitation of an electron into the conduction band, the initial state of the system being, therefore, the ground state of the system before the excitation. The final state is then after the absorption event where the system is in an excited state and in the presence of a core hole.

Thus, the *initial state rule*, formulated for NEXAFS, states:

> *The integrated X-ray transition intensity is determined by the total number of valence states in the initial state, i.e. prior to the X-ray transition.*

The *final state rule* states, on the other hand:

> *The spectral features reflect eigenstates of the final state Hamiltonian. In the case of [NEXAFS] a core hole is present in the final state. The influence of the core hole may be very different for different systems.*

This means that NEXAFS can be used to probe the density of unoccupied states as they exist in the ground state, without a core hole, as follows from the initial state rule. However, the energetic positions of these states (spectral features) are not necessarily those positions found in the ground state (final state rule). Thus, the region immediately following the absorption edge contains information about the local densities of states (LDOS) seen by the excited atom in the ground state and LDOS calculations can be compared to measurements to determine conduction band composition. The position of the edge, however, does not necessarily correspond to the energy of the conduction band edge, not only due to possible band distortion from the core hole, but also due to NEXAFS measuring specific LDOS which may not contain the states at the bottom of the conduction band (conduction band edge). The difference, ΔE, between the conduction band edge and a specific absorption edge is not trivial to determine and is specific to each system as it clearly depends on specific material properties.

When determining the densities of states of the conduction band, a complete set of edges, for example K and $L_{2,3}$, $L_{1,2,3}$ or L_1 and $M_{2,3}$, are needed because of the dipole nature of

the electron's excitation, described by the dipole transition rule $\Delta l = \pm 1$ [21].[1]

Interestingly, it is also shown in [19], that the excited atom, Z, can often be replaced theoretically by another atom, Z+1, in order to correct for the core hole.

Referring back to the initial and final state rules to complete the picture, XPS initial and final states are the same as those of NEXAFS, making measured core level binding energies comparable to NEXAFS spectra as will be more fully discussed in chapter 7. This is important because the absorption edge identifies the energy difference between the two states involved in the transition and if the energy of one of the states can be measured, the energy of the other state can be calculated.

To complete the picture now, X-ray emission spectroscopy (XES), which uses fluorescence as detection signal, can be used to gather valence band information. In contrast to absorption, the core hole is in the initial state, meaning that densities of states measured by XES are those of the excited state, however, the final state has only a valence hole if the core hole is filled by electrons from the valence band. Electronic positions in XES valence band spectra can be compared with UPS valence band spectra because the latter also contains a valence hole in the final state.

Sources [18, 19, 20, 21] give together a good general description of the electronic and chemical experiments possible with NEXAFS, especially as pertains to Cu, which is very important in this work. And although [21] deals with Cu(In,Ga)Se_2, its results can easily be generalized to the $CuInS_2$ system.

NEXAFS can also be used to study lattice structures, albeit in a rather indirect way, in order to further identify and characterize different phases of a material. Using the modeling program FEFF, one can generate NEXAFS spectra from defined lattice structures and compare these theoretical results with the experimentally determined absorption edges [22]. In order to achieve this, one must have some idea of what the sample lattice structure is like and this structure is then defined and input into the FEFF program. The program then calculates specific absorption spectra at a chosen energy through a multiple scattering approach using self consistent, or overlapping, atomic potentials (for FEFF8) [23]. The problem is solved by trial and error as a new lattice must be defined for every new attempt if the previous resulting calculation does not fit the measured data. This has also been briefly attempted in this work, although structural studies are usually left to the realm of EXAFS.

The EXAFS region is made up of the long wave-like structures extending for several hundred eV past the initial absorption edge. EXAFS is usually done with a material's K absorption edge because the structures making up the EXAFS must be uninterrupted in order to ensure a successful transformation to reciprocal space. The K edges of most of the materials considered in this thesis are the only edge sufficiently energetically sepa-

[1] The K-edge refers to the quantum number n=1 or 1s shell. The L-edge refers to the quantum number n=2 so that the L_1, L_2 and L_3 edges correspond to the 2s, $2p_{1/2}$ and $2p_{3/2}$ shells, respectively. The M edge refers to n=3 so that the M_1, M_2, M_3, M_4 and M_5 edges correspond to the 3s, $3p_{1/2}$, $3p_{3/2}$, $3d_{3/2}$ and $3d_{5/2}$ shells, respectively. This scheme continues *ad nauseam*.

rated from other bound states to make this possible. L and M edges, being in regions of higher densities of states, are interrupted by other absorption edges of the same atom or by absorption edges of another element in the material.

The waves, or variations in intensity in EXAFS come from the fact that with higher and higher excitation energy, the resulting photoelectrons posses a shorter and shorter de Broglie wavelength, as is evident from the quantum mechanical formulation of the energy for a free electron $E = h^2k^2/m = h\nu = h^2/\lambda$.

Some of the electrons emitted from the excited atom will be reflected from the neighboring atoms, which are oriented regularly around the excited atom in the lattice. Depending on the distance to the neighboring atoms and the wave length of the electron, the signal will be subjected to constructive or destructive interference. Of course, because there are many neighboring atoms, there will be many overlapping signals. A Fourier transformation of this signal combined with a modeled Fourier transformation from a program such as Artemis can show atomic distances around the central atom and and be compared to known bonding lengths to determine the immediate environment of the atom in question [24].

The difference between the two calculations is that in the case of NEXAFS, a self-consistent potential must be calculated, whereas with EXAFS the reciprocal space curve can be generated exactly from the user-defined lattice.

3.5 Inverse Photoelectron Spectroscopy

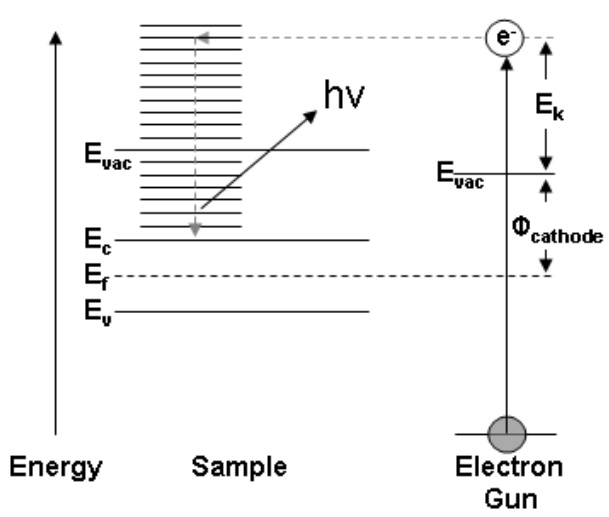


Figure 6: Schematic diagram of the IPES process. Injected electrons couple with the sample through the conduction band states above E_{vac} and emit a photon through de-excitation into the lower conduction.

Like NEXAFS, inverse photoelectron spectroscopy (IPES) is a method enabling the investigation of unoccupied states in a solid. Because IPES "setups" are not commercially available as they are for XPS, the description of the method here will concentrate on the variation built by J. Wüsten at the Universität Kaiserslautern [25].

The method revolves around the injection of electrons of varying kinetic energy from an electron gun into unoccupied conduction band states of the sample above the vacuum level (fig. 6). These electrons can then relax down to lower unoccupied states below the vacuum level through the release of a photon, very similar to fluorescence described in sec. 3.3.

The photons can then be detected by one of two methods. The system used here consisted of a $SrFl_2$ low pass window filter

($E_{max,photon}$=∼9.7 eV) and a NaCl covered cone ($E_{ionization}$=∼9.2 eV) as high pass solid state filter photocathode. Thus, only photons with energies 9.2 eV< $h\nu$ <9.7 eV can contribute to the signal by entering the channel electron multiplier positioned directly after the cone.

The second method also involves a $SrFl_2$ low pass window filter and as a high pass filter a Geiger-Müller counter filled with iodine gas and the carrier gas argon [26]. The iodine has an ionization energy $E_{ionization}$=∼9.2 eV, making the energy window in this case the same as in the first, although different materials can be used in order to augment the pass energies. Because this energy window essentially defines the resolution of the system, it can be seen that in many cases the fine structure of the conduction band will not be resolvable as is the case with the valence band and UPS.

The Geiger-Müller system is characterized by a slightly better signal-to-noise ratio than the solid state system, as can be seen through a comparison of the spectra in this work and in [26]. The advantage of the solid state photocathode is, however, that there is no pressure regulation as is necessary with the ionization of the I_2.

Other aspects of the system such as sample charging will be discussed with the results of the IPES experiments in sec. 7.4.

3.6 The CISSY

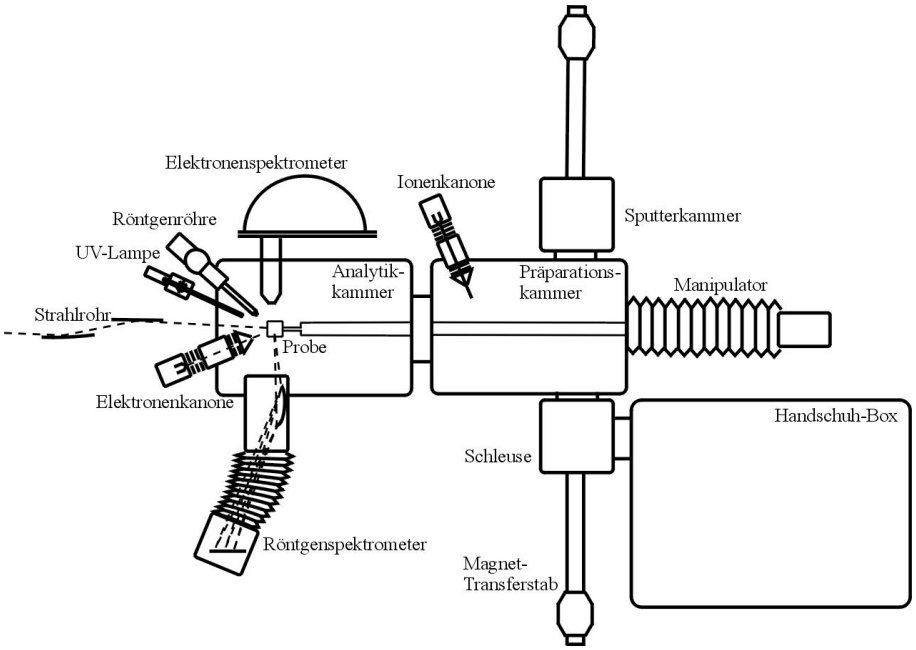


Figure 7: The CISSY vacuum chamber. Taken from [27].

Most laboratory experiments in this work involving XPS and UPS were done using the CISSY (derived from "CIS+Synchrotron") vacuum chamber, two radiation sources, an XR-50 X-ray source and a UVS 10/35 UV source from Specs and a photoelectron ana-

lyzer from VG. The CISSY, seen in fig. 7 is a multifaceted machine capable of in-situ analysis of solar cell components, due to its attached sputter chamber (Sputterkammer) and N_2-filled glove box (Handschuhbox), from both of which an anaerobic transfer is possible through the preparation chamber into the analysis chamber for characterization [27].

The main vacuum chamber, consisting of the afore mentioned preparation chamber (Präparationskammer), analysis chamber (Analytikkammer) and load-lock chamber (Schleuse), boasts typical working pressures in the range of $5.0\text{x}10^{-9}$-$5.0\text{x}10^{-8}$mbar. The reason for this rather high pressure is that much of the work done with the CISSY involves characterization of samples following different surface treatments, some of which necessitate the repeated extraction and reloading of the sample. The increased frequency of sample transfer leads directly to the stated pressure although directly after bake-out the CISSY comes comfortably into 10^{-10} mbar region.

The CISSY can also be used as a synchrotron end station (Strahlrohr). Specifically, the CISSY is used regularly on the U41-PGM at BESSY II.

3.7 Synchrotron Radiation and BESSY II

The advent of the use of synchrotron radiation in the 1950s and the subsequent construction and widespread use of machines designed exclusively to produce synchrotron radiation, commonly called synchrotrons, have revolutionized the field of photoelectron spectroscopy. A synchrotron, consisting often of an inner ring (the synchrotron) and an outer storage ring to which the end stations are actually attached via beamlines, produces a radiation continuum by forcing electron packets into a circular orbit. The normal mode of operation is, thus, through the use of this dipole radiation although insertion devices, such as wigglers, can also be used which force the electrons into an additional undulating path, thereby increasing the flux of the radiation at certain energies.

Because the electrons are moving near-relativistically, the radiation they emit will travel at a right angle to the direction of acceleration and be confined to a narrow cone with a 0.1 mrad angular divergence [11]. This means that the observer sees only a short burst of radiation once every time the electron packet passes on its orbit. This produces the radiation used for experiments in pulses which can be as short as picoseconds. The use of monochromators makes it possible to select desired wavelengths from this emission which are suitable for specific experiments.

The main advantages of a tunable light source are core electron excitation near threshold, variation of ionization cross sections, variation of the information depth and photons polarized in the plane of the electron orbit [28]. The continuous spectrum itself also makes methods such as NEXAFS, CFS, constant initial state (CIS) and depth profiling possible in a general sense. The other advantage to synchrotrons is the sheer energy available at certain facilities where over 100 keV can sometimes be reached at resolutions high enough to still enable experimentation. Increased beam brilliance is also advantageous for experiments involving low ionization cross sections.

Although every synchrotron will have its individual characteristics, the types of experiments possible are just as dependent on the characteristics of the beamline and end station used, that is, the type of monochromator and detector, for example, are beamline and end station specific and usually allow only certain features of the synchrotron to be exploited.

Further information on synchrotrons can be found in [11, 28] and the the specifics of the BESSY II synchrotron and its end stations can be found at [29]. In this work synchrotron experiments were performed with the CISSY end station on the U41-PGM beamline, the SurICat end station on the Optics Beamline and the HIKE end station on the beamline KMC-1.

4 Heterojunctions and Solar Cell Basics

4.1 The Schottky Contact

The description of metal-semiconductor junctions began in the 1930s with the investigation of the Schottky Contact [30, 31, 32]. Although the junction discussed in this work is a semiconductor-semiconductor heterojunction, there are several important concepts used to characterize the heterojunction which are more easily described using a Schottky Contact. These concepts will now be introduced before moving on to the description of the semiconductor heterojunction.

4.1.1 Band Bending

Band bending describes a depletion or enrichment region in a semiconductor causing a change in the position of the Fermi Level within the band gap and, thus, in the binding energy of the electronic levels in this region because binding energies are measured from the Fermi Level.

In fig. 8 for the case of an ideal metal-semiconductor junction (no interface states), where the latter is p-type, the Fermi Level of the metal was at lower potential energies than that of the semiconductor before contact. Charges, in this case electrons, move from the metal into the p-type semiconductor until the Fermi Levels coincide [33]. It can also be understood that holes flow from the semiconductor into the metal. Thus, a depletion region for a p-type semiconductor is created, meaning that the Fermi Level moves toward the conduction band edge in this region.
The position of the Fermi Level relative to the band edges reflects the concentration of mobile charge carries at the band edges. This is shown mathematically for the holes through [34]:

$$p = N_v e^{((E_v - E_f)/kT)} \tag{6}$$

where N_v is the equivalent density of states of the valence band, E_v the energetic position of the valence band edge, k Boltzmann's constant and T the temperature.

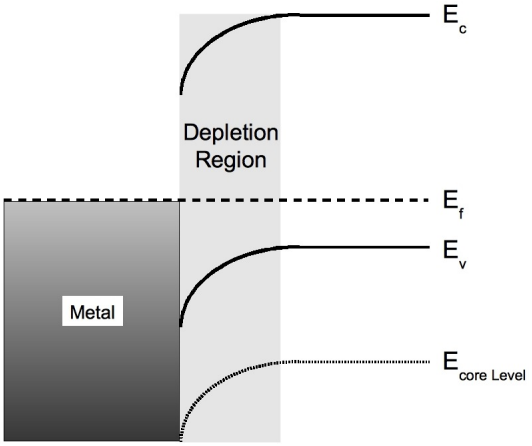


Figure 8: A depletion region in a junction with a p-type semiconductor and a metal. The change in the position of E_f effects not only the binding energy of the conduction and valence band edges, but also that of the core levels.

In a semiconductor not in a junction, intrinsic surface band bending may be present if the holes move to the surface and leave behind the compensating negative charge in the depletion region while the surface becomes positively charged.
Also, as will be described in sec. 4.3.1, the electrical contacting of two differently doped semiconductors can also bring about these diffusion processes.

As can be seen in the figure here, the shift of the Fermi Level affects not only the binding energies of the conduction and valence band edges, but also that of the core levels of the material. Changes in band bending can, therefore, be identified through parallel shifts in the measured binding energies of all elements in a sample (sec.).

4.1.2 Fermi Level Pinning

One phenomenon which is sometimes observed while investigating band bending and surface treatments is called Fermi Level Pinning. This often comes into play when one takes into account the interface states which may come about through metal-semiconductor or semiconductor-semiconductor junction formation which causes defect states at the interface which lie in the band gap.

In the case of a metal-(p-type) semiconductor junction, these surface states are generally confined to several atomic layers and have a defined energy with respect to the valence and conduction bands of the semiconductor. The states can have a conduction band or valence band "character" which corresponds to an acceptor and donator type defect state, respectively. The former state is negative when filled and neutral when empty, whereas the latter state is neutral when filled and positive when empty.

The position of the Fermi Level at the interface will be that which achieves charge neutrality in the junction. If the position of the Fermi Level does not achieve charge neutrality between the interfaces states, this charge must be compensated by the charge in the space charge region (in this case the depletion region), leading to a change in band bending. However, if the density of interface states is high enough ($\sim 10^{15}(\mathrm{eV})^{-1}\mathrm{cm}^{-2}$), a small change in the position of the Fermi Level can no longer be compensated through the space charge region and the Fermi Level is pinned at the position where the total charge of the interface states is practically zero.

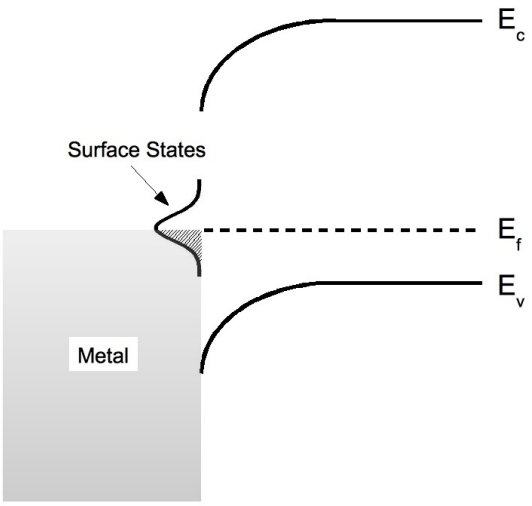


Figure 9: Surface states in a metal-semiconductor junction, filled below the Fermi Level. If the density of these states is high enough ($\sim 10^{15}(\mathrm{eV})^{-1}\mathrm{cm}^{-2}$), they can pin the Fermi Level at a certain position on the semiconductor surface.

A change in doping of the semiconductor or an applied bias across the junction will then have little effect (1-10 meV) on the position of the Fermi Level in the semiconductor band gap [35].

If such surface states exist before the deposition of another material and are not removed during the deposition process, there may be no change in Fermi Level position, although charge transfer takes place between the two materials. This is because the amount of charge contained in the surface states is much greater than the transfered charge.

If the deposition process creates such states at the interface, thereby pinning the Fermi Level at a certain position on the surface of the substrate material, one would expect these states to be created with every deposition and that the Fermi Level would be consistently pinned at the same position. A discussion of this important phenomenon is carried out in chapter 5.

4.2 The Semiconductor Heterojunction

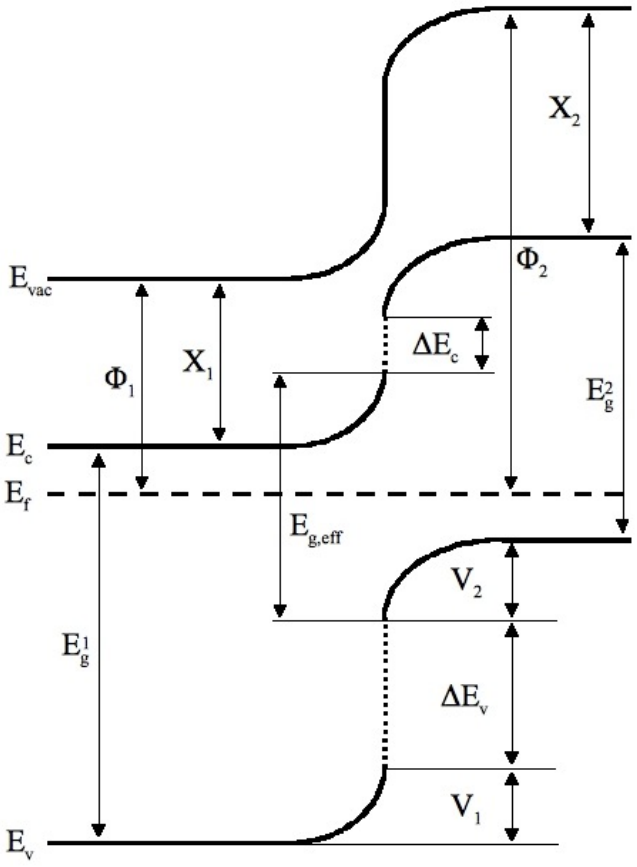


Figure 10: Schematic diagram of a semiconductor-semiconductor heterojunction. The explanation of the symbols is found in the text.

A semiconductor-semiconductor junction is the metallurgical joining of two different semiconductor materials creating electrical contact and allowing diffusion processes to take place.

The key characteristic defining and differentiating a heterojunction from a homojunction is the presence of a discontinuity between either the conduction bands, ΔE_c, or valence bands, ΔE_v, or both, of the two materials forming the junction. Whereas a homojunction is formed from two differently doped pieces or sections of one material resulting in no band discontinuities (Fig. 13), the heterojunction is a metallurgical junction forged from two materials of differing chemical make-up, or stoichiometry. Fig. 10 shows a heterojunction and several properties of the two semiconductors involved. All such diagrams in this thesis illustrating band bending and band offsets are implicitly assumed to have a vertical energy axis and a horizontal position axis. For simplicity these axes have been left away. Such diagrams are very common in the field of photovoltaics and find use in many publications on the subject, including many cited in this thesis.

In the fig. 11, E_g^i are the energy gaps, Φ_i the work functions, V_i the respective amounts of band bending in each semiconductor, χ_i the electron affinities, ΔE_i the band offsets and $E_{g,eff}$ the effective band gap. The following equation can be read off from the figure:

$$\Delta E_v - \Delta E_c = E_g^1 - E_g^2 = \Delta E_g \tag{7}$$

meaning that the knowledge of one band offset and both band gaps allows the calculation of the second offset [36].

The band discontinuities, dependent on the specific chemistry between the two materials in the junction, play a central role in determining the transport characteristics[2] of the resulting device and are, thus, of the highest importance for junction characterization. And therein lies the main hurdle to the understanding of heterojunctions: there is no easy way to predict what the band line-up between two semiconductors may be and simplistic as well as sophisticated models often fail to give results in agreement with experiment or to provide proper physical reasoning for the predicted result. In addition, there is no single universally accepted measurement method; all methods have their advantages and drawbacks.

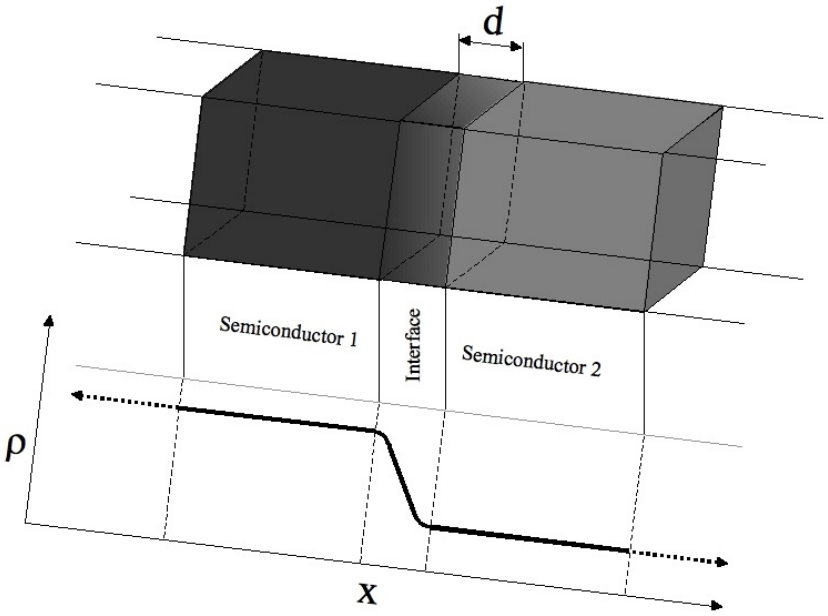


Figure 11: Schematic diagram of a junction between two semiconductors. In the junction the properties of one semiconductor change to that of the other; in this case the change in density is shown. In order to speak of a "junction" rather than a phase, the width, d, of the junction should be small compared to charge carrier diffusion length.

Although serious proposals on devices based on heterojunctions began in the 1950s [37], it wasn't until the next decade that quantitative results began to be published. Semiconductor-metal junctions had been investigated since the late 1930s and early 1940s by Mott, Bethe, Gurney, Shottky, Fan and others [38, 39, 40, 41], and this may well have been a necessary first step as the first theories of the semiconductor-semiconductor heterojunction grew out of this research.

While most of the first works were based on Ge/GaAs junctions, and later included the $Al_{1-x}Ga_xAs$, a semiconductor whose band gap is dependent on x, it was not until the advent of such deposition techniques as liquid-phase epitaxy, molecular beam epitaxy and metal-organic vapor phase deposition in the late 1970s and 1980s that the production of highly defined heterojunctions was possible [42, 43]. These techniques are able to produce highly uniform layers with thicknesses on the order of Ångstroms. Stacked many-layer systems called superlattices can be made to study directly the behavior of electrons in quantum wells [44].

[2]Transport characteristics include current-voltage (I-V) and capacitance-voltage (C-V) behavior.

In this work the deposition method is chemical bath deposition (CBD). While also able to produce very thin layers (<1nm), the layers are highly non-uniform, with thicknesses varying at times by more than 100% depending on the substrate used. This is of no consequence, however, because the goal of the CBD here is a passivation of the substrate surface and not the production of quantum wells.

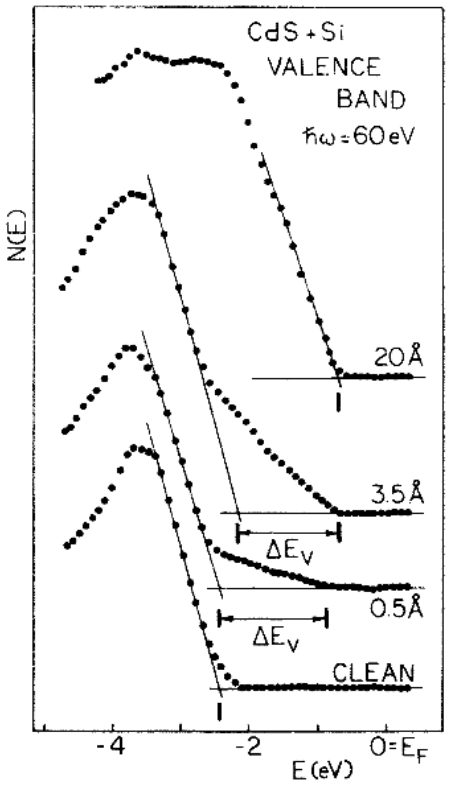


Figure 12: The valence band offset between CdS and Si can be directly measured in this spectrum. Not only are the band edges a favorable distance apart, but the cover layer was thin enough to allow the detection of the substrate. This situation is ideal and is more an exception than a rule. Graphic taken from [45].

This does, however, bring up the interesting question of what a junction between two materials actually is. The junction is the region between two semiconductors in which one lattice (and thus the properties of the solid) changes into that of the other, and roughly put, must have the distance d in fig. 11 small relative to charge carrier diffusion lengths [36]. Of course, with the techniques mentioned above, it is possible to make junctions with thicknesses of a few atomic planes, so that it is in fact possible to speak of abrupt junctions. In this thesis, though, as we will see, there is considerable intermixing of the elements from both semiconductors and the definition of the "heterojunction" here is not quite so straightforward. Following this point further, fig. 11 is obviously a highly idealized situation. If one takes inter-diffusion, as just one example, into account, the interface itself would be made up of several different regions similar to the region of width d, all flowing into one another.

However, because of the relatively abrupt nature of the heterojunction compared to the total dimensions of two semiconductors forming the junction, it seems suitable to use a localized characterization method when studying them. Early on, transport studies were carried out using current-voltage or capacitance-voltage techniques. The problem here is that these techniques average over the entire diode, while the junction is highly localized in space.

The surface sensitive nature of PES techniques is suitable to semiconductor heterojunction investigations, although the measurement error on the order of 0.10-0.20 eV may, in some situations, be too large to adequately describe a band offset. This drawback will be more thoroughly opined upon in the discussion of the individual results.

The most favorable situation using PES is one illustrated well by [45] and [46], where a spectrum of the former can seen in fig. 12. Here both valence bands are visible in a single

spectrum and ΔE_v can be read off directly. However, this is the exception. In many practical situations, when one is not dealing with ultra-thin layers, the substrate is no longer detectable after the deposition of only several nanometers of a top layer due to the surface sensitive nature of PES. Chapter 6 will discuss this in more detail.

There have also been attempts to predict the size of band discontinuities resulting in junctions made of certain materials which can help to illustrate the evolution of heterojunction research.

4.2.1 Electron Affinity Rule (Anderson Model)

The first attempt to quantitatively characterize semiconductor heterojunctions was made by R. L. Anderson using Ge/GaAs junctions [47]. Essentially an extension of the Shottky theory of semiconductor-metal junctions, Anderson predicted that the electron affinities, χ, of any two semiconductors (fig. 10), measured separately, determine ΔE_c through the equation

$$\Delta E_c = \chi_2 - \chi_1 \tag{8}$$

eq. 7 being used to determine ΔE_v.

Although now seen as a positive historical step, the fallacy can immediately be seen: semiconductor properties may be dependent on substrate, deposition temperature or deposition method. Therefore, there is no reason to assume, *a priori*, that the electron affinity of a semiconductor measured on a given substrate will remain the same when the same semiconductor is deposited under different conditions on another semiconductor to form a junction.

Anderson was, however, able to identify the band discontinuities as well as the built-in potential (band bending), $V_{tot} = V_1 + V_2$ (fig. 10) as the defining characteristics of the heterojunction. However, one main characteristic he failed to identify are the role of interface states on band offsets [36, 48, 49].

In fact, in a more modern slant, these interface states are identified in, for example [50], as the defining force behind the band lineup. Very similar to Fermi Level pinning (sec. 4.1.2) caused by metal-induced gap states in the Schottky Contact, there exists a mid-gap energy on each semiconductor surface which will achieve charge neutrality between the interface states caused by junction formation. If this mid-gap energy at both surfaces is aligned it will minimize the interface dipole induced by charged gap states. Deviations from this band lineup will be compensated by the induced dipole. If, however, the junction is in the presence of, for example, an external potential step, V, there may be a change in the band lineup on the order of V/ϵ away from the minimal dipole position, where ϵ is the bulk dielectric constant of the material. Thus, a screening effect limits the effect of the potential step.

4.2.2 Common Ion Rule

Another early theory attempting to describe the band offsets in a heterojunction is the common ion rule. The belief that the valence band of a binary semiconductor is made up mainly of the s and p states of its anion, led to the proposal that a heterojunction between two such materials with similar lattices would have a very small ΔE_v. Early work on the $Al_{1-x}Ga_xAs/GaAs$ junction using optical absorption seemed to confirm this hypothesis, as ΔE_c was found to account for 88% of ΔE_g, making ΔE_v accountable for only 12% of the difference [42].

This helped to establish an "85%-15%" rule for the common anion theory, which remained intact until the mid 1980s when photoluminescence methods showed the distribution of ΔE_c and ΔE_v to be 0.59 and 0.41 of ΔE_g, respectively [51].

The quandary over the failure to be able to predict seemingly simple systems was in part quelled in the late 1980s when it was shown that neglecting the cation d states in semiconductor heterojunctions with a common anion will result in a failed band offset calculation [52]. When applied to ternary and quaternary semiconductors, it was found that the d state contribution of different cations was sometimes self-compensating, leading to successful predictions using the common ion rule. These were, however, exceptions. And, as we will later see in this thesis, the common ion rule in no way predicts the band offset in the system under study here (chapter 6).

One drawback to many current models and theories employing computer calculations is that they rely on bulk values of the semiconductor to give information about the band offsets. Although these offset values may be a good first approximation, especially when considering heterojunctions with single-crystal components, it is well known that the surface states of the lattice may be very different from the bulk states. This difference may be due to concentration gradients in the sample, that is, a position-dependent stoichiometry, or simply to surface relaxation/reconstruction due to the end of the repetitive nature of the lattice. This and the diffusion of elements of one semiconductor of the heterojunction into the other and vice versa have special significance in this thesis and will be discussed at various points throughout the work.

This rather complicated heterojunction is one of the main building blocks for a type of thin layer solar cell. The next section will first discuss several characteristics of the solar cell based on a homojunction because of its relative simplicity. A few comments will then be made about the differences between solar cells based on homojunctions and those based on heterojunctions before the actual heterojunction and solar cell of interest make there appearances.

4.3 The Photovoltaic Cell

Most of the information contained in this section is taken from either [34] or [53], two excellent introductions to solar cell physics. It can, therefore, be assumed that the information here is from one of these two sources, unless another source was used, in which

case it will be cited as such.

4.3.1 The Photovoltaic Cell Based on the Homojunction

A solar cell, being a diode, is formed from a p-type and an n-type semiconductor having, in the most simple case, the same lattice or chemical make-up (for example two differently doped pieces of a mono-crystalline Si wafer). The result is a band diagram devoid of any discontinuities in the conduction or valence band edges (fig. 13). Before the two differently doped pieces are brought into contact with each other, they are still charge neutral. After forming the junction, mobile holes from the p-type material will defuse toward the interface with the n-type material, driven by diffusion pressure, leaving behind the negative static charge. The same process happens with the electrons entering the p-type material, leaving behind positive static charge, causing an effective charge separation. The mobile charge carriers recombine at the interface and the diffusion proceeds until it is balanced by the electric field generated by the charge separation. The result is the space charge region, found in the gray box in fig. 13, which leads to charge carrier separation and is the key to this kind of solar cell.

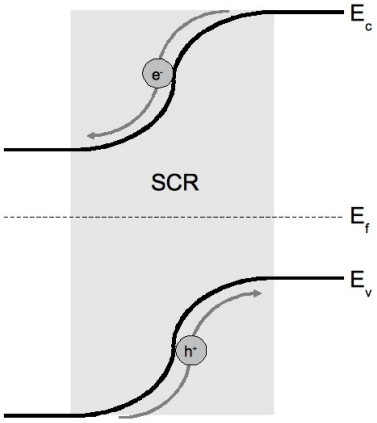


Figure 13: A homojunction made from two differently doped pieces of the same semiconductor. The gray box with the band bending is referred to as the space charge region.

An alternative and equivalent description is the alignment of the Fermi Levels in the p-type and n-type material causing depletion regions in both materials, the band bending signifying the same electric field mentioned above (fig. 14). The result is shown in fig. 14.

It is possible to determine the properties of the pn-junction and the space charge region exactly as long as the charge distribution is known [34]. Although this is not possible for most solar cells, the characteristics of a mono-crystalline Si solar cell can be predicted very well with such a model due to a detailed knowledge and control of the doping processes and zero defect density at the interface.

Starting with Poisson's equation (in 1 dimension) and integrating once:

$$\frac{d^2\varphi(x)}{dx^2} = -\frac{\rho}{\epsilon_p \epsilon_0} \;\Rightarrow\; E(x) = -\frac{d\varphi}{dx} \tag{9}$$

and assuming the following boundary conditions for an abrupt pn-junction:[3]

[3]Several simplifications have been made here: the fixed charge in both the n- and p-type semiconductors is taken to have a homogeneous distribution which leads to an abrupt end of the space charge region, the donator concentration in the p-type semiconductor and acceptor concentration in the n-type semiconductor have been ignored and it is assumed that all donors and acceptors are ionized.

$$\rho_p = \begin{cases} -eN_A \text{ for } -W_p \leq x \leq 0 \\ 0 \text{ for } x \leq -W_p \end{cases}$$

$$\rho_n = \begin{cases} -eN_D \text{ for } 0 \leq x \leq W_n \\ 0 \text{ for } x \geq W_n \end{cases}$$

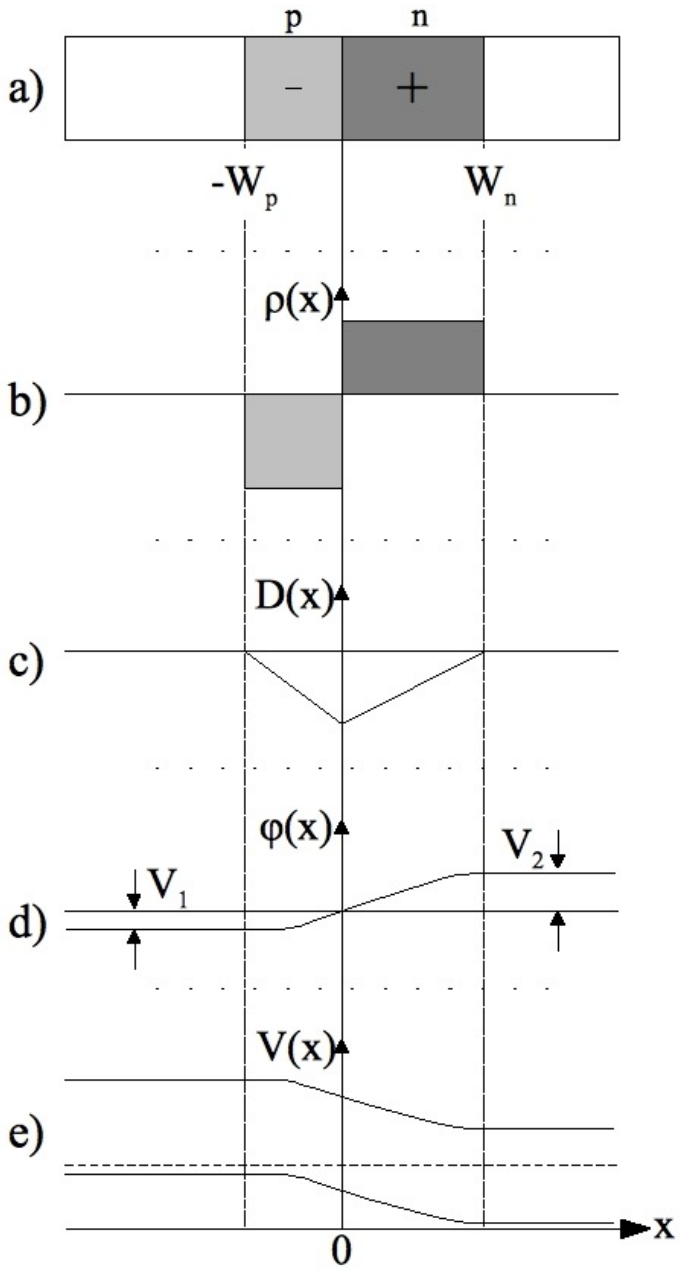


Figure 14: a)-e) show graphically the characteristics of the homojunction as derived from eq. 9-11 [34]. See text for explanation.

one can calculate the electric field in the space charge region. After calculating the integration constants using the boundary conditions, one obtains:

$$E_p(x) = -\frac{eN_A}{\epsilon_p \epsilon_0}(x+|W_p|) \text{ for } -W_p \leq x \leq 0 \tag{10}$$

$$E_n(x) = \frac{eN_D}{\epsilon_p \epsilon_0}(x-W_n|) \text{ for } 0 \leq x \leq W_n \tag{11}$$

with the field having a maximum at $x = 0$.

In the above equations, ρ_p and ρ_n are the hole and electron densities, respectively, and N_A and N_D the acceptor and donator concentrations, respectively. As usual, the ϵ_i stands for the permittivity of free space, of the p-type material and of the n-type material for $i = 0, p, n$.

Looking to fig. 14, the mathematical development of the space charge region can be followed. In a) one sees the fixed charge in each piece of material after the contact is made while b) shows this charge distribution, $\rho(x)$, in a graphical way. c) then shows the above derived equations for the electric field (eqs. 10 and 11), displayed here as the electric displacement field, $D(x) = \epsilon_i \epsilon_0 E_i(x)$, i=p,n. d) gives the change in potential across the junction and, finally, in e) the band

diagram of the homojunction is shown. Notice as well, that the derivation is general enough to allow different doping in each side of the junction and is reflected in all parts of fig. 14. For example, in b) the fixed charge concentration (acceptors) is higher in the p-side and is reflected again in e) where the Fermi Level on the p-side of the junction is closer to the valence band edge than to the conduction band edge in the n-type side.

4.3.2 The Origin of the Open Circuit Voltage

Although the system in fig. 14 is still in thermodynamical equilibrium, under illumination, where at least a part of the radiation is made up of photons with energy $h\nu \geq E_g$, the situation is different: the band bending is reduced because electrons created in the p-type material will diffuse into the n-type material (due to diffusion pressure and the direction of the electric field). This partially reduces the amount of depletion in that region. The holes created in the n-type material will have the same effect in the p-type material. The system is thus driven toward the flat-band regime.

In addition to this, the Fermi Level, common to both holes and electrons in the equilibrium situation will split in two "quasi-Fermi Levels," one for the holes and one for the electrons. The quasi-Fermi Levels are generally different in the p-type and n-type material.

The quasi-Fermi Levels are a consequence of the system no longer being in thermodynamic equilibrium. Because of the logarithmic dependence of the local charge carrier density on the position of the Fermi-Level,[4]

$$n = N_c e^{(-(E_c - E_F)/kT)} \tag{12}$$

impinging photons will produce a much larger change in the position of the minority charge carrier quasi-fermi-level than in that of the majority charge carriers. A few simple assumptions can illustrate this well: an intrinsic charge carrier concentration of $10^{10}/cm^{-3}$ and a donator concentration of $10^{16}/cm^3$ which corresponds to a hole concentration of $p_0 = 10^4/cm^3$, a photon flux of $10^{17}/cm^2/s$ and a charge carrier lifetime of $\tau = 10^{-}6\,s$. If the light is absorbed within $10\,\mu$m of the surface it can be seen that the change in population for each charge carrier under illumination will be $10^{14}/cm^3$. This means that that population of the majority charge carrier is left essentially unaffected by illumination while the population of the minority charge carriers jumps by 10 orders of magnitude. Thus, the quasi-Fermi level of the minority charge carriers can shift quite considerably while that of the majority charge carrier remains stationary showing why minority charge carriers are so important to the characteristics of the solar cell.

The role of the majority and minority charge carriers is reversed on the other side of the pn-junction, creating a potential difference between the same species of charge carrier on either side of the junction. This potential, V_{oc}, can be most clearly understood when expressed through the total band bending, or built-in potential, before (ξ_0) and after (ξ) the cell is illuminated:

[4]The new variable in eq. 12 is N_c, the effective density of states in the conduction band. The equation for the holes is completely analogous.

$$V_{oc} = \int_{SCR} \xi - \xi_0 \; dx = - \int_{SCR} \frac{(e\mu_n \Delta n + e\mu_p \Delta p)}{\sigma} \xi_0 \; dx \tag{13}$$

where μ_i are the charge carrier mobilities, Δi the light-induced change in charge carrier concentration and σ the total conductivity and the integration, as indicated, takes place over the space charge region. The Dember potential [54, 55] has been neglected here for purposes of clarity.

Looking more closely at the term in parentheses, it can be seen that $(e\mu_n \Delta n + e\mu_p \Delta p)/\sigma \leq 1$ because the maximum of the numerator is indeed equal to the total conductivity of the diode when $\Delta i \to i$, that is, the amount of light induced charge carriers far exceeds the number of intrinsic carriers. Furthermore, because the total band bending can be as large as the band gap itself, the total contribution to V_{oc} from the band gap will be less than, but on par with, E_g:[5]

$$V_{oc} \lesssim E_g \tag{14}$$

where the "$\sim$" part of the relationship symbol only comes into play as $T \to 0$.

This supports the connection of the splitting of the quasi-Fermi Levels to V_{oc}, because the amount of band bending will determine the maximum splitting of the quasi-Fermi Levels.

Furthermore, it can be seen that the size of the band gap is one of compromises as larger band gaps allow for more band bending and thus higher $V_{oc,max}$ while at the same time excluding the lower energy photons which cannot excite an electron across the energy gap ($h\nu < E_g$). This has the effect of reducing the splitting of the quasi-Fermi Levels and thereby limiting the actual V_{oc}. In addition, a high band gap can also limit photocurrent by limiting the total number of charge carriers. The theoretical optimum band gap is about $E_g = 1.4\,eV$ [6].

4.3.3 Solar Cell Characteristics Based on the Diode Equation

The action of a photovoltaic cell in the dark (which is exactly that of a simple diode) is described to a first approximation by the diode equation

$$j_d = j_s(e^{(eV/kT)} - 1) \tag{15}$$

where j_d is the dark current density, j_s the reverse saturation current density, V the applied voltage, e the elementary charge, T the temperature and k Boltzmann's constant.

The situation is similar under illumination but the entire diode curve is shifted along the current density (y-) axis by an amount equal to the photo-generated current density, j_l (fig. 15):

[5] Common rules of thumb are: $V_{oc} \sim \frac{2}{3} E_g$ and $V_{oc} \sim \frac{E_g}{q} - 0.4\,\mathrm{V}$ at room temperature.

$$j_{ph} = j_l - j_d = j_l - j_s(e^{(eV/kT)} - 1) \tag{16}$$

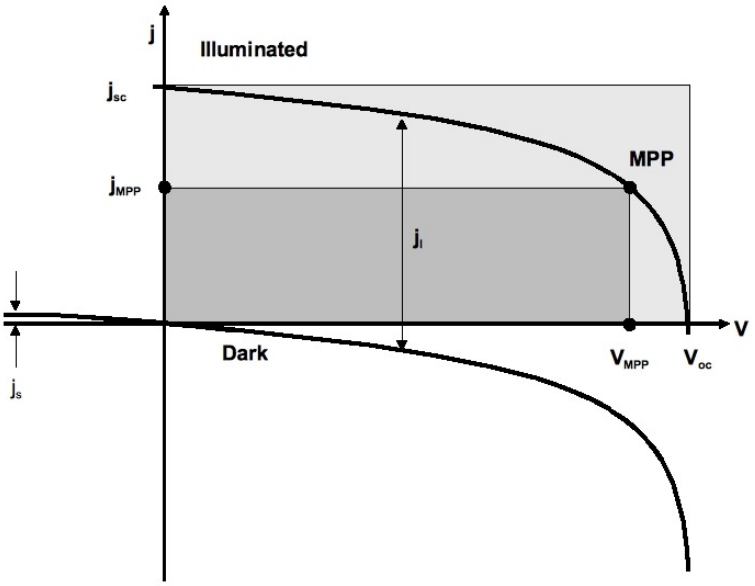


Figure 15: An example of a current-voltage (I-V) curve of a solar cell in the dark and under illumination.

where j_{ph} is the total photocurrent density in the solar cell. The minus sign between j_l and j_d shows that the photo-generated current and the dark current flow in different directions: the photo-generated current is due to the separation of charge in the cell, whereas the dark current is due to recombination from, for example, bulk recombination or charge carriers thermally activated over the potential barrier.

Many of the important characteristics of the solar cell can be determined from from fig. 15 or, equivalently from eq. 16, including the short-circuit current (j_{sc}) and the open-circuit voltage (V_{oc}) at the points where the curve crosses the X-axis and Y-axis, respectively. It is noteworthy to point out that the curve shown in fig. 15 is not an example of a good I-V curve. However, the different parts of the curve can be easily seen.

In eq. 16, j_{sc} can be found by setting the voltage, V, to zero giving

$$j_{sc} = j_l \tag{17}$$

V_{oc}, on the other hand, can be found by setting $j_{ph} = 0$ and solving for V:

$$V_{oc} = \frac{kT}{e} ln\left(\frac{j_l}{j_s} + 1\right) \tag{18}$$

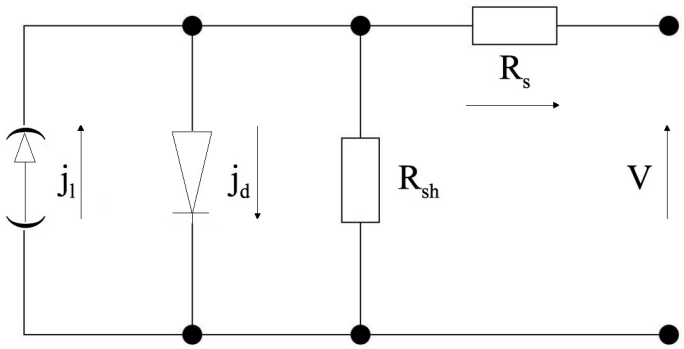


Figure 16: The equivalent circuit of a solar cell. See explanation in text.

In addition to j_{sc} and V_{oc}, three other parameters are very important to the solar cell. The maximum point of power, MPP, is the point on the I-V curve where the product $I \cdot V$ is a maximum. The MMP can then be used to determine the fill-factor of the solar cell, defined to be $FF = [(I_{MPP} \cdot V_{MPP})/(I_{sc} \cdot V_{oc})]$, equal to the ratio of the two gray rectangles

in fig. 15, and the cell efficiency $\eta = P_{MPP}/P_{in}$, where P_{in} is the incident power.

The diode-nature of the solar cell is re-enforced through fig. 16 showing the equivalent circuit of a solar cell. The photocurrent source, j_l, is connected in parallel with the diode, j_d and two sources of resistance have also been added here.

The parallel resistance, R_{sh}, is due to shunts in the solar cell, caused, for example by small short circuits or diffusion paths along grain boundaries and has the effect of decreasing the fill factor, FF, by flattening the cell's I-V curve and reducing V_{oc}. The series resistance, R_s, on the other hand, is due to the resistance between the semiconductor layers themselves, from the metal back contact and the front grid. R_s reduces J_{sc} and also causes a decrease in FF [56].

From these descriptions it can once again be seen how critically V_{oc} and j_{sc} depend on one another, that is, the solar cell is a thing of compromises.

4.3.4 The Photovoltaic Cell Based on the Heterojunction

The description of the homojunction above is of course an idealized situation, although, as mentioned already, some kinds of Si solar cells can be described quite well using a similar model. However, the description does propose guidelines for characterizing other, more complicated kinds of solar cells where one is often left with intuition alone owing to the complicated nature of the materials involved. The mechanisms and processes in these more complicated devices are no different than those in the homojunction, but the system is simply less defined and/or definable. Too many unknowns about stoichiometry, charge carrier densities and defect distributions make the application of such exact quantitative theories of little interest and is often nonsensical.

Heterojunction solar cells are often made from such materials or "mixed crystals," although the term "heterojunction" does not refer to the nature of the crystals per se. As described above, cells containing heterojunctions are defined through metallurgical junctions between materials of different lattices or chemical make-ups. Whereas the homojunction, consisting of two differently doped identical lattices, has no discontinuity in the conduction or valence band, such an offset in one or both bands is the hallmark of the heterojunction solar cell (fig. 10). And these offsets can have large effects on the characteristics of the solar cell.

Returning to eq. 13 from the previous section, we must now modify this equation due to new possible gradients in the electron affinities and band gap (or, equivalently, in the valence and conduction band edges) as well as in the densities of states at the band edges on either side of the heterojunction:

$$V_{oc} = \int_{cell} \xi - \xi_0 \; dx = -\int_{cell} R(x)\xi_0 \; dx + \int_{cell} E_{edge}(x) \; dx + \int_{cell} N_{n,p}(x) \; dx \qquad (19)$$

where $R(x) = (e\mu_n \Delta n + e\mu_p \Delta p)\rho$, making this term the same as the right side of eq. 13 apart from the integration limits, and $E_{edge}(x) = f(\chi(x), \chi(x) + E_g(x))$ and

$N_{n,p}(x) = f(N_v(x), N_c(x))$ are functions which describe the spacial dependence of the electron and hole affinities and the electron and hole densities of states, respectively [53]. The Dember potential has again been neglected [54, 55]. The integration over the entire cell accentuates the fact that material properties may be different in all parts of the cell, not just those affected by band bending. In fact, the very idea of charge diffusion and band bending described for the homojunction becomes increasingly blurred as some mixed crystals have intrinsic surface band bending or the change in the Fermi Level position after the deposition of a top layer is due to a pinning or re-pinning of the Fermi Level from interface states. It may also be the case that no additional band bending is found as a consequence of the deposition; the second semicondcutor may only act to supply a workable transition between the substrate and later layers needed to complete the cell.

More than just creating a more complex equation for its description, a heterojunction made of poorly understood crystals will make the determination of the functions in eq. 19 impossible. Similarly, the quantities R_{sh} and R_s in fig. 16 will also be difficult to determine.

Although the crystals used are sometimes difficult to reproduce or their properties cumbersome to ascertain, the use of such substances can be justified on many grounds. Some materials may have attractive absorption properties but can only be produced as either p- or n-type with relatively low cost of production. Heterojunctions may also offer a way to engineer a solar cell in order to, for example, strategically place the pn-junction in a region of low defect density thereby limiting recombination at the interface. Also, top- or back-surface fields may be included in order to limit charge carrier access to recombination sinks. An optimized band line-up can also be achieved using materials with different band gaps or absolute band positions. Some rules for the construction of heterojunction solar cells are proposed in [1].

A well known family of solar cells based on the ternary compounds $A^I B^{III} Ch_2^{VI}$ (A^I=Cu, B^{III}=In, Ga, Ch_2^{IV}=Se, S), jointly referred to as CIS, are an example of one of these ill-defined systems. CIS is commonly used as absorber material in chalcopyrite-based heterojunction solar cells with the structure substrate/Mo/absorber/buffer[6]/i-ZnO/n^+-ZnO [57, 58, 59]. A scanning electron micrograph (SEM) cross section of KCN etched $CuInS_2$ absorber on Mo along with a SEM cross section of a complete cell stack can be seen in fig. 17. Noticeable in the figure are the hollow regions between the CIS and the Mo, which sometimes lead to adhesion problems.

In this thesis the details concerning heterojunctions in general and the resulting solar cells will be focused on Cu(In,Ga)S_2 solar cells with the main emphasis being on the Cu(In,Ga)S_2/buffer junction as opposed to the buffer/ZnO junction. Special attention will be given to the Cu(In,Ga)S_2/CdS junction although inferences will often be made using the much more thoroughly studied Cu(In,Ga)Se_2/CdS sister system. Finally, possible influences of the application of ZnO will also be discussed, as the buffer/ZnO junction may heavily influence the finished device.

[6]Possible buffer layer materials include CdS, Zn(Mg,O), Zn(O,S) and In_2S_3.

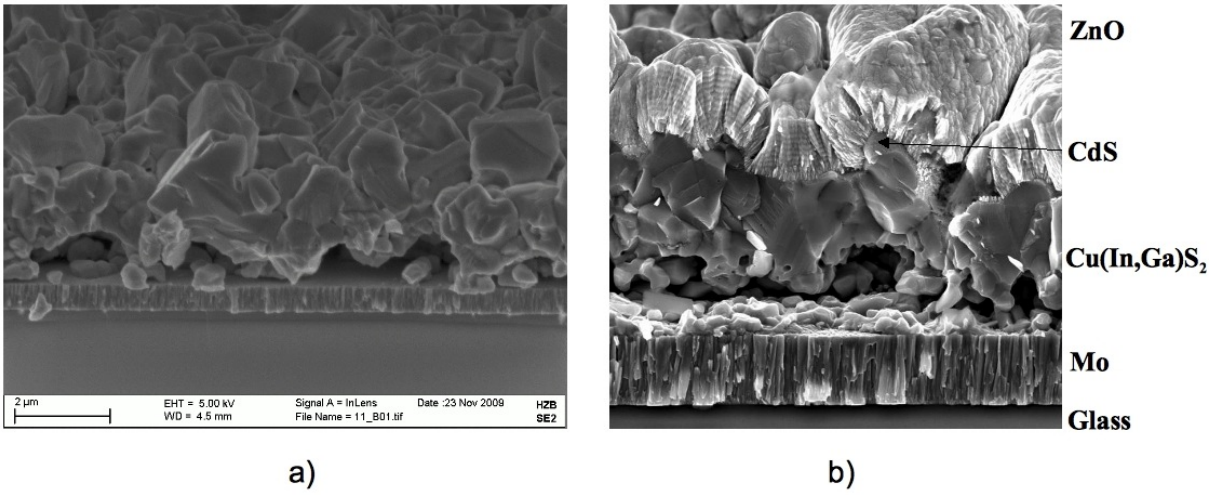


Figure 17: Scanning electron micrographs (SEM) showing a) a KCN etched CIS absorber on Mo and glass, while b) shows the completed Glass/Mo/$CuInS_2$/CdS/i-ZnO/n^+-ZnO stack as it appears in a finished solar cell (contact grids are lacking). In b) the individual layers are marked although CdS, found between the CIS and the i-ZnO is not visible as its thickness is in the 10's of nm. The arrow points to the surface of the CIS where the CdS has been deposited. The extreme fluctuations in the CIS surface morphology are evident.

4.4 The Cu(In,Ga)S_2/CdS Junction and Cu(In,Ga)S_2 Thin Layer Solar Cells

Note: Because of the rather limited body of literature that exists about the $CuInS_2$/buffer system, and more acutely about Cu(In,Ga)S_2/buffer system, this section, and indeed the entire thesis, draws on many publications about Cu(In,Ga)Se_2 and the Cu(In,Ga)Se_2/buffer system for comparison. Although there are many similarities between the Se and S systems, any comparison must be made with caution as differences do exist. When making these comparisons, care has been taken to explicitly draw the readers attention to possible differences if needed. This seems not only a fair way to circumvent holes in the literature, but is also a sensible way to make faster advances in research by exploiting the results of a similar, more well-studied system. In addition the author will attempt to differentiate between $CuInS_2$ and Cu(In,Ga)S_2 by referring to the Ga-containing system when the effects of the Ga are explicitly being explored or when the general system itself is being considered. In some of the latter cases it will be irrelevant if the system contains Ga or not, but because the addition of Ga is considered to reflect the modern state of research, it will be included if possible.

The CIS/CdS contact was first investigated in the 1970s as a photovoltaic detector. At that time the pn-junction was made of a 1.0-1.3 μm CIS substrate covered with a thick (5-10 μm) CdS layer, then referred to as the "window"[60, 61]. Today, however, for purposes of direct sunlight-to-electricity conversion in a solar cell, the CdS layer, now called the buffer layer, has shrunk to a thickness of $\sim$40 nm and the "window" now consists of a $\sim$450 nm thick i-ZnO and n^+-ZnO layer, usually doped with Al [62].

The absorbers used in this work were produced at the Helmholtz-Zentrum Berlin by rapid thermal processing. Cu or Cu/Ga and In were deposited sequentially as stacked elemental layers by DC magnetron sputtering onto Mo-coated float-glass substrates. The stacks were then heated under Cu-excess conditions ([Cu]/[In+Ga])=1.30-1.6) with radiation to about 600°C, the sulfur source being elemental sulfur powder placed in a quartz sample holder together with the sputtered layers before heating [58]. The end result are polycrystalline CIS absorber layers.

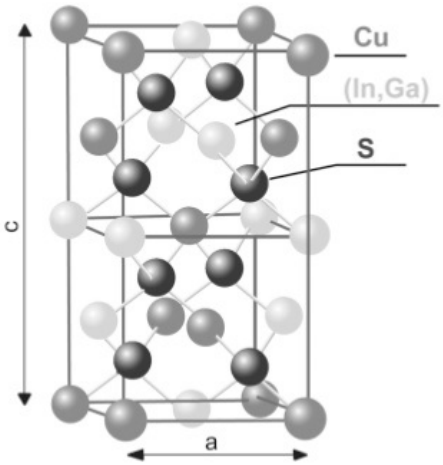


Figure 18: The chalcopyrite crystal lattice of $CuFeS_2$ with (In,Ga) replacing the Fe to create the $Cu(In,Ga)S_2$ structure found in the chalcopyrite-based thin-layer solar cells investigated here.

The kinetics of the sulfurization process itself have been studied using in-situ X-ray diffraction with [63] and without [64] Ga and have been used to optimize the growth process of the absorbers used here.

CIS, a I-III-VI_2 semiconductor compound, crystallizes in the tetragonal chalcopyrite form, a derivative of the original $CuFeS_2$ chalcopyrite (fig. 18), which is itself a derivative of the zinc blende (or sphalerite) structure, (Zn,Fe)S. While chalcopyrite, when referring to the materials discussed in this thesis, could mean the entire $Cu(In,Ga)(Se,S)_2$ system, the $Cu(In,Ga)S_2$ lattice is referred to as roquesite. Typical lattice constants for roquesite are a=5.34 Å and c=10.47 Å for $CuGaS_2$ and a=5.52 Å and c=11.13 Å for $CuInS_2$, showing an increase in density with the addition of Ga [65]. As in the $Cu(In,Ga)Se_2$ system, the addition of Ga to the $CuInS_2$ system opens the bulk band gap by ∼100-200 meV, and is discussed further in sec. 7 [66]. Although the original thought process driving the incorporation of Ga was more along the lines of creating a top cell for a tandem solar cell system because $CuInS_2$ already has an optimal E_g, incorporating Ga into a single cell also increases the cell's efficiency, η, and V_{oc} by ∼100 mV [67]. For CIS, the main characteristics of the cell are η ∼11%, V_{oc} ∼730 meV, j_{sc} ∼22 mA/cm^2 [58], while for CIGS the numbers are η ∼12%, V_{oc} ∼830 meV, j_{sc} ∼22 mA/cm^2 [67].

Due to the Cu-rich growth conditions, excess Cu is deposited on the surface of the absorber in the form of $Cu_{2-x}S$ and/or CuS. This is not thought to be a complete layer of CuS, but rather island-like growth resulting in differing lateral thickness. For photovoltaic uses this layer must be removed through an etch step using a solution of aqueous potassium cyanide (KCN) because of the high conductivity of this layer [68]. Some experiments were done here without removal of the CuS (sec. 5.2), however, unless otherwise noted, all $Cu(In,Ga)S_2$ samples were etched for three minutes in 5% KCN solution to be sure of the complete removal of CuS. Because the KCN etches the CIS much more slowly than the CuS, longer etch durations to ensure CuS removal are of little consequence to absorbers [69].

After the removal of the CuS, the buffer layer is applied. Although several different buffer layers are available with many different deposition methods, the buffer layer used here is

exclusively CdS applied by chemical bath deposition (CBD). The CBD CdS layers were deposited at 60°C using standard solutions of Cd-acetate ($Cd(C_2H_3O_2)_2$), ammonia (NH_3) and thiourea (H_2NCSNH_2). The absorbers were produced independently of this work and at a geographically different site from where the research for this thesis was carried out, but the CdS layers were deposited by the author just prior to the experiments. Although this means that the Cu(In,Ga)S_2 junctions may not be of standard solar cell quality, it does insure that a fresh, clean, defined junction was repeatedly formed within the realities of the chemical bath deposition.

On Cu(In,Ga)Se_2 as well as on commercial glass slides CdS crystallizes in both hexagonal and cubic zinc blende structures, having lattice constants of a=4.14 Å and c=6.71 Å and a= 5.82 Å, respectively. In addition, it is possible that some amorphous regions exist [70, 71]. It has also been shown that the structure of CBD CdS is temperature- and substrate-dependent [72, 73]. As would seem likely, some orientations of the CIS lattice carry on into the zinc blende structured CdS, but due to the polycrystalline nature of the Cu(In,Ga)S_2 samples, it is assumed here that all three phases of CdS are present in the CBD CdS layers, although no actual investigation was carried out. In addition, it is also assumed that the usual impurities are present in the layer, including $Cd(OH)_2$, C, O and H impurities, and perhaps at an increased level due to the low processing temperature of 60°C used in this thesis [74, 75].

The application of the CdS or other buffer seems to be necessary in both the $CuInS_2$ and the Cu(In,Ga)Se_2 systems in order to obtain a working pn-junction [74]. Speculation as to the reason for this touches on several points. The CdS may provide a chemical passivation of the CIS surface, thereby reducing defects at the interface [76, 77], it may optimize the band alignment between the absorber and the window layer [62] or it may provide a better lattice match between cell components. The lattice matching between $CuInSe_2$ and CdS is, however, far better than between $CuInS_2$ and CdS [78] which may, in part, explain the often observed high interface recombination in the $CuInS_2$ system under illumination [66, 68]. Furthermore, the CBD may also "clean" the CIS surface as well as allow Cd to diffuse into the CIS, possibly resulting in an n-type inverted absorber surface layer (see chapters 5 and 6) [71, 75, 79].

In this particular kind of solar cell with a p-type absorber and n-type buffer and window layers, the electrons are the minority carriers at the position in the absorber where electron-hole pairs are created and separated. Because the minority charge carriers define the characteristics of the solar cell, it is important in this case to consider the transport mechanisms effecting the electrons in the conduction band, one of the most important being the alignment of the the conduction bands at the interface between two constituents of the cell.

The three possible conduction band diagrams resulting from the construction of the CIS/buffer junction can be seen in fig. 19. The band diagrams are shown here without the window layer, although it is likely that the window layer, such as ZnO, has an effect on the finished band diagrams describing the entire solar cell. These effects, for example charge injection, will, however, only change the amount of band bending in the absorber and/or buffer layer and WILL NOT affect the band offsets between these two

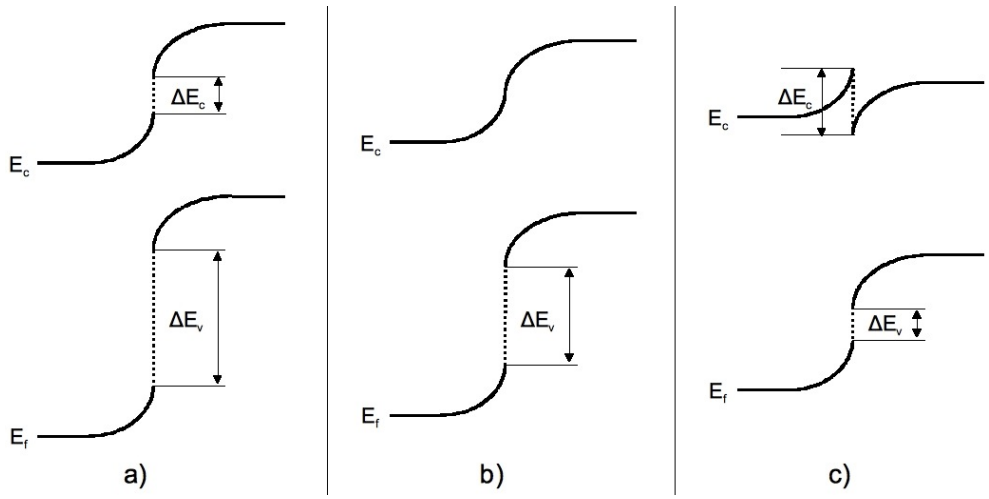


Figure 19: Three possible conduction band line-ups in the region around the absorber-buffer junction, including a) a cliff, b) aligned conduction bands and c) a spike. It can also be seen how knowledge of the valence band offset and the band gap can lead to assumptions about the conduction band offset.

layers.[7] Although it can be immediately seen that the junctions here, and in fact that entire band diagram, in no way resembles that of the homojunction discussed above, the junction itself is by no means less important to the device. In fact, the junctions in these kinds of solar cells may indeed be more important to the functionality of the solar cell because the possibility of band gap engineering.

While the aligned situation, b), is often ideal, posing no barrier to electron transport, the spike configuration in c) can have the effect of pushing the Fermi-level toward the conduction band, thereby moving the point were n=p deeper into the absorber, the result being a reduction in charge carrier recombination (see sec. 6.2). As long as the spike is no larger than 300-400 meV, it will have no negative effect on the current [80]. The third possibility, the cliff, shown in a), has the effect of reducing the effective band gap, E_{eff} in fig. 10, at the junction thereby increasing Shockley-Read-Hall recombination and leading to an increased dark current and decreased voltage [57]. The point were n=p is also moved closer to the metallurgical junction which also increases charge carrier recombination [1].

The $CuInS_2$/CdS junction is thought to have a conduction band cliff in the range of 300 eV, which would help to explain its limited efficiency compared to other chalcopyrite thin-layer solar cells, although not everything in literature supports this (see chapter 6) [81]. The effect of Ga on the band line-up is the subject of chapter 7 of this thesis.

Other characteristics of the solar cell based on the Cu(In,Ga)S_2/CdS junction as well as characteristics of the junction itself will be discussed in further detail in the various results sections. Putting these discussions in the context of the results improves the effectiveness of the thesis as these are its central concepts.

[7] The band offsets are determined alone through the chemistry of the two materials involved and not through doping.

5 $CuInS_2$-CdS Junction Formation

The deposition of CdS onto $CuInS_2$ before the application of the ZnO window layer is of vital importance because the CdS or other buffer is necessary to produce a functioning pn-junction in the solar cell [74]. There have been several reasons proposed for this including the CdS chemically passivating the CIS surface, which leads to a reduction of defects at the interface [76, 77]. CdS may also optimize the band alignment between $CuInS_2$ and the window layer [62] or improve lattice matching between these two cell components. Finally, the CdS deposited via chemical bath deposition (CBD) may allow Cd to diffuse into the CIS, possibly resulting in an n-type inverted absorber surface while at the same time allowing Cu from the absorber to diffuse into the CdS [71, 75, 79, 82].

In this chapter the Cd and Cu diffusion processes will be investigated by incremental etching of a thick (∼35 nm) CdS layer deposited on CIS with HCl in order to obtain a depth profile of the CdS and to re-expose the surface of the CIS after CdS deposition. While this experiment, in part, investigates the chemical state of the Cd on the CIS surface, HAXPES, X-ray absorption and XES experiments investigate the diffusion of the Cd into the absorber in an attempt to determine the extension of the diffusion into the absorber and which lattice positions the Cd occupies.

Further XPS/UPS experiments on samples etched with HCl are also done in order to investigate the band bending caused on the CIS surface during CdS deposition as well as the role of Cd as a dopant in CIS.

The "junction," as discussed throughout this thesis consists of an absorber from the HZB baseline as a substrate with CdS cover layers of differing thickness. CBD is a simple wet chemical deposition method using standard solutions of Cd-acetate ($Cd(C_2H_3O_2)_2$), aqueous ammonia (NH_3) and thiourea (H_2NCSNH_2). A 200 mL double-walled glass container allows water at 60°C to be pumped around the CBD solution, which begins at room temperature and is contained within the inner wall, in an attempt to heat it in the same way with each separate deposition. The glass was first filled to ∼120 mL with de-ionized water after which the sample was inserted and secured at a reasonable depth. The thiourea dissolved in ∼50 mL of de-ionized water was then added and finally the Cd-acetate in NH_3. As soon as possible after the addition of the Cd-acetate the pump was switched on and the heated water began flowing immediately, making this a "warm-start" deposition.

As a slight variation to this, a Cd treatment, known as "partial electrolyte treatment" [83, 84, 22] was often performed where the S source, thiourea, was simply left out of the solution in order to only investigate the effect the Cd and NH_3 have on the CIS surface. These treatments, with a duration of 50 minutes, were longer than the CdS deposition, and the Cd concentration was quadrupled along with the quantity of NH_3. The increased times and concentrations were meant to enhance any effects caused by Cd or NH_3 and not meant to create the exact conditions of the normal CBD [22]. It is known that this technique creates a thin ∼1nm layer of CdS on the surface of $Cu(In,Ga)(S,Se)_2$ substrates, the S coming from the absorber itself [85]. Here, this CdS layer was in some cases etched away before experimentation and in other cases left on the sample. The specifics of this etching accompany the results of each experiment.

Also, the choice of the author to make the depositions stems from the benefit of loading the sample into the vacuum chamber directly after completion of the junction. Although this means the samples may differ slightly from those found in completed HZB baseline solar cells, the alternative is extended time in air and deposition conditions not directly under the author's control.

Another difficulty with CBD CdS deposition are the layer thicknesses. Deposition times ranging from 40 seconds to 7 minutes correspond to CdS layer thicknesses between <1 nm to 30-40 nm, respectively. This means that one must be careful when comparing layers with extreme deposition times. In all likelihood, the creation of the layer begins almost instantly with ion-by-ion deposition [86], meaning the short deposition times may produce incomplete layers, i.e., layers with large open areas of substrate or large areas of substrate lacking CdS but which have been treated in a way similar to the Cd-treatment mentioned above.

In this chapter, samples referred to as "HCl-etched" were all first etched in KCN to remove CuO and CuS from the surface. This is done to reduce confusion by referring to every KCN-HCl etched sample as such. Some samples were etched again in KCN after being etched in HCl and are referred to as "HCl-KCN-etched" to distinguish them from samples not re-etched with KCN. The HCl-KCN samples are denoted as such because of the specific order of the etching, namely, that a KCN etch step came before the HCl as usual, but also after.

5.1 Cd and Cu Diffusion During Chemical Bath Deposition

5.1.1 Etching with HCl

Most of the experiments in this chapter deal with the deposition (or Cd treatment) and subsequent etching of CdS layers on CIS. Part of the goal of this section is to investigate for $CuInS_2$ results found in [87] for Cu(In,Ga)Se. Here it is shown that although HCl is able to remove the CdS deposited on epitaxial $Cu(In,Ga)Se_2$ substrates, a Cd-containing compound remains bound on the CIGSe surface and is not removed even after long (>24 hours) etching times. It is then immediately interesting to know whether this is also true for CdS on $CuInS_2$ and whether CBD of CdS "treats" either absorber in a different way. The results from [87] show that that the Cd incorporates itself into the CIGSe surface in a bonding environment different from CdS because of the Cd-containing layer's insolubility in HCl.

In [87], SEMs of HCl-etched CIGSe films showed no rounding of the sharp steps characteristic of epitaxial layer morphology. This was taken as evidence that the absorber itself was not attacked by the acid. Other reports, such as [88], also report that HCl does not attack $CuInS_2$.

This is different in the case of the RTP-produced CIS layers investigated here. Fig. 20 shows the effect of a one hour etch in concentrated 32% HCl, where holes can be seen in

the absorber, the result of a large removal of material. Although this is a much higher concentration than used in the experiments in this chapter, it shows that HCl, at a high enough concentration, can indeed etch away CIS at rates which can effect layers of several tens of nm. Both images in fig. 20 were taken from the center of the sample; at the edges of the HCl-etched sample the CIS was almost completely removed. Solubility was not confirmed in such a concrete way with lower HCl concentrations, however, short etch times in lower concentrations did change the stoichiometry of the CIS surface and, according to XPS measurements, preferentially removed In. SEMs were made of samples etched in lower concentrations but no changes could be observed because of the already rounded and irregular features defining the CIS morphology.

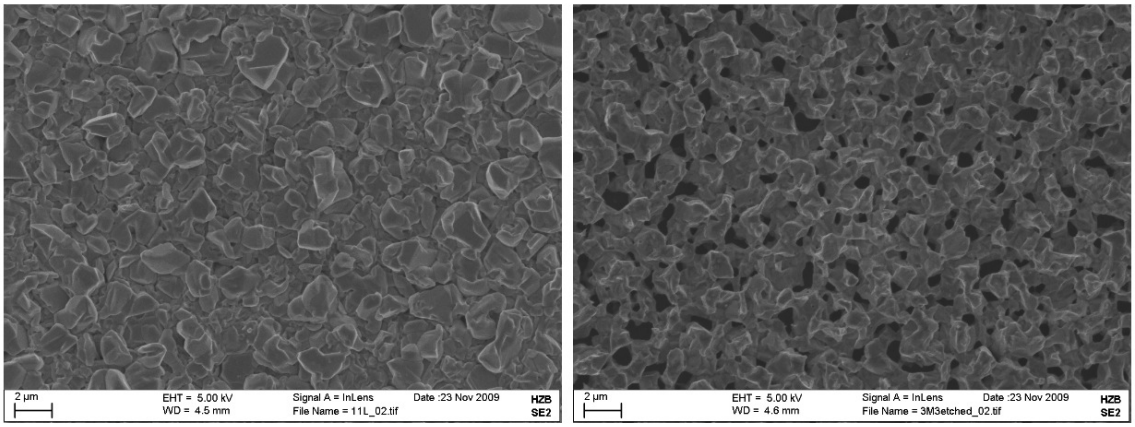


Figure 20: Scanning Electron Micrographs (SEM) showing a) the surface of KCN-etched CIS and b) the surface after one hour in 32% HCl. The removal of large amounts of material is clearly visible.

The result of the solubility of CIS in HCl means that experiments similar to those found in [87] done with CIS must consider that the HCl may remove the volume of CIS possibly containing Cd, whereby the HCl would appear to have removed the Cd. This was avoided by removing a thick (∼35 nm) CdS layer deposited on CIS through incremental etch steps of several seconds duration in 4% and 8% HCl. The added benefit here was that a depth profile of the CdS was created revealing, among other things, information about Cu diffusion in CdS.

5.1.2 Diffusion: XPS/UPS Investigation

5.1.2.1 Core Level Observations Beginning with short etching times of between two and three seconds, a ∼ 35 nm CdS layer was incrementally removed from a CIS absorber and core levels were measured with XPS in order to follow the removal process in detail by creating a depth profile of the CdS and to ensure that a volume of CIS possibly containing Cd was not removed before it could be measured. Because the removal of the CdS layer is very clear in the measurements, the observation of the CIS surface immedi-

ately after CdS removal was possible, as well as after longer etch times. Not only was it shown that Cd remains on the CIS surface after more than six hours in 8% HCl solution, but the diffusion of Cu into the CdS was also observed.

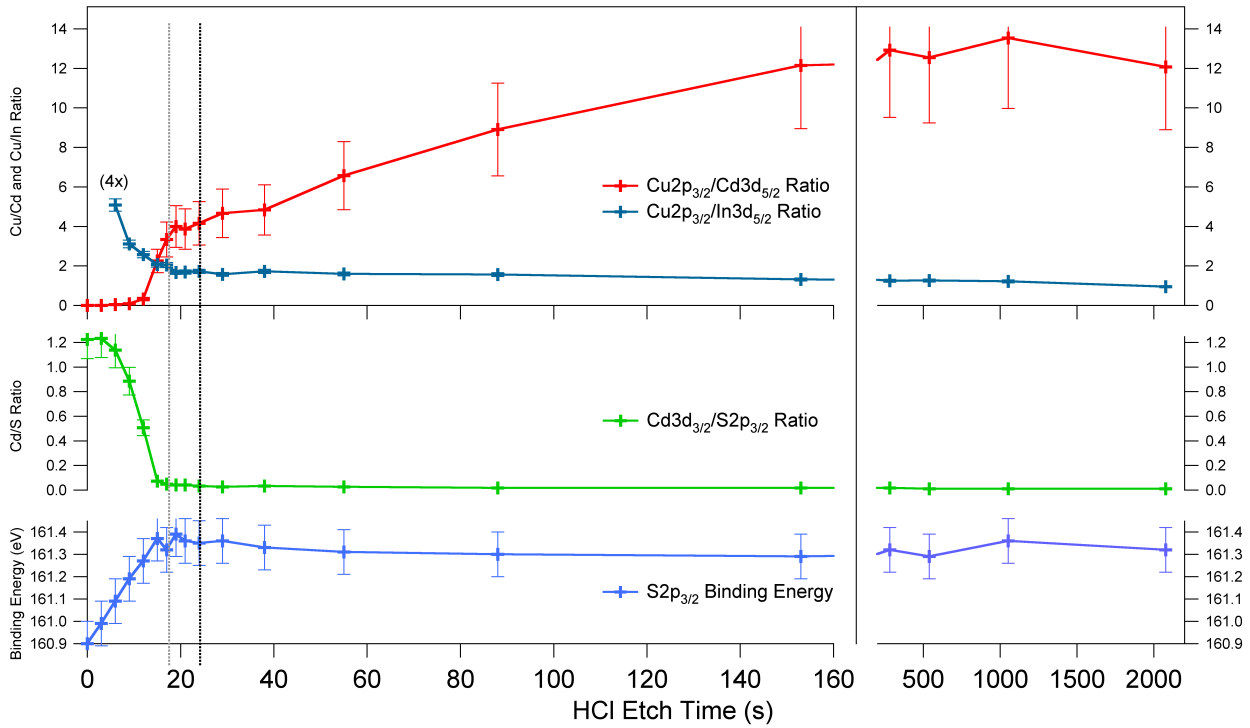


Figure 21: The incremental etching of a $\sim 35\,\text{nm}$ thick CdS layer on a CIS absorber with HCl shows that Cd remains on the CIS surface ([Cd]/[Cu]>0) after the complete removal of CdS, and that Cu diffuses into the CdS layer during CdS deposition. The ratios were calculated using the denoted peak areas under consideration of the factors mentioned in sec. 3.2.7 for quantitative XPS analysis.

Fig. 21 shows the results of the incremental HCl etch experiment. The times shown on the x-axis correspond to the actual time the sample was in HCl plus one second for the rinsing process. Thus, the first point at three seconds corresponds to the sample being held in HCl for two seconds plus one second for the rinsing process to remove the HCl from the CIS surface, thereby stopping the etching process. Also of importance is to note that the HCl concentration was 4% until the 24 second mark (marked by the black dotted line), at which point the solution was switched to an 8% concentration in order to accelerate the etching process thereafter.

Because of the start-stop action of this experiment, any quantitative conclusions made about the duration needed to remove the CdS would be very inaccurate at short etching times because the error associated with the time axis is rather large ($\pm 2\,\text{sec}$) but after longer etching times the error becomes much less significant. This graphic is, however, meant to be qualitative. The break in the time axis omits no measurement points, but is necessary to accommodate all points in one graph. The points themselves have been calculated using the quantitative XPS method discussed in sec. 3.2.7 and have an error

of ±10%, the entirety of which is a result of the fitting of the measured peak surface area. The other factors in sec. 3.2.7 also contain an error but have not been included here because they are systematic and would only influence the curves through a vertical shift leaving the characteristics of the curves intact. The last curve showing binding energy has an error of ±0.1 eV also arising from the fitting of the measured peak.

The most noticeable feature of fig. 21 is the large change in all four curves between 14 and 18 seconds (marked by the gray dotted line). In this temporal region the [Cu]/[Cd] ratio changes from 0 to 3.99 due to the removal of CdS. The [Cu]/[In] ratio changes from a value not consistent with CIS to one between the values for KCN and freshly HCl-etched CIS (1.27→0.42). The [Cd]/[S] ratio changes from a value corresponding to CdS_{1-x} with $x \sim 0.2$ (the S vacancies giving CdS its n-type character) to a value no longer consistent with CdS (1.22→0.04) and further supports the total removal of CdS from the sample surface.

The [Cu]/[Cd] ratio shows clearly that the HCl completely removes the CdS quickly as expected and leaves behind a small amount of Cd whose concentration diminishes further with each successive etch step. However, the Cd was never completely removed from the sample surface and was detectable even after six hours etching time. The further decrease in the [Cu]/[Cd] ratio is probably due to the partial removal of the CIS itself, as discussed above. This insolubility shows that the remaining Cd is not present as a constituent of CdS because it cannot be dissolved in HCl, although it may still be bound to S because the Cd most probably occupies a cationic lattice position in or on CIS [79, 89]. This Cd-containing layer will often be referred to as the CIS:Cd layer hereafter.

In order to exclude the possibility that the Cd was temporarily removed by the HCl and then "re-deposited" before the sample was removed from the acid bath, the sample was switched to a new bath after no longer than 32 seconds up to 9 minutes of total etch time and after every minute up to 18 minutes of total etch time. The last etch step of six hours was completed in one acid bath.

Moving to the [Cu]/[In] ratio, now, the curve in fig. 21 begins with a relatively high Cu concentration and decreases before and during the time in which the CdS layer is actually being removed. This is interpreted as a diffusion of Cu into the CdS layer, whereby the In signal increases as the CdS, together with the diffused Cu, are etched away. The missing points prior to 6 seconds are the result of a lack of both Cu and In signals until this time and show that Cu does not diffuse through the entirety of the CdS layer to its surface. The increased [Cu]/[In] ratio at the beginning of the etch process is not due to the above mentioned preferential etching of In by HCl etching. Longer etch times removing increased amounts of In would cause the [Cu]/[In] ratio to climb with longer etch times as opposed to what is observed. Furthermore, the main change in the [Cu]/[In] occurs before the CdS has been removed from the sample surface, meaning that the HCl has not yet made contact with the CIS surface. This is supported by the UPS measurements in sec. 5.1.2.2 below where surface sensitive measurements first show a CIS surface after 15 sec of etch time. Although the measured Cu and In peaks used to calculate the [Cu]/[In] ratio at the times 6, 9 and 12 sec were small, they were still adequate for fitting and can be found in appendix A.

It was expected at first that the [Cu]/[In] ratio would approach values between 0.53 and 0.62 for t$\rightarrow \infty$, as found after HCl etching of CIS with and without CdS in sec. 5.2. However, the values of the [Cu]/[In] ratio here stabilized around 0.40. This same ratio was found for one sample out of 10 in the series discussed in sec. 5.2, making it a possible stoichiometric value for the HCl etched sample. However, a more plausible explanation is that after so many etch steps (i.e. extended time in air) the sample surface became contaminated with hydrocarbons or other O and C containing species which masked the true stoichiometry of the surface and reduced the perceived relative Cu concentration.[8] This correlates to the O and C peaks seen with XPS. The samples in sec. 5.2, on the other hand, had the CdS layers removed with one etch step, thereby revealing the HCl-etched CIS surface without prolonged exposure to air and led to measurements of clean surfaces. This layer of contamination is, however, not the reason for the trends of the [Cu]/[Cd] and [Cu]/[In] ratios seen in fig. 21. In fact, the cover layer would reduce the magnitude of the observed changes, i.e. differences in concentration ratios: electrons with lower kinetic energies have exponentially lower mean free paths than their higher kinetic energy counterparts corresponding to an exponentially higher dampening of the signal from the slower electrons (see fig. 4). Using Mg Kα radiation the electrons from the Cu 2p_3/2 core level have a kinetic energy of approximately 316 eV while those from the In $3d_{5/2}$ and Cd $3d_{5/2}$ core levels have kinetic energies of 804 eV and 848 eV, respectively.

The final curve in fig. 21 shows the S $2p_{3/2}$ binding energy. While also displaying a changing value which stabilizes at 18 seconds, this curve has, in contrast to the other curves, a linear slope. Although this was not expected, it could be the result of the removal of S with the corresponding CdS binding energy and a simple chemical change of the surface S states after contact with HCl combining to give a linear change in the measured S $2p_{3/2}$ binding energy toward $CuInS_2$ values.

The change in the S $2p_{3/2}$ binding energy itself displayed in the curves, which corresponds to a different phase emerging on the sample surface, is more important than the absolute value of the binding energy. Binding energy is a band bending dependent value and, as will be seen in sec. 5.2, the position of the Fermi Level in CIS and CdS band gaps after CdS deposition was not reproducible.

The Cd $3d_{3/2}$ core level binding energy was also observed. Before HCl etching began the binding energy was 404.39 eV and after the first etch step it shifted to 404.50 eV. Thereafter the binding energy of the Cd $3d_{3/2}$ core level stayed in the range 404.54 eV$\pm$0.04 eV for the remainder of the experiment, the total change being comparable to the experimental error of $\pm$0.1 eV. One reason why the S $2p_{3/2}$ core level binding energy changed while the Cd $3d_{3/2}$ core level binding energy did not is because the Cd may be surrounded by S atoms in both materials while the chemical environment of the S changes from exclusively Cd to Cu and In as next neighbors with the occasional Cd atom. Any real change in the Cd $3d_{3/2}$ binding energy may be well under the resolution of the XPS method used to measure the binding energies.

[8] The oxides were not of Cu or In as these would be removed by HCl.

The data points from the last measurement after six hours in HCl were left away for several reasons. Not only would it be inconvenient to extend the time scale to $t = 23677$ sec, but the sample could only be measured with Al Kα radiation, whereas most of the other measurements were taken only with Mg Kα radiation. This measurement was also done more than three months after the point at 2077 sec due to logistical difficulties and the sample was, therefore, highly contaminated. The values for this point are: [Cd]/[Cu]=154, [Cu]/[In]=0.91, [Cd]/[S]=0.003 and S $2p_{3/2}$=161.24 eV. Except for the [Cu]/[In] ratio, these values follow the trends of the previous measurements and show that Cd remains on the CIS surface even after this long etch step. The reason for the anomalous [Cu]/[In] value may be due to a Cu gradient and the different information depths of Al Kα and Mg Kα radiation or to a large preferential removal of In during the long etch step.

An inconclusive attempt to estimate the thickness of the Cd-containing layer was made by contrasting results using Al Kα and Mg Kα radiation on the sample investigated in fig. 21 and is found in appendix B.

5.1.2.2 Valence Band Observations In addition to the core level measurements made using XPS at each point in fig. 21, the valence band was also measured after each etch step. In contrast to the core level measurements above, the change in the valence band from CdS to CIS (figures not shown) was seen after 15 seconds of etch time as opposed to 19 seconds for the core levels. Although the error for the time axis would compensate for this discrepancy, the XPS and UPS observations were made together after every etch step and a correspondence between the two methods was, therefore, expected. The two very different information depths of XPS and UPS were also considered, however, changes should have been seen early in the core levels (XPS) because of the higher information depth. Nevertheless, it was clearly seen that a valence band edge at 0.6 eV stabilized at this time and confirms the removal of CdS from the sample surface. As was the case with the [Cu]/[In] ratio discussed above, it was expected that the valence band edge of this HCl etched CIS would lie between 0.4 and 0.5 eV as it did with the CIS samples measured with UPS directly after total removal of CdS with HCl (sec. 5.2). The discrepancy may be once again attributed to the contaminated state of the CIS surface (sec. 5.1.2.1). Similar increases of the value of $E_f - E_v$ were also observed with KCN etched samples after they became contaminated or were left in air for a significant time (sec. 6.2).

A further discussion of valence band measurements continues in sec. 5.2, where they are used to discuss the position of the Fermi Level (band bending) on the CIS surface before and after CdS deposition along with Cd doping of CIS. Before that, however, we will remain with the topic of Cd diffusion in CIS and attempt to look at this process in further detail.

It has been shown here already that Cd is bound to the CIS surface by a bond different from that found in CdS because the Cd-containing layer left after etching cannot be dissolved by HCl. But if the Cd is so strongly bound to the CIS surface, does it in fact diffuse some distance into the absorber? And if so, which lattice positions does it occupy or does it occupy an interstitial lattice position or build a separate phase?

To answer this question, several experiments were attempted, including those involving

XPS, HAXPES and NEXAFS with both total electron yield and fluorescence detection.

5.1.3 Diffusion: HAXPES Investigation

The depth to which the Cd diffuses beneath the CIS surface, if it diffuses at all, is difficult to measure if the diffusion lengths are short (<3 nm), due to the resolution and minimum information depth of many profiling techniques [91, 92, 93]. Several attempts were made here to at least qualitatively determine if Cd diffuses into the absorber, as many claim, however, this effort was by no means exhaustive and could be improved upon on many levels in the future. The question of diffusion is linked closely to the question of, if diffusion in fact takes place, where the Cd is situated in the CIS lattice. It may, as is most commonly thought, occupy a cation lattice position, most likely that of Cu because the Cu vacancy is the most energetically favorable defect as predicted by theoretical calculations [94]. This is also supported by the Cu vacancies left by the Cu-diffusion out of the CIS and into the CdS. The Cd may of course also occupy a S position although this seems to be almost universally rejected, or it may be found on interstitial sites or may build a separate phase.

The largest experimental difficulty with the cation sites is that the Cd would, in this case, be bound into the CIS lattice solely by Cd-S bonds, making it possibly very difficult to differentiate between measurement signals stemming from these bonds and the signal from CdS. A proper Cd treatment followed by HCl etching would alleviate some of this complication because one could be sure that all of the CdS had been removed. Any resulting Cd signal would be, therefore, from the Cd in the Cd-containing layer left on the CIS surface. On the other hand, as discussed in sec. 5.2, Cu atoms in some kinds of CuS are very easy to differentiate from $CuInS_2$ when observing the Cu L_3 absorption edge although both compounds have Cu-S bonds. However, until now, there is no evidence for such a detectable difference in the case of Cd-S bonds.

Unfortunately, the two experiments done here which did deliver some results involved CIS absorbers with a 50 minute Cd treatment (without thiourea), and *were not* etched afterward with HCl. It must, therefore, be assumed that the surfaces of the investigated samples have a thin (∼1 nm) layer of CdS as shown in [85]. The results may, therefore, contain only information about this layer whose Cd content is much larger than the CIS:Cd layer. In [85] it is also stated that a $Cd(OH)_2$ layer is deposited on top of the thin CdS layer. In this work, the $Cd(OH)_2$ was always removed with an additional NH_3 etch step before measurements were made.

The results can, nevertheless, still be discussed in terms of the possibility of Cd diffusion and may also call into question some of the results found in literature. Furthermore, the sensitivity of the depth profile measurement and associated calculations to the amount of Cd on the surface of the sample is evident and supports the power of the technique.

Fig. 22 shows energy dependent [Cd]/[In] ratios made using increasing incident photon energies at the HIKE end station at BESSY II to investigate a CIS absorber after a 50 minute Cd treatment (this sample *was not* etched in HCl) and relies on the higher infor-

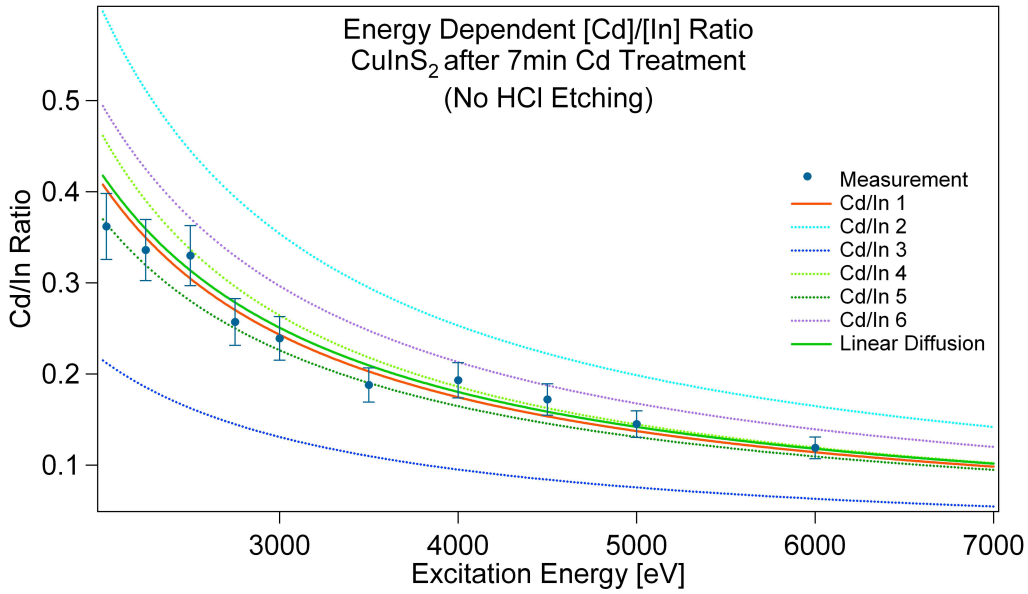


Figure 22: HIKE (HAXPES) energy dependent [Cd]/[In] ratios on a CIS absorber after a 50 minute Cd treatment and calculated curves from modeled depth profiles. The sample *was not* etched in HCl and therefore has a thin (∼1 nm) layer of CdS on the surface. The core levels used here were In $3d_{5/2}$ and Cd $3d_{5/2}$ (see sec. 3.2.7 on quantitative analysis). See table 1 for description of calculated depth profiles.

mation depths associated with higher excitation energies to probe deeper into the sample. The information depths range from about 5 nm at 2010 eV excitation energy to about 20 nm at 6000 eV. The fits were generated using a program written by H. Mönig to investigate Cu(In,Ga)Se_2 layers with the same apparatus [91] which calculates measurement spectra from modeled depth profiles. The peaks used to calculate the data points were In $3d_{5/2}$ and Cd $3d_{5/2}$ and the transmission function was left out of the ratio calculation because of the energetic proximity of the peaks. As in the previous section, the main error in this measurement comes from the determination of the integrated peak surface areas and has a value of ±10%. Other sources of error from the factors discussed in sec. 3.2.7 are systematic and have not not been considered here.

Table 1 contains a list of the assumed concentration profiles modeled in fig. 22. For simplification, sulfur has been left out of the calculations altogether because it was assumed to be present in all layers in its stoichiometric concentration. This corresponds to a [Cd]/[S] ratio of 1 for CdS in the first layer, a [Cu+In+Cd]/[S] ratio equal to 1 in the second layer and a [Cu+In]/[S] ratio of 1 for CIS in the third layer.

The fits in fig. 22 were generated using various Cd concentration profiles. Four of the first five profiles, Cd/In 1, 2, 3 and 5, are based loosely on two models relating to the preparation of the sample, whereby a thin layer of CdS is assumed [85], followed by a thin Cu-free layer [91][9] after which the sample is assumed stoichiometric. Cd/In 4 does not

[9]The results in this dissertation pertain, strictly speaking, only to the Cu(In,Ga)Se_2 system, however, the extension to Cu(In,Ga)S_2 has been considered here.

include the Cu free layer and Cd/In 6 assumes that Cd is also found in the Cu-free layer underneath the CdS layer. In the first 6 simulations, an assumption is made that no Cd diffuses into the stoichiometric CIS.

Table 1: Concentration depth profiles for the calculated spectra found in fig. 22. Sulfur is assumed to be stoichiometric throughout the sample and therefore does not appear in the model.

Profile	First Layer (nm)	Second Layer (nm)	Third Layer (nm)
Cu/In 1	0.00-0.42	0.42-0.78	0.78-50
Conc	Cu=0.0 Cd=1.0 In=0.0	Cu=0.0 Cd=0.0 In=1.0	Cu=0.5 Cd=0.0 In=0.5
Cu/In 2	0.00-0.60	0.60-0.96	0.96-50
Conc	Cu=0.0 Cd=1.0 In=0.0	Cu=0.0 Cd=0.0 In=1.0	Cu=0.5 Cd=0.0 In=0.5
Cu/In 3	0.00-0.24	0.24-0.80	0.80-50
Conc	Cu=0.0 Cd=1.0 In=0.0	Cu=0.0 Cd=0.0 In=1.0	Cu=0.5 Cd=0.0 In=0.5
Cu/In 4	0.00-0.48	0.48-50	-
Conc	Cu=0.0 Cd=1.0 In=0.0	Cu=0.5 Cd=0.0 In=0.5	- - -
Cu/In 5	0.00-0.48	0.48-1.15	1.15-50
Conc	Cu=0.0 Cd=1.0 In=0.0	Cu=0.0 Cd=0.0 In=1.0	Cu=0.5 Cd=0.0 In=0.5
Cu/In 6	0.00-0.24	0.24-0.78	0.78-50
Conc	Cu=0.0 Cd=1.0 In=0.0	Cu=0.0 Cd=0.5 In=0.5	Cu=0.5 Cd=0.0 In=0.5
LinDiff	0.00-0.20	0.20-1.10	1.10-50
Conc	Cu=0.0 Cd=1.0 In=0.0	Cu=0.5-Cd Cd=0.556x+0.611 In=0.5	Cu=0.5 Cd=0.0 In=0.5

Beginning with the first three fits, Cd/In 1-3, it can be seen that the calculated spectrum is highly sensitive to the thickness of the CdS layer on the sample surface. Cd/In 1 assumes a CdS layer of thickness 0.42 nm followed by a Cu-free layer of thickness 0.36 nm and is the best fit of the three profiles. Cd/In 2 and 3 also have a Cu-free layer of thickness 0.36 nm, but the CdS top layer is 0.60 nm in the former and 0.24 nm in the latter. The change in the thickness of the CdS layer leads to drastic changes in the calculated spectra.

Cd/In 4, having a CdS layer of 0.48 nm in thickness and no Cu-free layer, shows a good fit to the data at higher energies, >4500 eV, but tends to overestimate the Cd/In ratio at lower energies.

Similarly, Cd/In 5 with its 0.48 nm CdS layer and rather large Cu-free layer of 0.67 nm, displays a good fit to the data at higher energies, but slightly underestimates the Cd/In ratio the middle and lower energies, although this fit is also very good.

Cd/In 6, having a relatively thin CdS over-layer of 0.24 nm in thickness and a rather thick Cu-free layer of 0.54 nm, this time including Cd so that ([Cd]+[In])/[S]=1, while having a shape similar to the measurements, overestimated the Cd/In ratio at all energies.

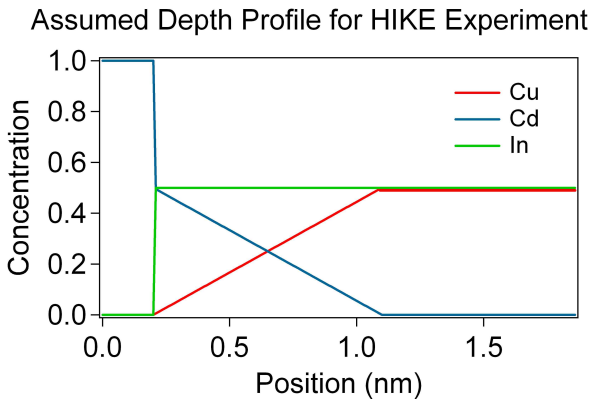


Figure 23: Concentration profile assumed in the simulated spectrum "Linear Diffusion" in fig. 22. The model takes into account the assumption that Cd diffuses into the CIS bulk and occupies Cu lattice positions.

The final simulation, entitled "Linear Diffusion," also includes a CdS over layer, after which the Cu concentration increases linearly to stoichiometric concentrations, while the Cd concentration decreases linearly so that ([Cd]+[Cu])/[In]=1, as can be seen in fig. 23. This simulation takes into account the assertions that Cd occupies a Cu lattice position in the CIS. Although a linear profile does not correspond to normal diffusion distributions usually characterized by an inverse square law, the lack of knowledge about the Cu distribution on the CIS surface makes a completely accurate Cd diffusion profile very difficult. Nonetheless, this fit corresponds well to the measured data and allows for the possibility of Cd diffusion a short distance (∼1 nm) into the absorber. Larger diffusion distances were not modeled here.

A few other facets of this diagram are also of importance. First and foremost, the layer thicknesses considered here are all in the *sub-nanometer* range and show very large changes in the calculated spectra which emphasizes the sensitivity of the measurement method to small changes in the depth profile of Cd. Differences in Cd profiles are real between individual samples and different CdS deposition methods such as CBD, sputtering or MOCVD could be compared. Secondly, the linear diffusion fit, and to a lesser extent Cu/In 6, allow for at least a short diffusion of Cd beyond the CIS surface, if only in the ∼1 nm range. This is, however, significant as the distance corresponds to several atomic layers, and the experiment, therefore, does not exclude that the Cd in fact enters the CIS lattice as opposed to only passivating the dangling surface bonds. In addition, the results here support a CdS layer of thickness $d \lesssim 1$ nm.

The effect of the surface layer of CdS on the HIKE measurement cannot be estimated. A similar measurement to fig. 22 was attempted after the Cd-treated sample was etched

in HCl to remove the thin CdS layer. The result was that no Cd could be detected. In the laboratory with excitation energies from the Mg and Al anodes Cd was seen on this sample but more than 50 scans at 100 ms acquisition time were necessary to successfully separate the Cd peak from the background and the signal-to-noise ratio on the HIKE end station is lower than the laboratory X-ray sources. Also, the absorption cross sections at the higher excitation energies using HIKE are lower than in the laboratory. This means that the amount of Cd on or in the CIS surface after etching is significantly less than the Cd contained in the CdS surface layer, resulting in two scenarios. If the etching only removes the thin CdS layer from the Cd treatment and none of the Cd in or on the CIS, then the signal contributing to the ratios in fig. 22 comes exclusively from this CdS layer, as Cd remaining after etching provides no signal. More probably, though, as supported from the ever climbing [Cd]/[Cu] ratio in fig. 21, is that the HCl etching removes not only the thin CdS layer but also some of the Cd in or on the CIS, probably through removal of the some of the CIS itself. In this case, some of the Cd originally present in the CIS, but removed by the etching may contribute to the signal in fig. 22. Because it is not known how much of the CIS:Cd layer is removed through HCl etching, the precise influence on the measurement cannot yet be derived.

It was, however, estimated that when using the Cd $3d_{5/2}$ core level, the detection limit of the Cd in the laboratory would be ∼0.3% Cd in the material volume contained within the information depth of the signal which is approximately 3 nm. Two further calculations to determine the amount of Cd remaining on the surface after HCl etching were also carried out and resulted in quantities similar to this. Comparing the Cd $3d_{5/2}$ core level signal strengths from pure CdS to the signal from the point at 539 sec in fig. 21, it was found that at 539 sec there was ∼0.2% Cd on the sample surface. Using the same temporal point and its [Cu]/[Cd] and [Cu]/[In] ratios along with the assumption ([Cu]+[Cd]+[In])/[S]=1, a Cd concentration on the sample surface was calculated to be ∼0.66%. Thus, after HCl etching, the amount of Cd left on the sample surface is in the same order of magnitude as the detection limit and corresponds roughly to 0.1 atomic layers of Cd. Considering the afore-mentioned lower signal-to-noise ratio at the HIKE end station, it is not surprising that the Cd signal was lost in the background.

The discussion of layers thinner than 1 atomic layer or even sub-nanometer layers is difficult due to the surface morphology of CIS (see fig. 4) because the surface roughness of the sample is in the μm range. This must always be considered when analyzing the results of this is a depth-profiling technique.

5.1.4 Diffusion: X-Ray Absorption Investigation

Staying with the same sample as in the HIKE measurement above, we move to the question of how the Cd is bound into the CIS lattice. Attempts were made to asses the chemical surrounding of Cd atoms using NEXAFS and EXAFS (see sec. 3.4). In this case, as with the HIKE measurements, no signal was detectable from samples coated with Cd and then etched with HCl. The sample with a 50 minute Cd-treatment (no thiourea, no HCl etching) was, however, measurable.

Fig. 24 a) shows several different Cd L_3 absorption edges from these samples. The uppermost spectrum is a FEFF calculation (see sec. 3.4) of the edge from CdS while the remaining spectra are measured. The calculated spectrum is shifted to match the bottom of the absorption edge to those of the measured spectra, the reason being the problematic reproducibility of the excitation energy. A detailed discussion of this is given in sec. 7.2.1. The first and second measurements used fluorescence and total electron yield signals, respectively, from a CIS absorber with a thick (∼35 nm) CdS top layer while the next spectrum is from an absorber subjected to a 50 minute Cd treatment (*not etched* in HCl). The final spectrum is a smoothed version of the spectrum from the Cd-treated sample. The measured spectra are not shifted in energy.

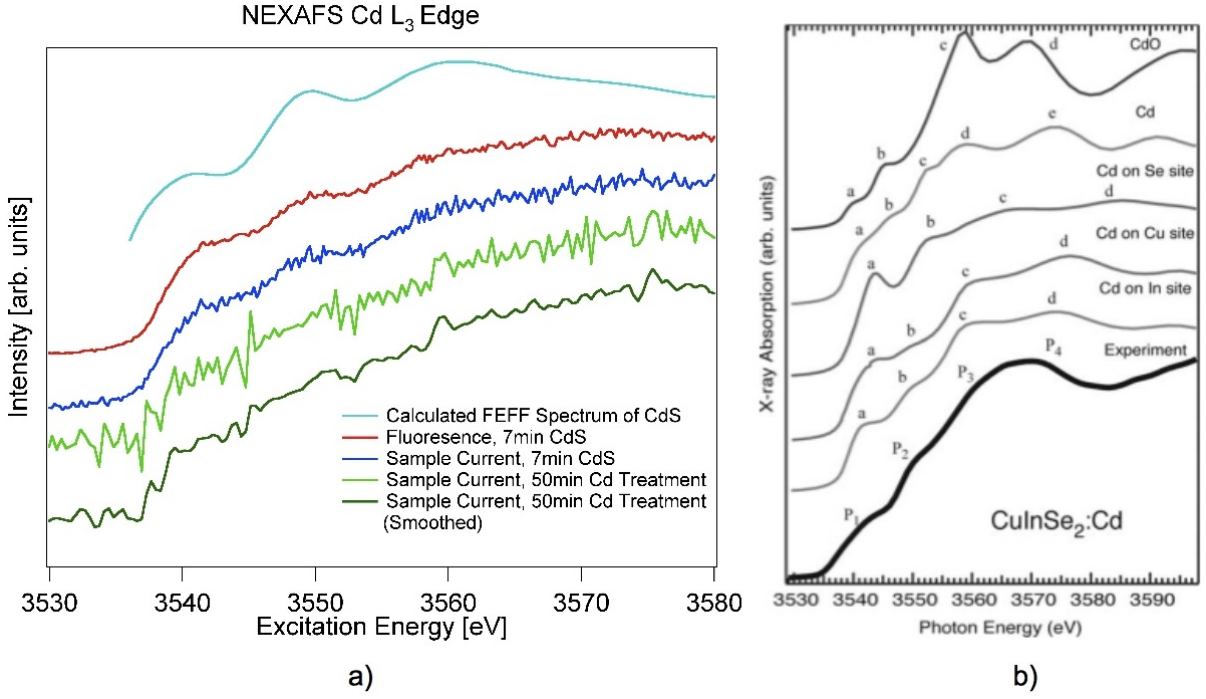


Figure 24: a) A calculated FEFF Cd L_3 absorption edge for CdS, shifted to match the absorption edges of the measured spectra, is compared to measurements of the same edge on CIS absorbers with a thick (∼35 nm) CdS top layer (fluorescence and total electron yield signals), after 50 minutes Cd treatment (only total electron yield) as well as a smoothed version of the latter spectrum. Spectra are normalized and vertically shifted for clarity. b) Calculated (thin lines) and measured (thick line) Cd L_3 absorption edges on Cd-treated CIGSe from [22]. See further explanation in text.

The reason for the poor quality of the latter spectrum is due to the small amount of Cd contained in the Cd-treated sample, as discussed in the HIKE section above. This sample was only measurable in total electron yield mode, as the high information depth attainable with fluorescence caused the signal from the Cd to be lost in the noise, supporting the assertion that the Cd stays near the surface of the CIS. It must, however, be pointed out that the information depth of the total electron yield signal is tens of nm, which is no longer surface sensitive when compared to other methods in this thesis.

Despite this, the similarity of all the spectra in fig. 24 a), including the calculated spectrum, is immediately evident, including all three post edge features. The reason for this is probably that all signals come from CdS with, in the case of the Cd-treated sample, a small contribution from the Cd bound on or in the CIS. This signal is also technically contained in the fluorescence signal from the sample with the thick CdS layer, but is totally negligible here.

A similar experiment was performed by [22] on Cd-treated Cu(In,Ga)Se_2 and some of the results are displayed in fig. 24 b). The treatment was also done wet-chemically, albeit, using slightly different precursors. Nonetheless, a thin CdSe layer can also be expected here analogue to the CdS layer found on CIS. The treated CIGSe samples were, however, not etched in any way to remove the possible CdSe layer. Here it was concluded from Cd L_3 FEFF calculations for CdO, Cd, CIGSe:Cd_{Se} (Cd on Se sites), CIGSe:Cd_{Cu} (Cd on Cu sites) and CIGSe:Cd_{In} (Cd on In sites) that the Cd must occupy a cationic lattice position in the CIGSe crystal. This is not only due to the similarity between the measurements and the calculated spectra of CIGSe:$Cd_{Cu,In}$, but also due to the large post edge feature at 3543 eV labeled "*a*" in the calculated CIGSe:Cd_{Se} spectra (fig. 24 b)) which is missing in the measured spectrum. However, after considering the above discussion, it is most probable that, similar to the results of fig. 24 a), CdSe was measured in this case instead of CIGSe:$Cd_{Cu,In}$, CdSe looking like CIGSe:$Cd_{Cu,In}$ due to the similarity of Cd-Se bonds in both lattices. The Cd content in the CdSe top layer most likely dwarfs the amount of any Cd on or in the CIGSe. Furthermore, it is interesting to note that no calculated CdSe spectrum is included in [22] and a calculated CdS spectrum is, therefore, included in this thesis. The similarity between the calculated and measured spectra shown in fig. 24 a) and the calculated CIGSe:$Cd_{Cu,In}$ spectra and the measured spectrum in fig. 24 b) can clearly be seen, including all three post-edge features, labeled a, b and c or P_1, P_2 and P_3 in fig. 24 b).

5.1.5 Diffusion: Further Absorption and Fluorescence Experiments

No signal from the Cd L_3 absorption edge was attainable from the Cd-treated CIS sample after HCl etching. In addition, it was attempted to measure the Cd K absorption edge at 23 keV on Cd-treated samples, both HCl etched and non-etched as well as on a CIS absorber with a thick CdS top layer. Although the latter sample gave a signal of good quality, no signal was obtained from either of the two former samples. The success of this experiment may have made possible the direct Fourier transformation of the spectrum to calculate binding lengths of the atoms surrounding the excited Cd atom, thus, giving information about the chemical environment of that atom.

Further experiments will continue in this area.

Energy dispersive fluorescence experiments with samples subjected to the same preparation were also preformed with similar results. Here it was attempted to look specifically at the fluorescence resulting from the transition of electrons from the Cd 4d states into empty S 2p states (if Cd occupies a cationic lattice site) and from transitions from Cd 4d

to empty Cu 2p and In 3d levels (If Cd occupies an anionic site).

Although the Cd was again detectable for CIS with a thick CdS layer, no differences were seen between a KCN-etched CIS reference and CIS with 50 minutes of Cd-treatment (both unetched and HCl-etched), that is, there was again no Cd signal from the latter sample.

5.2 CBD-Induced Band Bending and Cd Doping in $CuInS_2$

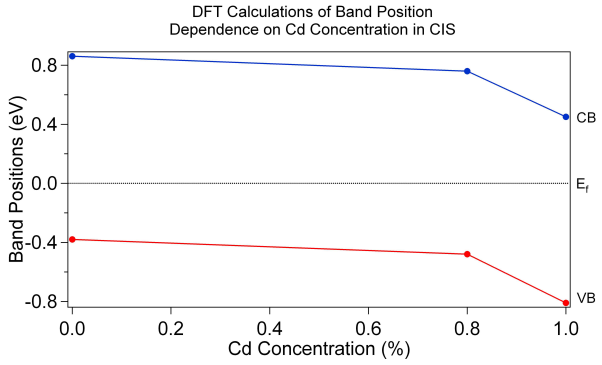


Figure 25: Positions of the valence and conduction band edges relative to the Fermi Level as a function of Cd concentration x calculated with density functional theory. At 0% Cd, the material is p-type and already with 1% of Cu replaced through Cd, the material becomes n-type.

Another reason for the HCl etch experiments is to discover what effect the Cd has when on the CIS surface or after it has diffused into the CIS lattice. It is thought that the Cd occupies a cationic position in the CIS lattice, most likely a Cu position [79, 89]. Due to one extra valence electron of Cd, it would dope the CIS crystal n-type if it were to land on a Cu lattice position [95]. On the other hand, if the Cd stays only on the surface and does not diffuse, the deposition process may result in the pinning of the Fermi Level (see sec. 4.1.2) at a position in the CIS band gap nearer the conduction band edge than is found after the KCN etching, making the CIS surface more n-type.

Support for a "doping" action from the Cd is shown in fig. 25. This first principles Density Functional Theory (DFT) calculation,[10] although it contains only three points, shows clearly that Cd on Cu lattice positions in CIS will dope the crystal n-type. At 0% the CIS is of p-type and with 1% of the Cu replaced by Cd the crystal is n-type showing the critical impact of Cd in CIS. This simple model supports the intuitive conclusion that Cd(II) filling Cu(I) positions in the CIS lattice will dope the crystal n-type although some suggest one Cd(II) atom replaces two Cu(I) atoms [84]. Theoretical calculations for some chalcopyrites have shown, however, that the doping action of divalent atoms such as Cd, Zn and Mg can be compensated by Cu vacancies [95] although this does not effect all chalcopyrites equally [89, 95].

The pinning scenario is supported by the fact that any change in the Fermi Level position on the CIS surface was completed within the first 40 seconds of the CBD, meaning that an increased amount of time for Cd diffusion into the CIS did not decrease the p-type character of the CIS surface. This was determined after it was observed that when several CIS substrates were coated with CdS using the *same* chemical bath, the shortest

[10]The details of the DFT calculation are found in appendix C

deposition time being 40 seconds, the observed change in Fermi Level position during the deposition was the same for all samples. However, as will be discussed below, the amount by which the Fermi Level shifted on the CIS surface before and after CdS deposition was not reproducible when comparing depositions from *different* chemical baths.

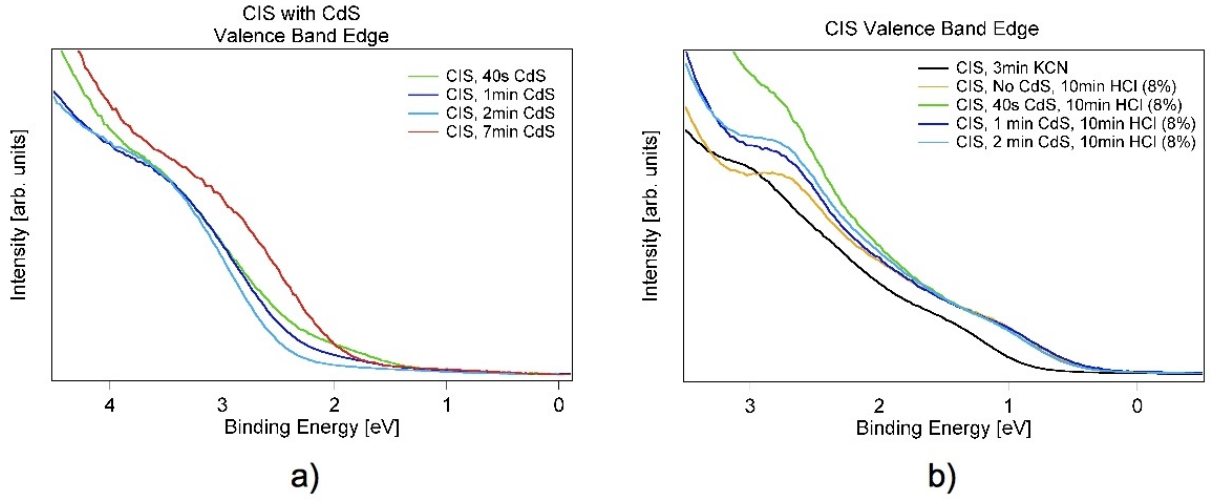


Figure 26: He I UPS valence band spectra of a) CdS on different CIS substrates from different depositions and b) the same CIS absorbers with the 40 sec, 1 min and 2 min CdS layers after the CdS has been removed in 8% HCl. b) also shows a KCN-etched as well as a KCN-HCl (no CdS) CIS reference. The differences in the positions of the band edges in a) can be clarified through differing amounts of band bending on the underlying CIS surface. In b) the prominent Cu 3d peak at 3 eV is evidence for a Cu-richer surface after HCl etching.

Fig. 26 a) shows valence band spectra of several CIS samples after CdS depositions of duration 40 sec, 1 min, 2 min and 7 min, corresponding to layer thicknesses of about 0.7, 1, 2.5 and 35 nm, respectively. All CdS layers were made using different chemical baths.[11] Fig. 26 b) shows the same samples which had the 40 sec, 1 min and 2 min CdS layers, but after the CdS layers had been etched away with 8% HCl. Part b) also contains spectra from a KCN-etched CIS reference and a sample etched in KCN and then in HCl without CdS deposition. Here, as well as later in this section, the results from the last section are applied: CIS samples retain a Cd-containing layer after CdS removal with HCl.

Beginning with part a), the CdS spectra all have a similar appearance apart from a decrease in background signal intensity with deposition time at binding energies lower than the valence band edge, between about 1.5 and 2.5 eV (black arrow in figure). This change is due to increasing CdS layer thickness leading to increased absorption, and, therefore, attenuation, of the signal from the underlying CIS. The other noticeable difference is the shift in band edge positions which can be clarified through differing amounts of band bending on the CIS surface between different CdS depositions. A change in the amount

[11] The samples with different CdS thicknesses were originally made to determine if CdS deposition time had any effect on the CIS surface after CdS removal with HCl. However, because any change in band bending on the CIS surface due to CdS deposition is completed after at most 40 seconds, these samples can also be used to compare Fermi Level positions from different depositions.

of band bending on the CIS surface corresponds to a change in the Fermi Level position in the CIS band gap (sec. 4.1.1). This can be seen indirectly with XPS through a change in the CIS core level energies and the assumption that the energy difference between the valence band edge and the core levels is fixed. But, because the valence band offset between CIS and CdS remains the same, as will be shortly discussed, differences in the amount of surface band bending on the CIS will correspond to an equal shift in the CdS core levels, as the Fermi Level will also change its position by an equal amount in the CdS band gap. This technique is discussed in greater detail in chapter 6 where it is compared to another method called near-UV constant final state.

The samples with the 40 sec and 1 min deposition times have valence band edges at 2.20 and 2.25 eV, respectively, while the other two samples are shifted noticeably away from these values. The sample with 2 min deposition time has a band edge at 2.45 eV and the sample with 7 min, the thickest CdS layer, is at 1.90 eV. By using the core levels measured on the CIS substrate before and after CdS deposition the additional band bending on the CIS surface can be ascertained and the band offset estimated with the equation

$$\Delta_{vb} = E_{vb,CdS} - E_{vb,CIS} - E_{bb} \tag{20}$$

where the Δ_{vb} is the valence band offset, $E_{vb,CdS}$ and $E_{vb,CIS}$ the measured positions of the valence band edges of CdS and CIS, respectively, and E_{bb} the change in core level position on the CIS surface due to the additional surface band bending caused by the CdS deposition. We will assume in all cases that the valence band position of the CIS before the CdS is at $E_{vb,CIS}$=0.85 eV as measured on the KCN etched sample in fig. 26 b), although this is slightly higher than the normally observed value.[12] However, it is, of course, possible that this slightly less n-type surface was a characteristic of this particular batch from which all of the samples shown in fig. 26 came.

We have, then, for the samples with 40 sec, 1 min and 2 min deposition time the following results when the remaining terms in eq. 20 are replaced with their measured values:

$$\Delta_{vb,40\,sec} = 2.20\,eV - 0.85\,eV - 0.15\,eV = 1.20\,eV \pm 0.20\,eV \tag{21}$$

$$\Delta_{vb,1\,min} = 2.25\,eV - 0.85\,eV - 0.15\,eV = 1.25\,eV \pm 0.20\,eV \tag{22}$$

$$\Delta_{vb,2\,min} = 2.45\,eV - 0.85\,eV - 0.40\,eV = 1.20\,eV \pm 0.20\,eV \tag{23}$$

The correspondence of the shift in Cd core levels to the shifts of the Cu and In core levels points, again, to band bending.[13] These results should be compared to the similar results

[12]The "normal" value is $E_{vb,CIS}$=0.70-0.75 eV. This would add 0.10 eV to the band offset , but the new value would still be in agreement with the values in chapter 6. The weak points of the assumption that valence band edge and core level shift parallel are indeed critical and are discussed in sec. 6.1 along with other aspects of this method.

[13]The core level shifts from the sample with 2 min CdS were taken only from the In and Cd $3d_{3/2}$, In and Cd 3p, In and Cd $4d_{3/2}$ and In and Cd $4d_{5/2}$ levels because the Cu levels were the same as the

obtained in chapter 6 for the XPS/UPS method.

The sample with the 7 minute CdS deposition time, at 35 nm layer thickness, was so thick that the underlying CIS core levels could no longer be measured and is thus a little trickier to evaluate. However, if we look at the difference in Cd core levels between this sample and samples 2-4 and compare them to the difference in the corresponding valence band edges, we find that although there is a small discrepancy the shifts are similar:

Table 2: Values for the differences between electronic positions of the sample with 7 minutes CdS deposition time and the other three samples in fig. 26 a), as noted in the column on the left. The differences in valence band positions are denoted ΔE_{vb}, the differences in core level positions with ΔE_{core}.

Sample	ΔE_{vb}	ΔE_{core}
40 sec	0.30 eV	0.40 eV
1 min	0.35 eV	0.45 eV
2 min	0.55 eV	0.80 eV

This parallel shift in levels again points to a shift in the position of the Fermi Level in E_g although chemical shifts are also present. Due to the extremely thin CdS layer, it is more likely that this shift comes from a difference in the Fermi Level position on the CIS surface causing a shift in the Fermi Level position of the buffer layer and not from band bending in the buffer layer itself.[14]

The author must admit, however, that a difference in surface band bending on the order of half an eV is quite extreme and may not be accounted for through small changes in deposition conditions. In addition, the position of the valence band edge of the thickest CdS layer, being at 1.90 eV means that the valence band position in the CIS can be at a maximum of 0.70 eV in order to keep the 1.20 eV band offset, implying band bending *toward a more p-type surface* when compared to the value of 0.85 eV for the KCN-etched CIS sample found in fig. 26. This is the only observation of this trend in this thesis. Of course, assuming a CIS valence band position of 0.85 eV on this CIS surface (i.e. no deposition-induced band bend), the band offset of 1.05 is still inside of the error of these measurements of ± 0.20 eV discussed in chapter 6 for the XPS/UPS method. It must, however, be kept in mind that this sample had the thickest CdS layer and we are thus comparing the electronic states on the CdS surface with the states on the CIS surface. Although this keeps with the assumption that there is no band bending in the buffer layer (sec. 6.2), it neglects possible chemical changes in the CdS surface which is deposited after

samples with 40 sec and 1 min deposition times. This points to some kind of chemical shift in addition to band bending and has been seen in literature [90]. The calculation of the valence band offsets in the samples with 40 sec and 1 min CdS layers included the core levels Cu $2p_{3/2}$, Cu $3p_{1/2}$ and Cu $3p_{3/2}$

[14] It is the view of some that the Fermi Level position on the CIS surface after CdS deposition is carried on into the CdS and that no band bending occurs in the buffer layer because it is so thin (sec. 6.2). In other words, the extremely small amount of charge in the buffer layer is not enough to influence the position of its own Fermi Level and the "doping level" of the CdS is determined by the position of the Fermi Level on the surface of the absorber. This was investigated here in sec. 6.2.

seven minutes as compared to the other three samples which had shorter deposition times.

It must be concluded then that although the valence band offset between CIS and CdS is the same for every individual CdS deposition within experimental error, the Cd, or more generally, the CdS deposition process, does not pin the Fermi Level at a specific electronic position on the CIS surface which is critical for solar cell functionality. If this were the case, the observed band bending on the CIS surface and, therefore, the position of the Fermi Level in the CdS, would be reproducible.

Moving on now to fig. 26 b), the differences between the KCN etched sample and the other samples after removal of the CdS can be clearly seen.

In contrast to the KCN-etched CIS surface, the HCl etched surface is highly reproducible.[15] In addition to the samples whose measurements are presented here, many other CIS absorbers etched with HCl after KCN etching had not only very similar valence band positions, $0.40\,\mathrm{eV} < E_f - E_b < 0.50\,\mathrm{eV}$, but the form of the entire upper valence band was the same. This can be compared to the spread in the KCN-etched CIS samples: $0.55\,\mathrm{eV} < E_f - E_b < 0.90\,\mathrm{eV}$

The HCl-etched CIS surface shows a strong feature at 3 eV which is much weaker and at a slightly different energy in the spectra of the KCN-etched samples. These are the Cu 3d electrons, here more prominent due to the increased Cu concentration on the CIS surface. XPS measurements showed surface Cu-concentrations higher than on KCN-etched CIS. [Cu]/[In] ratios were routinely between 0.53 and 0.62 for HCl-etched samples while this ratio was between 0.25 and 0.30 for KCN-etched samples. While the latter ratio is quite low, Cu-poor surfaces are also found in literature [96]. The amount of Cu therefore doubled after the HCl etching and, as discussed in [94, 97], the increased Cu concentration leads to an increased repulsion between the S 3p and Cu 3d states (p-d repulsion) which leads to the shift of the valence band edge toward the Fermi Level.

Because the forms of the valence band and edge positions are the same for both HCl-etched samples with no previous CdS deposition *and* samples which had CdS removed by the HCl etching (which still have a Cd-containing surface layer),[16] it must be concluded that the Cd does not n-dope the CIS surface as the valence band edge is at the same position in all samples. In fact, the movement of the valence band edge toward E_f, when compared to KCN-etched samples, supports a more p-doped surface, although this is an effect of the HCl etching.

[Cu]/[S] ratios also increased by the HCl etch step to between 0.25 and 0.33, compared with 0.18 for KCN-etched samples. This leads to the conclusion that In is preferably removed by HCl etching, at least at first, with perhaps some S following, resulting in some phase of $Cu_{2-x}S$ on the surface.

To investigate this, other UPS valence band spectra were employed along with NEXAFS

[15] This is supported by the binding energies and surface stoichiometries measured with XPS on the same samples which will discussed shortly.

[16] As a first step with all samples from fig. 26, they were etched in KCN solution.

measurements which are very sensitive to some phases of CuS.

Fig. 27 shows several Cu L_3 absorption edges from unetched, KCN-etched and HCl-etched CIS absorbers. The very prominent pre-edge feature at 930 eV (black arrow) in the unetched sample is caused by the presence of a phase with a partially empty Cu 3d orbital (Cu $3d^9 4s^0$) [18], the empty 3d state being in the conduction band. Even very small amounts of this phase on the surface can contribute a large pre-edge feature to the absorption spectrum due to the high oscillator strength between the Cu 2p and Cu 3d states [18, 21]. These phases can include any compound with Cu bound as Cu (II) such as Cu(II)O and some kinds of $Cu_{2-x}S$ where there is at least a partially open 3d orbital.

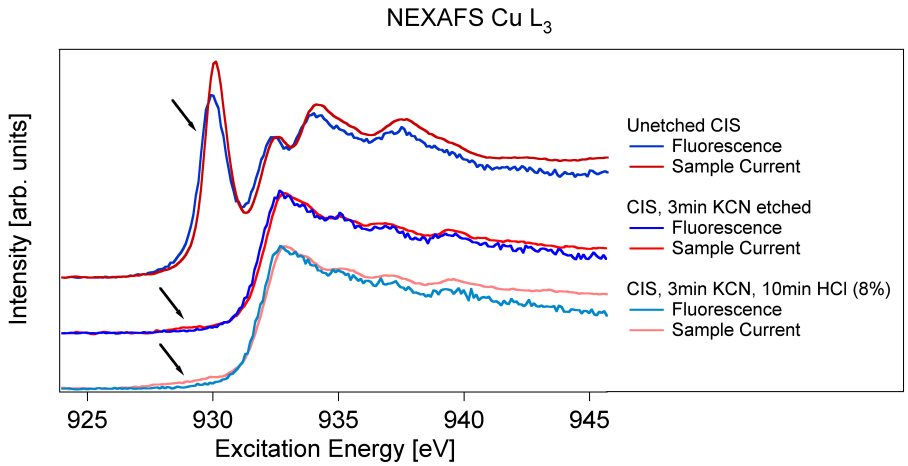


Figure 27: Cu L_3 absorption edges (blue is X-ray fluorescence, red is total electron yield) on unetched, KCN-etched and HCl-etched CIS samples. The large feature at 930 eV in the unetched spectrum (black arrow) is due to the CuS and CuO phases on the surface of the sample with a Cu $3d^9 4s^0$ valence structure. The HCl etching, although it produces a Cu-richer CIS surface than found on KCN-etched CIS, produces no phase with a Cu $3d^9 4s^0$ valence structure. The spectra are normalized to the peak at 932 eV following the pre-edge feature and are shifted vertically for clarity.

Therefore, when looking at the other two spectra in fig. 27, it can be seen that neither the KCN-etched CIS nor the HCl-etched CIS contains any amount of this Cu $3d^9 4s^0$ phase on the surface in concentrations corresponding to total surface coverage. It can be seen that the red total electron yield curves have indeed a small feature at about 930 eV (marked by black arrows). It is not thought that this Cu(II)-containing phase is a result of HCl-etching but is rather due to a slightly contaminated surface, most probably from Cu(II)O, as is often seen [21].

Several other features in the spectra in fig. 27 are noteworthy. The reduced and/or absent pre-edge feature at 930 eV in all three spectra with fluorescence signal can be explained by the different information depths of the two signals. The relatively bulk-sensitive nature of X-ray fluorescence detects proportionally less of the Cu(II)-containing phase compared to total electron yield because this phase is not present in the bulk of the absorber. Also, the slight deviation in the position of the absorption edges measured by fluorescence and

total electron yield on each sample shows a slight change in the energy between the Cu 2p core level and the final state of the absorption event when moving deeper into the sample bulk. This will be considered again in chapter 7.

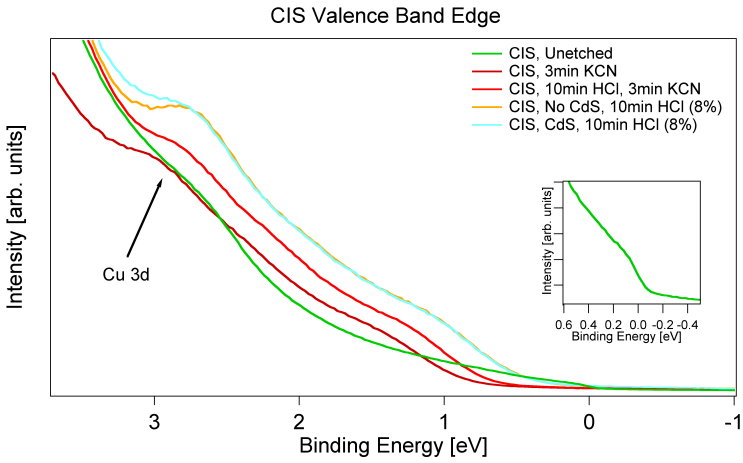


Figure 28: UPS valence band measurements of unetched, KCN-etched, HCl-etched and HCl-KCN-etched CIS absorbers. The metallic nature of the unetched sample can be clearly seen (Fermi Level inset) as well as the effect of the KCN etch step coming again after HCl etching. The sample surface of the HCl-KCN etching lies between that of the only HCl and only KCN etched samples.

Further investigation of the HCl etched surface was done with UPS and the valence bands of several samples.

Fig. 28 shows the valence band edges of an unetched CIS sample, a KCN-etched sample, an HCl-etched sample and a sample etched in KCN, then HCl and then again in KCN (HCl-KCN-etched). The unetched sample with presumably CuO, CuS and Cu_2S phases on the surface clearly has a metallic nature as can be seen from the small Fermi Level at 0 eV (see inset). In this spectrum as well, a somewhat washed-out Cu 3d feature is visible at 3 eV. While $Cu_{2-x}S$ is known to be metallic for some values of x [98, 99], the resistivity values can vary over several orders of magnitude and depend on the purity of the material. Metallicity is therefore not a criterion for the existence of $Cu_{2-x}S$. Additionally, the problem with ascertaining the value of x in the $Cu_{2-x}S$ discussed here is that it is on a $CuInS_2$ substrate making it difficult to determine how much of the Cu and S signals come from the substrate and how much from the $Cu_{2-x}S$.

At the other extreme, having a valence band edge at 0.85 eV, is the valence band edge of a KCN etched CIS absorber (this is the same spectrum shown in fig. 26). As usual, the Cu 3d peak is rather weak and shifted to slightly higher binding energies due to the Cu-poorer surface and the reduced repulsion between the S p and Cu d orbitals.

In between these two extremes are spectra from samples etched in HCl, one with the Cd-containing surface layer and one without, as well as a sample etched in HCl and subsequently in KCN. It can immediately be seen, as in fig. 27, that the surface created by the HCl etch step is not the same as the unetched surface as the valence bands look very different.

However, the valence band edge of the sample etched in HCl and then KCN looks very similar to the valence band of the CIS sample etched only in KCN. The thought here was that, if the Cu-rich phase produced by the HCl were indeed CuS, it must be removable by a further KCN etch step and the valence band should return to one similar to the KCN etched sample.

It can be seen that the HCl-KCN sample has a valence band edge at 0.70 eV, very typical for KCN-etched CIS. The Cu 3d peak at 3 eV is only slightly more prominent than the Cu 3d peak in CIS and is shifted to slightly lower binding energies. Because the KCN-etched CIS sample measured here showed slightly anomalous values (fig. 26 b)), it is possible that after a subsequent HCl and KCN etch step, the surface does not return to its exact original form.

Therefore, it seems that the HCl etching produces a nonmetallic $Cu_{2-x}S$ phase on the CIS surface with a Cu $3d^{10}4s^0$ electronic structure because the pre-edge feature at 930 eV in fig. 27 is not found after HCl etching. It is also possible that the surface of HCl-etched CIS is a layered system, for example: $Cu_{2-x}S/CuInS_2$(Cu-richer)/$CuInS_2$(Cu-poorer).

A HCl and subsequent KCN etch step may, therefore, be a method to achieve reproducible CIS surfaces, because the HCl-etched CIS surface layer was always found to be the same.

5.3 Conclusions about Junction Formation

During formation of the $CuInS_2$/CdS heterojunction, a Cd-containing layer (CIS:Cd) is formed on the surface of CIS. Although the Cd in this layer most likely occupies cationic lattice positions, the resulting CIS:Cd compound is different than CdS because this Cd-containing layer is not soluble in HCl.

The Cd may also diffuse into the CIS while at the same time Cu diffuses into the CdS layer during the CBD process. The Cu does not, however, reach the surface of a full ∼35 nm CdS buffer layer.

Observations of the Fermi Level on the CIS and CdS surfaces after different CdS depositions resulted in the conclusion that the amount of CBD-induced band bending on the CIS surface is not reproducible. This led, in turn, to the conclusion that the CdS deposition does not pin the Fermi Level at a specific position on the CIS surface important for the solar cell. The amount of band bending in the constituent parts of the solar cell may, therefore, first be defined after the deposition of the window layer.

HCl etching of CIS layers with and without CdS led to the same, reproducible surface which was Cu-richer than the KCN-etched CIS surface. Moreover, both samples had the same surface Fermi Level position. Because earlier results had confirmed that Cd remained on the CIS surface after CdS deposition and subsequent HCl etching, it was concluded that the CIS surface is not doped by Cd.

The one characteristic of the junction which was reproducible was the valence band offset. An offset of $\sim 1.25\,\text{eV} \pm 0.20\,\text{eV}$ for $E_{v,CIS} - E_{v,CdS}$ was consistently found using the indirect XPS/UPS method for the junction, independent of the position of the Fermi Level and is supported by the reproducibility of solar cells made using this absorber/buffer junction. This reduces the possible roles of the CdS in the $Cu(In,Ga)S_2$ solar cell to lattice matching, interface defect reduction or to optimizing the band alignment between CIS and the

window layer.

NEXAFS and EXAFS studies of the bonding environment of Cd in CIS were inconclusive because no signal from Cd could be obtained in samples where CdS had been removed by HCl etching. It was, however, reconfirmed, that the Cd-treatment of CIS surfaces forms a thin layer of CdS which must be removed before the CIS:Cd layer can be studied.

In the next chapter, the electronic characteristics of the completed $CuInS_2$/CdS junction, specifically the valence bands and the valence band offset, will be studied with two methods and the results compared. At the end of the chapter Ga is introduced into the system and preliminary band offset measurements on the Cu(In,Ga)S_2/CdS and $CuGaS_2$/CdS junctions are presented in order to investigate the dependence of the valence band offset on Ga concentration.

6 $CuInS_2$ and CdS Valence Bands and the Valence Band Offset

The valence band positions and the valence band offset of this system which will be investigated in this chapter are interesting for two reasons, although the link to the functionality of the solar cell is an indirect one. First, the simple material characteristics of such a junction, as mentioned in sec. 4.2, are interesting from a materials science perspective in order to more fully understand the behavior of heterojunctions. Second, and more pertinent to the solar cell discussed here, the valence band offset gives a first approximation about what the conduction band offset may look like (this topic is discussed further in chapter 7).

The conduction band offset, as illustrated in fig. 19, is crucial to the cell's voltage and current output due to the effective band gap (fig. 10) and charge carrier transport characteristics. The best alignment is either no offset or a spike as long as it is smaller than about 300-400 meV [80]. The spike occurs when the conduction band of the absorber lies below (higher binding energy) that of the CdS. A cliff, on the other hand, occurs when the conduction band of the absorber lies above (lower binding energy) that of the CdS resulting in an effective reduction of the band gap at the interface by the size of the cliff and can increase dark current and limit photovoltages [1, 57]. Although the offset itself can vary depending on the stoichiometry of the absorber, the system CdS-$CuInS_2$ as used in solar cell applications is expected to have a cliff of 200-400 meV [57, 81, 100, 101], which may contribute to the cell's moderate 11% efficiency [58]. The offset, however, may depend heavily on the crystallinity of the CIS and the method of preparation [52, 81].

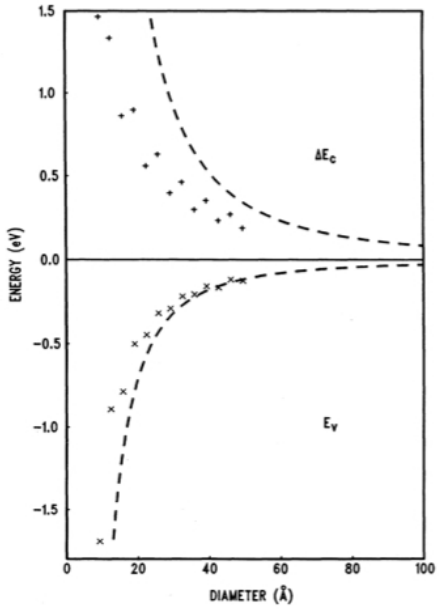


Figure 29: The positions of the valence (×) and conduction (+) band edges in CdS as a function of crystallite size as resulting from the tight-binding model. Dashed lines represent the effective-mass approximation calculations. The energy (y-) axis is the deviation from bulk values, E_g=2.5eV. Taken from [103].

The estimates of the conduction band offset here are, of course, made by adding the optical band gaps of the $CuInS_2$ and CdS to the measured valence band offset. This must be done with caution because there is no reason to assume that the surface band gaps of the two materials are the same as the optically measured bulk values. And the surface band gap values are the important quantities when investigating junctions. The possibility of a difference between the bulk and surface CIS band gap values, possibly due to the Cu depletion at the surface and the Cu 3d-S 3p repulsion, has been well discussed in literature [94, 97, 102].

Furthermore, it has been shown that the quantum size effect in CdS (fig. 29) begins to widen the band gap (both the valence and conduction bands move) in crystallites smaller

than 10 nm [103]. The CdS layers in this section are all less than 7 nm thick, meaning that the crystallites must be quantized in at least the vertical direction. The actual energies of the "bands" in these crystallites may, therefore, vary, the measured valence band edge being an average over all crystallites forming the layer's surface. And, as we will see, the measured valence band edge indeed lies at higher binding energies than many literature values, but not all. The conduction band position, was, however, not measured on these layers, leaving its energetic value open to question, especially in light of the quantum size effect on the conduction band and how this relates to the full buffer layers.

The CIS valence band is comprised of Cu 3d-S 3p antibonding states, Cu 3d nonbonding states, Cu 3d-S 3p bonding states and S 3s states [105] whereas the CdS valence band is constructed of S 3s, S 3p and Cd 4s states [106]. According to the common ion rule (sec. 4.2.2) it might be expected that the valence band offset should be relatively small, which, as will be shown is another reason to abandon this model. This is also supported by more modern theoretical results [97, 104]

While the majority of this chapter revolves around the $CuInS_2$-CdS junction, sec. 6.4 at the end of the chapter contains a short discussion on the offset in the Cu(In,Ga)S_2-CdS and $CuGaS_2$-CdS systems. These junctions were, however, by no means investigated to the extent of the $CuInS_2$-CdS junction.

6.1 The Direct and Indirect Methods of Valence Band Offset Determination (XPS/UPS and CFS)

The valence band offset was determined here using a common method combining XPS and UPS data as well as a method used heretofore only on the a-Si/c-Si heterojunction called near-UV constant final state.[17] The results of each method are compared and the advantages and disadvantages of each method discussed.

The specifics of the usual method of determining band offsets using combined XPS/UPS (referred to hereafter as "the indirect method" of band offset measurements) are explained elsewhere [100, 107]. Briefly, after the initial measurement of the bare substrate valence band edge, any change in the position of the edge after deposition of a top-layer is accomplished through observation of substrate core levels through the top-layer. Although able to correct for energetic shifts on the substrate due to band bending, this method is unable to account for chemical shifts due to, for example, changes in stoichiometry resulting from the wet-chemical deposition of the CdS because an assumption is made that the difference in the binding energies between the CIS valence band edge and the various core levels is fixed. The NH_3 in the chemical bath is known to cause a relative increase in the Cu concentration on the Cu(In,Ga)Se_2 surface through preferential removal of In and Ga [108, 109] and this effect has also been observed here for $CuInS_2$. Of course, any other process changing the surface stoichiometry could lead to a change in the energy

[17] The "near-UV" is important because it differentiates this method from absorption or NEXAFS/EXAFS methods also commonly referred to as Constant Final State. Other than the difference in excitation energy, the electrons detected with near-UV CFS are primary photoelectrons whereas the absorption methods detect secondary electrons or processes.

difference between the CIS valence band edge and core level, making the determination of band offsets using the indirect method questionable.

Another difficulty arises with the formation of the junction itself. In the normal completed junction, consisting of the CIS absorber covered with ∼40 nm of CdS, the band offset is not measurable because of the thickness of the buffer layer. Thus a thinner (<5 nm) layer of CdS must be used in order to still obtain a signal from core levels of the CIS layer [12]. When measuring the valence band edge of the CIS substrate in the CIS-CdS junction with UPS, the CdS can have a maximum thickness of a few atomic layers at which point the CBD-CdS layer will most likely be made up of not-yet coalesced islands from ion-by-ion deposition, meaning that some of the signal will still come from the bare CIS absorber [86]. On the other hand, when using XPS the absorption cross sections of the CIS valence band are so small using Al Kα and Mg Kα that with any CdS coverage many scans (∼100 at 100 ms acquisition time) would be needed to determine the valence band edge. One is thus left with the indirect method. Using CFS (also referred to as "the direct method" of band offset measurements), however, with an excitation energy of 7.5-4.0 eV, one is on the extreme low energy side of the universal curve of electron mean free paths and below the excitation energy of plasmons. Here the information depth in CdS is higher than at He I excitation (21.2 eV), up to about 5 nm as estimated by CFS measurements (fig. 32). The absorption cross sections of the CIS valence band electrons at these energies are also large enough to allow the measurement of the valence band edge through at least 1.3 nm of CdS in a single sweep.

Furthermore, only one sample is needed for the entire measurement and no bare CIS absorber is required. This is of extreme convenience because oxygen in air can quickly change the properties of the absorber [110, 111]. The single sample used, CIS covered with CdS, need not be loaded immediately into the vacuum chamber due to CdS's stability in air, although the less air the sample sees the cleaner its surface will be.

For the indirect method five samples were used. Each had a $CuInS_2$ absorber from the same batch of the Helmholtz-Zentrum Berlin (HZB) baseline covered with increasingly thick layers of CdS ranging from the bare absorber to 30 nm CdS after 7:00 minutes deposition time. The other samples had deposition times of 40 seconds, 1:00 minute and 4:00 minutes corresponding to 1, 1.3 and 7 nm CdS layer thickness respectively, estimated from the integrated CIS core level peaks. For the CFS method, the same samples with 40 seconds, 1:00 minute and 4:00 minutes were investigated.

The CBD buffer layers were deposited at 60°C using standard solutions of Cd-acetate ($Cd(C_2H_3O_2)_2$), ammonia (NH_3) and thiourea (H_2NCSNH_2).

As previously mentioned, the details for the indirect band offset determination can be found elsewhere. The CFS method, while originally used to probe a-Si:H states [112], has more recently been applied to the investigation of the properties of a-Si/c-Si heterojunctions with ultrathin (≤10 nm) a-Si:H layers [46, 113, 114, 115], but not yet to the CIS-CdS heterojunction. In the CFS method, the excitation energy is scanned while the detector energy is kept just above the vacuum level, that is, the detected electron count rate, $n_{e^-}(n\nu)$, is made up of primary photoelectrons. If one knows the dependence of the

photon flux, $\Phi_{photon}(h\nu)$, on the excitation energy, a photoelectron yield,

$$Y = n_{e^-}(n\nu)/\Phi_{photon}(h\nu) \tag{24}$$

can be calculated. If the energy dependance of the matrix element for excitation of the electron from the valence band to the vacuum state is known, a density of states can be determined from a measured photoelectron yield [112]. This is because, unlike UPS, the valence band spectra measured with CFS are not convolved with the conduction band density of states due to the fixed final-state energy. But, because the energy dependence of this matrix element is not known for CIS, the density of states could not be determined. Solely the higher information depth offered by the low excitation energy was used because the immediate aim of the experiment was the determination of the band offsets. The determination of the density of states is, however, important because this information may help illuminate possibilities for changing the CIS-CdS band line-up.

Because the highest photon energy produced by the xenon high-pressure lamp used in the CFS experiment is about 7.5 eV, it is possible to probe both the a-Si and c-Si valence band edges in the a-Si/c-Si junction [116]. However, because the valence band edge of CdS lay at about 6.8 eV below the vacuum level in these samples, as determined using the secondary electron cut-off from the UPS measurements on CdS (sec. 3.2.4), it was not possible to measure the valence band edge of this layer with the CFS method: a clean signal is only available below about 6.5 eV excitation energy. Therefore, in a slight modification to the method already described, only the CIS absorber was measured with CFS while the CdS was measured with conventional UPS (He I) in the same chamber immediately following the CFS measurement. Thus, the high information depth of CFS was used to probe the underlying CIS layer while surface sensitive UPS was used for the exposed CdS. An excitation source able to produce higher energies will be able to measure both valence band edges directly using only CFS.

6.2 Linear Extrapolation

The method used to determine the valence band edges in this section is simply to extrapolate the linear portion of the band edge to the background signal, the point of intersection being the position of the band edge (see sec. 3.2.5). With the indirect method this is critical in order to maintain direct comparability with experiments found in literature. The results of the CFS measurements were not as straightforward. Because of the presumed high defect density at the CdS-CIS junction, it may be justified to treat this system similarly to the a-Si/c-Si junction and confirm the linear extrapolation through activation energy measurements to discern, if any, the difference between the valence band edge obtained from the linear extrapolation and the electron mobility edge [115, 116]. Nevertheless, a simple linear extrapolation is used in this section for the sake of continuity while section 6.3 explores the weak behavior of the CFS spectra using logarithmic plots.

The initial UPS and CFS measurements of the bare CIS absorber etched in KCN solution

for three minutes, fig. 30,[18] show a valence band edge between 0.65 eV±0.10 eV (UPS) and 0.70 eV±0.10 eV (CFS) below the Fermi Level. The discrepancy in the two measurements is well within the margin of error of the measurement and can also be caused by the different information depths of the two measurements as well as a slight difference in the determination of the Fermi Level. The Fermi Level position was repeatedly recalibrated throughout the experiments using Au foil cleaned via Ar^+ sputtering for the indirect method and freshly deposited evaporated polycrystalline Au films (∼100 nm) on Si for the direct method. In addition, valence band absorption cross sections at the low excitation energies used in CFS are higher than at the UPS excitation energy of 21.2 eV, which could possibly explain the increased band tail in the CFS measurement. In contrast, the almost linear behavior of the valence band edge and background measured with UPS has been observed in experiments on clean $CuInS_2$ many times using a laboratory UV source and at low energy (35 eV) synchrotron radiation and can be found in literature [117]. With increased exposure to air, it was observed that the band edge becomes more curved as the sample surface becomes contaminated (sec. 5.1.2.2); the little exponential behavior that is present is probably obscured by the noise in the measurement.

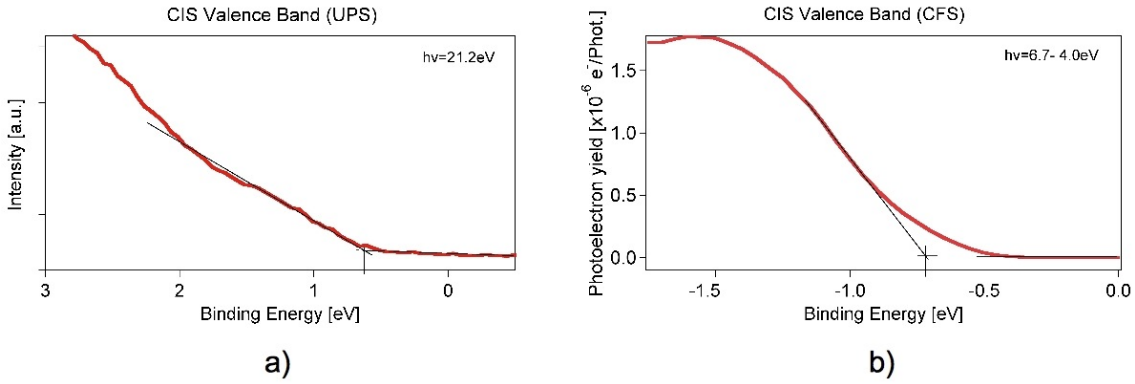


Figure 30: a) UPS and b) CFS measurements showing initial valence band edge positions of a CIS absorber etched in KCN for three minutes without CdS. The UPS measurement resulted in a valence band edge lying 0.65 eV±0.10 eV below the Fermi Level, while the CFS measurement resulted in 0.70 eV±0.10 eV.

With the indirect method, the shift in the valence band edge due to the deposition of CdS was found using the shift in the core levels measured before and after the application of the thin buffer layer. This exploits the assumption that the energy between the valence band edge and the core level is fixed, even after the CdS deposition. Thus, the CIS core levels were used to determine the change in the valence band edge from the initial position

[18]The difference in the intensity (y-) axes of the two graphs in this figure is due to the ability in the CFS measurements to record the photon flux *in-situ*. This results in an actual electron yield pro photon in CFS measurements so that intensities between measurements can be compared as follows later in the chapter. The flux of the He lamp used for UPS measurements, on the other hand, is dependent on several unknown factors, including local vacuum chamber pressure and He pressure in the the He lamp. Because the UPS intensities are susceptible to these random fluctuations, the intensities of the spectra are not comparable, leading to the intensity axis being marked in "arb. units." This commentary applies equally to fig. 32.

measured in fig. 30 a) to the position in the CIS-CdS junction, which leads to the band diagram illustrated in fig. 31 b). Similarly, the position of the CdS valence band edge in all samples with CdS was compared using Cd core levels where the observed change between these samples was less than 100 meV supporting the assertion in sec. 5.2 of no band bending in the CdS. Fig. 31 b) shows further the position of the CdS valence band edge measured on the 7:00 minute CdS layer, corrected using the small shift in the Cd core level between the 4:00 minute and 7:00 minute samples.[19] The difference between the core level-corrected CdS valence band edge of the sample with the 4:00 minute CdS layer at 2.40 eV±0.10 eV and that of CIS at 1.15 eV±0.10 eV delivers a valence band offset of 1.25 eV±0.20 eV.

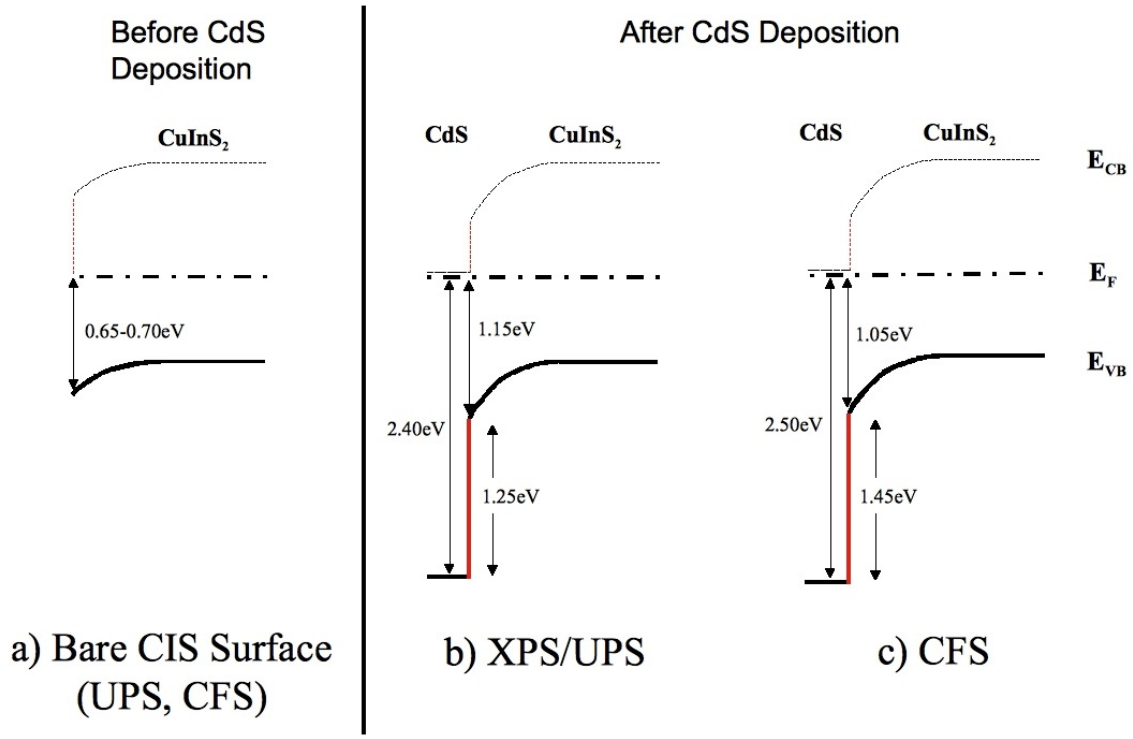


Figure 31: Schematic energy diagram showing a) the bare CIS surface and the CIS-CdS (4 min) junction with the band offsets at the interface as measured by b) the indirect method resulting in a band offset of 1.25 eV±0.20 eV and c) using CFS resulting in an offset of 1.45 eV±0.20 eV. The labeled valence band positions and offsets were measured with reference to the Fermi Level (dashed line) at the interface. The conduction band and the band bending are shown for completeness and were not measured here.

Instead of employing the CdS valence band edge of the 7:00 minute sample and the core level shifts to compute the position of the CIS valence band edge as done above, an alternative is to directly measure the CdS valence band edge on the 4:00 minute sample with UPS because it is also thick enough to be a closed layer and again calculate the position

[19]The sample used as the "junction" was indeed the sample with 4:00 minutes of CdS. However, in keeping with the literature, the valence band edge of the thickest layer was used and core level-corrected back to the sample used as the "junction."

of the CIS valence band edge through core level observation. This was done and resulted in a CdS valence band edge 1.30 eV below the CIS valence band edge, the deviation from the analysis above lying easily inside the error of the measurement. The observed changes in the CdS core levels are due to small chemical changes on the CdS surface and not due to band bending in the CdS buffer layer.

The initial measurement shown in fig. 30 b) was only used as a comparison between the UPS and CFS methods on CIS. The actual measurement of the band offset using CFS did not employ this sample (see introduction) in the linear extrapolation analysis. The UPS measurement on the 4:00 minute CdS layer is shown in fig 32 a), while the corresponding CFS measurement in the CIS valence band edge, taken just prior to the UPS measurement in the same chamber, can be seen in fig. 32 b). Although three samples were measured with CFS, with 1, 1.3 and 7 nm thick CdS layers, only the valence band edge of the sample with the thickest layer could be fitted with a linear extrapolation of the band edge. The other samples displayed no linear portion suitable for extrapolation and are thus not shown here (see discussion in sec. D). In spite of this, however, the attenuation of the CIS signal was used to analyze layer thickness. The attenuation corresponded to CdS film thickness ratios of $1 : 1.5 : 4$, for the 40 second, 1 minute and 4 minute films, respectively, further supporting the estimates made from the attenuation of the CIS core level signals.

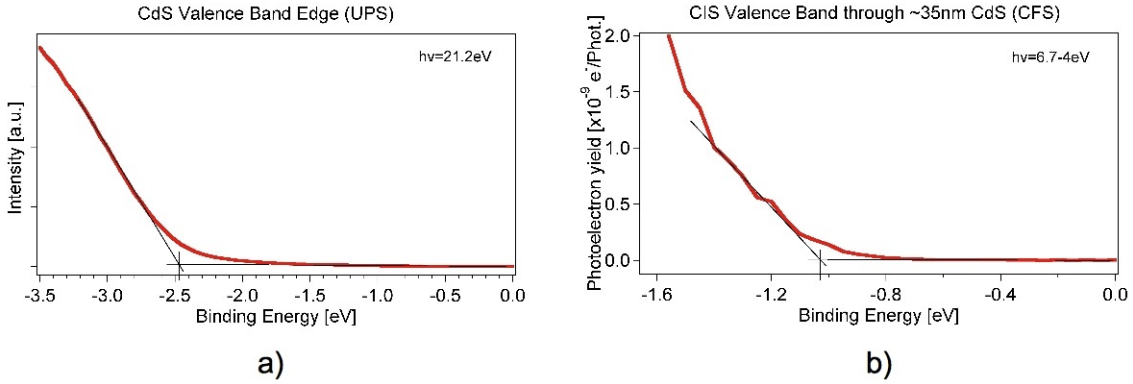


Figure 32: a) shows the UPS measurement of the 4:00 minute CdS layer complementary to the CFS measurement on CIS. b) shows the CFS measurement on the CIS-CdS junction which only probes the CIS valence band edge. This sample was taken to be the "junction" from which the band offsets were determined. The band offset is $E_{VB,CdS}$ (UPS)$-E_{VB,CIS}$ (CFS)$=1.45\,\text{eV}\pm0.20\,\text{eV}$.

Although the CIS valence band edge in fig. 32 b) is rather weak, the position of the edge is not chosen at random: the difference in intensity between the CIS edge extrapolated in Fig 30 b) and fig. 32 b) (about three orders of magnitude) can be reasonably expected from a signal attenuated through ~5-6 nm of CdS. The values appearing in fig. 31 c) are taken directly from the measurements in fig. 32 without corrections from core levels. The direct observation of the CIS valence band edge at $1.05\,\text{eV}\pm0.10\,\text{eV}$ and the CdS valence band edge at $2.50\,\text{eV}\pm0.10\,\text{eV}$ resulted in a valence band offset of $1.45\pm0.20\,\text{eV}$.

Changes on the CIS surface from the CdS deposition can be seen by examining the difference between the results shown in fig. 31 a) before the application of CdS and fig 31 b) and c) after CdS deposition. In this sample the Fermi Level is pushed an additional ∼400 meV toward the CIS conduction band edge during the deposition of the CdS, probably within the first few seconds in the chemical bath: before the deposition, the surface of the CIS absorber is slightly p-type while after the deposition the surface is solidly n-type.[20] This means the finished cell may contain an inverted absorber surface which is thought to be advantageous to heterojunction solar cells as long as the thickness of the inverted layer of the CIS is minimized. The photo-generated holes created in this inverted surface layer (where many of the photons in the blue range are absorbed) can diffuse to the pn-junction or to the interface where they will have a high probability of recombination due to the high defect density and high density of majority carriers (electrons). This results in a partial loss of charge carriers and a reduction in I_{sc} [1, 118].

6.3 Logarithmic Analysis

The weak behavior of the CFS measurement near the valence band edge on the sample with the 4:00 minute CdS layer was also investigated using a logarithmic plot in a manner similar to Sebastiani, et al.'s investigation of a-Si/c-Si [46].

Fig. 33 again shows the CFS spectrum found in fig. 32 b), this time plotted with a logarithmic intensity axis. The x-axis has been shifted by 2.50 eV, the energy difference between the CdS valence band edge and the Fermi Level measured by UPS, so that the valence band offset can be read directly from the position of the CIS valence band edge. The valence band edge of the CdS is thus at zero, and it can be seen that the highest excitation energy from the xenon high-pressure lamp was very close to being able to probe the CdS band edge, and that the CFS spectrum does indeed contain some contribution from the CdS, although a band edge could not be determined.

Several other curves are also present in the graph. The contribution from the CdS was fitted with the sum of a straight line (up to the valence band edge) and an exponential curve (after the band edge), shown here as the red dashed line. The dark dotted line is the contribution from the CIS, represented here by a down-scaled version of the bare CIS valence band edge measurement shown in Fig 30 b), the position of the valence band edge being the same in both plots (linear extrapolation). The scaling factor is $C_{CIS} = 8.0\text{x}10^{-4}$, and one can see by this fit that indeed the linear extrapolation shown in fig. 32 b) was done at a reasonable intensity. These two curves were then added to form the dark solid line $Y_{intern,fit} = C_{CdS} \cdot Y_{int,CdS,fit}(E) + C_{CIS} \cdot Y_{int,CIS}(E + \Delta E)$, to be compared with Y_{int}, the measured CFS spectrum, shown as the red solid line (marked with error bars). The scaling factors C_{CdS} and C_{CIS} are given at the bottom of fig. 33 and the relative difference between the fitted and the measured CFS spectra is plotted in the bar at the top of the figure.

[20] The band bending caused on the CIS surface by the CdS deposition was not reproducible when considering depositions from different chemical baths (see discussion, sec. 5.2).

The fit is very reasonable down to the position of the CIS valence band edge, but in order to subtract the effect of gap states stemming from the formation of the junction, the CIS valence band edge in the junction was determined by the linear extrapolation from fig. 30 b), shifted for band bending to fit into the shoulder clearly seen in the CFS spectrum, instead of using the linear fit from fig. 32 b). This resulted in a band offset of 1.40 eV±0.20 eV. The shift of the CFS spectrum to correct for band bending was $\Delta E =$ ∼450 meV, similar to that found using the core level shifts.

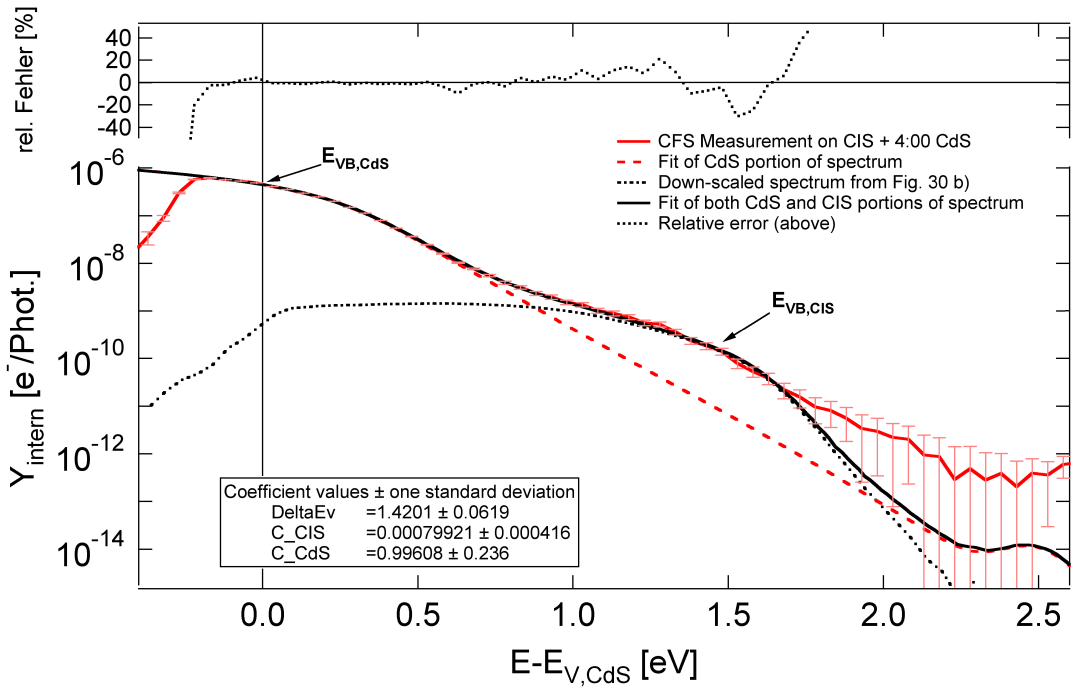


Figure 33: Logarithmic plot of the CIS sample with 4:00 minutes of CdS deposition. This is the same plot found in fig. 32 b). The band offset determined through the logarithmic investigation was 1.40 eV±0.20 eV. See explanation in text.

The linear extrapolation in section 6.3 thus overestimated the band offset by 0.05 eV possibly due to gap states now present on the CIS surface after the CdS deposition, or to CdS states still able to contribute a small signal at these energies. Although the difference in the values from the linear and logarithmic analyses of the band offset is small and well within the error of the measurement, the logarithmic investigation of the CFS spectrum does illustrate how weak behavior can influence band edge measurements.

The other two samples, with 40 seconds and 1:00 minute of CdS were also investigated in this way, with a resulting band offset of 1 eV, far smaller than any literature values and are discussed in Appendix D. We presume that, because of the lack of linear band edges in these measurements, as already discussed, there was some higher contribution from states near the CIS valence band edge which smeared out the linear portion, although it would be expected that with thicker layers, this smearing would become more pronounced, in contrast to what was observed. It is, however, also possible that the band offset changes

after the initial deposition period, and that what was measured after 40 seconds and 1:00 minute of deposition time was CdS with a stoichiometry (and thus density of states) changing with depth seen more clearly with CFS due to the larger information depth and not seen with UPS. A deposited layer several nm thick with CdS of a certain stoichiometry on the surface would appear to only have this stoichiometry in a UPS spectrum, whereas a CFS measurement may detect the slight changes with depth. These changes may become less apparent as the film continues to grow homogeneously after the initial stages.

Nevertheless, the scaling factors used to down-size the CFS CIS spectrum in fig. 30 b) for the fits of the three CFS spectra on CIS with CdS were used again to determine a ratio of the CdS layer thicknesses of $1 : 2 : 6$, supporting the estimates made from the attenuation of the core levels.

6.4 Preliminary Cu(In,Ga)S_2-CdS and $CuGaS_2$-CdS Band Offset Investigation

Timely and well defined measurements on the band offsets of these two junctions were hindered by the poor reproducibility of the CIGS and CGS absorbers due to the not yet fully mature production processes available at the time this thesis was completed. Samples in a single batch were known, at times, to have differing characteristics. The differences between samples from separate batches were even more pronounced. Also, adhesion problems were rampant in the very early stages of the Cu(In,Ga)S_2 production.

Because the XPS/UPS experiments employ, in general, several samples, it was decided to exclude these measurements at first in favor of more defined experiments on the $CuInS_2$-CdS system. Several preliminary experiments were, however, done on junctions with CdS and Ga containing absorbers.

These first XPS/UPS experiments with the Cu(In,Ga)S_2-CdS and $CuGaS_2$-CdS systems show similar valence band offsets to the $CuInS_2$-CdS system. This seems likely, because the upper valence bands off all three chalcopyrites have the same composition, the only difference being the type III element whose contribution to the valence band are the Ga 3d and/or In 4d quasi-core levels found well away from the valence band edge. Thus the S 3p states making up the CdS valence band edge will interact in a similar way with the S 3p electrons and the Cu 3d electrons of the CIGS valence band independent of Ga content.

Initial measurements of the Cu(In,Ga)S_2-CdS valence band offset resulted in $\Delta_{VB} = 1.30\,\text{eV} \pm 0.20\,\text{eV}$ while the initial result for the $CuGaS_2$-CdS system was $1.20\,\text{eV} \pm 0.20\,\text{eV}$.

Thus, within the margin of error, the band valence band offsets between CdS and the three absorbers $CuInS_2$, Cu(In,Ga)S_2 $CuGaS_2$ were the same.

6.5 Conclusions about the Measured Valence Band Offsets

Using the indirect method of measuring band offsets as a reference, it was shown that near-UV constant final state yield spectroscopy (CFS) is a suitable method for valence band edge and valence band offset experiments involving chalcopyrite thin films. The indirect method resulted in a measured valence band offset of Δ_{VB} =1.25 eV±0.20 eV while CFS showed a band offset of Δ_{VB} =1.45 eV±0.20 eV, both of which are in agreement with literature values [57, 101]. While another source, [100], is also in agreement with the XPS/UPS result presented here, the CFS result is noticeably different, possibly due to chemical shifts in the CIS from the CdS CBD. A band offset of Δ_{VB} =1.40 eV±0.20 eV was determined from a logarithmic investigation of the CFS measurements. Also, the absolute positions of the valence band edges themselves were similar in both experiments. This supports again the findings in [97], that the position of the valence band of a I-III-IV_2 chalcopyrite will be much more affected by the Cu 3d-S 3p repulsion than the CdS.

An estimation of the conduction band offsets using the bulk values of the band gaps (CIS, 1.5 eV [119]; CdS, 2.4 eV [120]) results in a Δ_{CB} =0.35 eV for the indirect method and Δ_{CB} =0.55 eV for the CFS method. The CFS values are higher than the literature values discussed earlier (200-400 meV) [57, 81, 100, 101]. In [66], it is suggested through activation energy measurements, that the effective band gap is around 1.3 eV, corresponding to a cliff of about 0.2 eV

Although the maximum excitation energy of 7.50 eV barred the possibility of measuring the CdS valence band edge with CFS, the high mean free path of low-kinetic energy electrons made it possible to measure the valence band offset of the CIS-CdS junction using only one sample. Also, because both edges were measured directly, CIS with CFS and CdS with UPS, any chemical changes taking place on the CIS surface during CdS deposition can be accounted for. Both of these factors represent an improvement over the indirect method. At a later time, after an excitation source able to produce higher photon energies is available, the CdS valence band edge will also be measurable with CFS.

Ga was also introduced into the system in this chapter. Preliminary valence band offset measurements of the Cu(In,Ga)S_2/CdS and $CuGaS_2$/CdS junctions resulted in values of Δ_{VB} =1.30 eV±0.20 eV and Δ_{VB} =1.20 eV±0.20 eV, respectively. Ga concentration, therefore, has no effect on the valence band offset of the general Cu(In,Ga)S_2/CdS system within experimental error.

In the next chapter the effect of Ga on the conduction bands of $CuInS_2$, Cu(In,Ga)S_2 and $CuGaS_2$ is investigated with two methods and the results are compared to each other and to bulk values. The effect of the Ga on the conduction band line-up with CdS is also discussed along with the consequences for the solar cell.

7 The Cu(In,Ga)S_2 Conduction Band

7.1 The Accessibility of the Conduction Band to Measurements

The semiconductor conduction band plays an important role for charge carrier transport in solar cells with a p-type absorber and n-type window as investigated here. The minority carriers, responsible for solar cell characteristics, are electrons in this type of cell at the point where electron-hole pairs are created and separated and are transported in the conduction band. For this reason, the band line-up at each junction between the different materials of the cell should not hem the flow of electrons through potential barriers, while at the same time causing no reduction in the effective band gap of the device and the p-n junction should not coincide with the metallurgical junction, as discussed in sec. 4.4. This is most easily done through a flat conduction band edge through the junction although a small spike less than ∼300-400 meV, surmountable by the electrons through thermionic emission alone, can improve junction characteristics [1, 57, 80].

The main difficulty in studying the conduction band of a material with photoelectron spectroscopy is that the states of the conduction band are not occupied, and thus, no electrons can be excited out of them as is the case with PES and the occupied lower states. When studying bulk effects in a semiconductor, optical methods can be used to directly acquire the bulk band gap. If the position of the bulk valence band edge is known these two values can simply be added to attain the position of the conduction band edge. However, for the investigation here, the surface characteristics of the Cu(In,Ga)S_2 are of interest because these are the decisive values affecting junction properties. In order to study these properties with surface sensitive methods employing electrons one is then left with the strategy of filling these unoccupied states and observing how the system reacts. One difficulty is that the system may no longer be in the ground state during measurements for reasons which will be discussed further below. This can make comparison with UPS spectra to determine the surface band gap difficult. In spite of this, investigations of the conduction band can still give information about the system if one is careful with the interpretation of the results.

Two methods were used here to investigate the conduction bands of CIS, CIGS and CGS and the effect of Ga concentration: Near Edge X-Ray Absorption Fine Structure (NEXAFS), a special form of X-Ray Absorption Spectroscopy (XAS), and Inverse Photoelectron Spectroscopy (IPES). In the former, a core hole is present in the system leading to possible distortion of the energy bands described by the *final state rule* in sec. 3.4, whereas in the latter, an additional particle, an electron, enters the system leading to possible charging effects (sec. 7.5) if the incoming electron flux is too high. Because of the low probability of the electrons coupling into the empty conduction band states, high currents used to increase signal intensity may cause the charging effects which can shift the position of the measured band edges.

In this section, the discussion of the conduction band of Cu(In,Ga)S_2 and the conduction band offset with CdS will remain a relative one, because, as will be seen, the setting of an absolute zero of energy remains elusive. Nevertheless, important information about the nature of the CIGS conduction band can be gleaned from the investigation which can

help to understand the function of the junction in the solar cell. Apart from being an interesting material system, the main impetus for these investigations as pertains to the solar cell is to learn more about the evolution of the Cu(In,Ga)S_2 band gap with the addition of Ga and to try to identify why the open circuit voltage, V_{oc}, of CIGS-based solar cells is ∼100 mV higher than that of its CIS counterpart. Although it has been concluded from the afore mentioned optical methods, more specifically quantum efficiency [66] and UV-VIS absorption [67] measurements, that the band gap of Cu(In,Ga)S_2 increases with Ga content, there is no information contained in these measurements about which band edge moves in order to accommodate this change. And this change, of course, however it may come about, may have profound effects on the band line up at the Cu(In,Ga)S_2-CdS interface.

Previous investigations of the Cu(In,Ga)Se_2/CdS junction have shown most of the opening of the band gap of Cu(In,Ga)Se_2 with increased Ga content takes place in the conduction band [121]. Correspondingly, the largest changes in band offset are also between the conduction bands of Cu(In,Ga)Se_2 and CdS as opposed to the valence bands. It remains to be seen if the Cu(In,Ga)S_2/CdS system reacts in a similar way to increased Ga concentration.

7.2 NEXAFS

In XAS, an electron can be excited into an unoccupied level without leaving the solid if $h\nu \geq \Delta E$, where ΔE is the energy difference between the initial and final states. The energy at which this transition occurs determines the energetic position of the absorption edge of a specific electron shell. Although information is contained in the entire absorption spectrum, sometimes extending hundreds of eV past the absorption edge as discussed in sec. 3.4, the focus here is on the edge itself and the region immediately following called NEXAFS.

In NEXAFS, electrons from a specific core level of an atom in the sample are excited into the unoccupied states of the conduction band by continuously increasing the excitation energy until ΔE is reached. The further increase in incident energy can then be chosen to measure the selected post-edge region. The selection of a specific energy range leads to the excitation of a specific part of an orbital, or edge, in the selected element of the sample. The remaining core hole causes several different phenomena to occur, each of which can be used to determine at which excitation energy the electron was excited into the lowest, allowed, unoccupied state (fig. 5) and correspond to different information depths in the sample. Unless otherwise noted, sample current is used here to detect the excitation energy at which the absorption begins because of its rather surface sensitive nature. Although it would be theoretically more surface sensitive to use the electron analyzer to detect electrons with the kinetic energy of the Auger electron corresponding to the transition being investigated, this method was attempted and produced unusable spectra of very poor quality.

In the following sections a linear background determined through the extrapolation of the linear portion of the spectrum before the edge was subtracted from all NEXAFS spectra. In addition an energy calibration was carried out to ensure at least a relative energy scale

between all spectra of one edge, as discussed in the following section.

7.2.1 Mirror Current

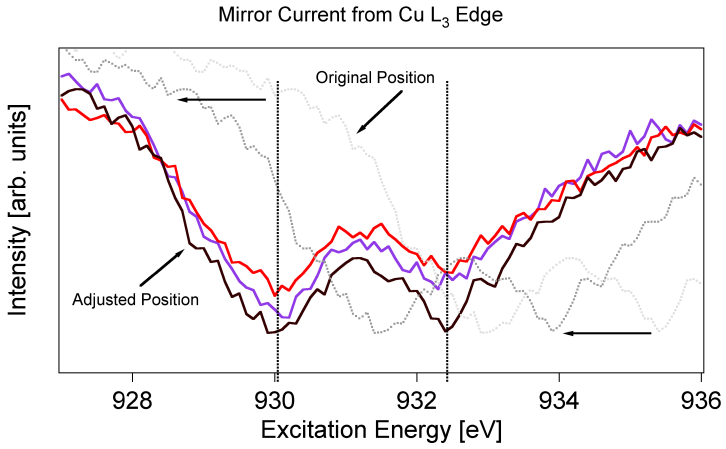


Figure 34: The process of adjusting NEXAFS spectra using the mirror current in order to ensure at least all measurements of a single absorption edge enjoy a common, relative energy scale. The shift is enlarged here for clarity, although shifts of up to 1.30 eV were routinely seen.

Before starting the discussion of the NEXAFS measurements, the issue of the reproducibility of the excitation energy needs to be resolved. The monochromator is run by a step motor with the resulting excitation energies being calculated from the motor position. Slipping of the motor, for example, especially when the monochromator is driven far from a certain energy region between measurements, can cause different scans to be slightly shifted in energy. Because part of the analysis of the absorption spectra entails the investigation of shifts in the absorption edges, the possibility that the shift is due to a non-reproducible monochromator scan must be ruled out.

Fortunately, the mirror current, I_0, recorded parallel to each absorption edge contains energy dependent features which allow for the determination of a relative energy scale. A shift of the mirror current spectra and a matching shift of the corresponding absorption spectra, as shown in fig. 34 ensure at least a common, relative energy scale for all spectra of a specific edge [122]. The dips in this figure were fitted allowing the determination of the energy scale to an accuracy of ± 100 meV for the Cu L_3 spectra. As will be discussed below, the S L_3 spectra[21] had, for example, a much larger error. The immediate purpose here is, however, to illustrate how the relative calibration of the absorption edges was performed.

An absolute scale could be defined if the material on the mirror causing these small absorption features could be identified. This is routinely done with higher energy edges where a material reference, whose absorption edge energy is known, is measured parallel to the sample.

7.2.2 Complementary Valence Band Meausrements

Before presenting the results of the conduction band measurements, it is reminded that not only the position of the conduction band is of interest, but also whether the valence

[21] The S spectra actually show the edges of S $L_{2,3}$ corresponding to the S $2p_{1/2}$ and S $2p_{3/2}$ core levels, respectively. However, because the two edges are only 1.2 eV apart only the first edge, S L_3, can be distinguished. For the sake of simplicity this spectrum will be referred to as S L_3.

band shifts with incorporation of Ga into the $Cu(In,Ga)S_2$ lattice. For this purpose, valence band measurements were made at BESSY with 35 eV excitation energy on CIS, CIGS and CGS samples in addition to the NEXAFS measurements. The results of these measurements are shown in fig. 35 and illustrate several characteristics of the evolution of $Cu(In,Ga)S_2$ with increasing Ga content.

In a way, these measurements supplement chapter 6, but find their own place here by completing the picture of E_g for the $Cu(In,Ga)S_2$ system. The structure of the upper valence band edges can clearly be seen, along with the p-d repulsion, also discussed in chapter 6. While no change is seen between the position of the valence band edge of CIS and CIGS [123], meaning that the opening of the band gap must be due to the conduction band alone, the valence band edge of CGS is moved closer to the Fermi-Level by 300 meV due to the increased prominence of the Cu 3d states at 3 eV. Not only does this support the XPS findings of a Cu-richer CGS surface ([Cu]/[In]=0.25 for CIS and [Cu]/[Ga]=1.20 for CGS), but the increased amount of Cu increases the repulsion between the Cu 3d states and the S 3p states, thereby pushing the Cu 3d states toward the Fermi Level [94, 97]. Thus, in the case of the CGS, using the bulk band gap value of 2.40 eV as a starting point, it can be concluded that here the opening of the band gap includes a shift of both bands where the conduction band must compensate for the effective closing of the band gap from the valence band.

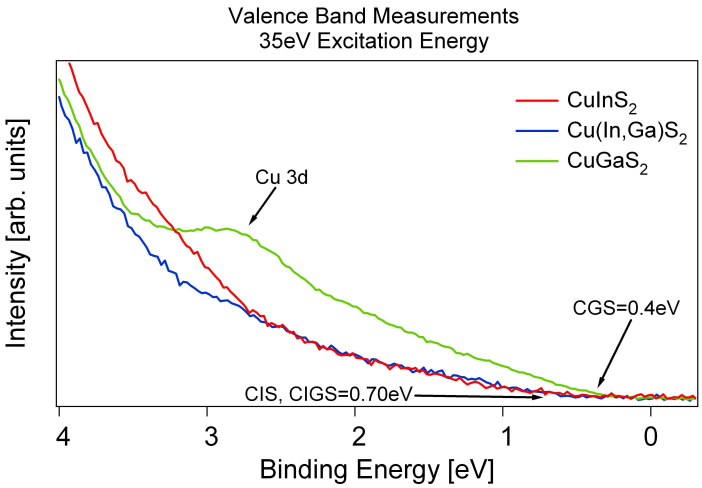


Figure 35: Valence band edges of $CuInS_2$, $Cu(In,Ga)S_2$ and $CuGaS_2$ measured with an excitation energy of 35 eV at BESSY. The edges of CIS and CIGS are at the same position showing that the opening of the band gap between these two materials is due to the conduction band alone. The CIGS edge is shifted toward the Fermi Level.

It must be emphasized once more here that the values given are for the surface of the sample and may be preparation dependent. Furthermore, the results for the surface cannot necessarily be carried over to bulk properties. It is, however, the surface properties that are interesting in this case because the surfaces are directly involved in the junction.

Although the measured positions of the valence band edges of CIS and CIGS were shown to be the same, it is probable that the positions differ by an amount much smaller than the ±100 meV error attached to these measurements. The measured Ga concentrations on the surface of the CIGS of about 8% supports the existence of a very small shift and would keep with the trend that increased Ga concentration continually shifts the valence band edge toward the Fermi energy similar to what is found with a continuous opening of the band gap.

Moving on, now, with the bulk band gap values for CIS (1.50 eV), CIGS (1.60 eV) and CGS (2.40 eV), these initial valence band edge measurements can be used to make an estimate of approximately where the conduction band edges will be. For CIS one would expect the conduction band to be at about $E_c - E_f$=0.80 eV, while for CIGS and CGS this value will be 0.90 eV and 2.00 eV, respectively. These are, again, bulk band gap values and, therefore, an opening of the band gap toward the sample surface, proposed by several authors [107, 126], could change these energies. In the case of CIS and CIGS it is thought that both absorbers have some degree of Cu depletion toward the surface, and a general trend of an opening of the band gaps toward the surface is expected, although the absolute change between $E_{g,bulk}$ and $E_{g,surface}$ off the samples need not be the same.

It must be noted here that UPS is a band bending-dependent method and the measurements in fig. 35 may have the observed values due to coincidental circumstances. However, care was taken to etch and mount all three samples at the same time under the same conditions in order to minimize discrepancies in the band bending on the surface of each sample. And the values here correspond to the values most often seen over many measurements done on similar samples. Therefore, if there were a real difference between the position of the valence band edge of CIS and CIGS which is sometimes obscured by discrepancies in sample preparation, a general trend of differing values would be expected but was not observed.

7.3 NEXAFS Measurements

The initial allure of the NEXAFS measurements is, neglecting the core-hole problem, to determine the energy of the conduction band edge through the equation

$$E_{Edge} - E_B = E_c - E_f \tag{25}$$

where E_{Edge} is the energy of the absorption edge, E_B the binding energy, E_c the position of the conduction band edge and E_f the Fermi Level.

The reality, however, is that NEXAFS measurements contain only information about the partial density of states seen by the excited atom. The excitation energy of the measured edge corresponds to the energy difference between the selected core level and the first allowed, empty state in the conduction band. It cannot be known *a priori* whether the first allowed state is at the bottom of the conduction band.

Furthermore, when attempting to define an absolute energy scale, the core hole problem comes into play twice. Once in the material under study and second in the metal used to define a "Fermi Level." This will be discussed to a further extent below.

Therefore, in order to respect these difficulties, yet still interpret the NEXAFS spectra in a meaningful way, the Cu L_3 (Cu $2p_{3/2}$), In $M_{4,5}$ (In $3d_{3/2}$ and In $3d_{5/2}$), Ga L_3 (Ga $2p_{3/2}$) and S L_3 (S $2p_{3/2}$) absorption edges will be shown in the following sections and several different methods of analysis will be presented and discussed.

In the following spectra, the energetic positions of the absorption edges are taken to be the position of the edge half way between the background and the initial peak following the edge. In the literature, several other methods are found, such as using the position of the inflection point of the edge, or an extrapolation of the edge to zero. The reason for the choice here was to attempt to analyze only the relative positions of the peaks and because it does not introduce any new error beyond that coming from the mirror current calibration. However, it is fair to discuss further how the precise position of the edge should be defined. It will be seen later that the quantitative analysis only appears toward the end of the section on NEXAFS and that the preceding qualitative analysis discusses the difficulties arising not only from the experimental method of X-ray absorption, but also from the specific problems posed by the Cu(In,Ga)S_2 samples when analyzing the absorption spectra.

7.3.1 Raw NEXAFS Data

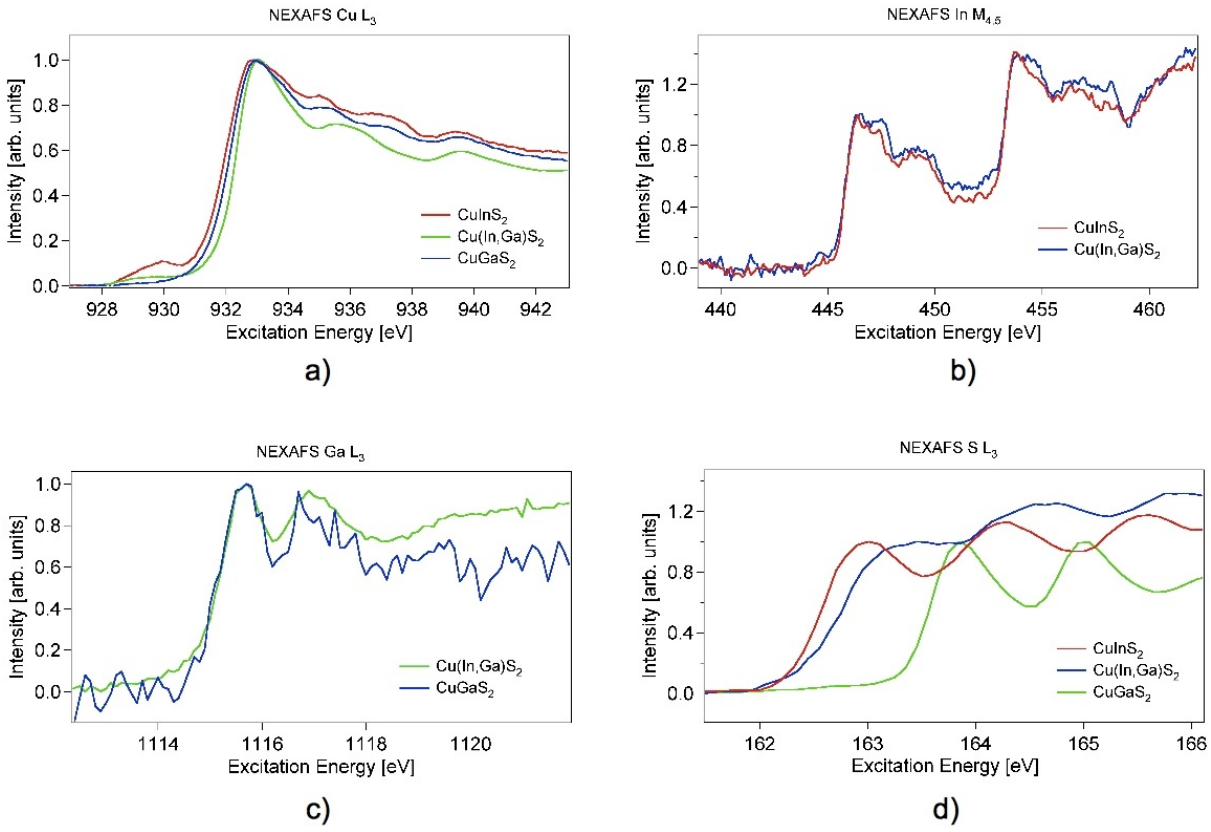


Figure 36: Absorption edges of a) Cu L_3, b) In $M_{4,5}$, c) Ga L_3 and d) S L_3 from $CuInS_2$, Cu(In,Ga)S_2 and $CuGaS_2$. The individual energy scales are not absolute, but instead relative, making shifts in the spectra correspond to real energy differences between the core level and first allowed, unoccupied state in the conduction bands of the three materials.

The L_3 absorption edges of Cu, S and Ga and the $M_{4,5}$ absorption edge of In are presented in fig. 36. All energy axes are calibrated relatively, as discussed above, so that energy

differences in the absorption edges are real differences in ΔE of each material. ΔE is, again, the energy difference between the core level and the first allowed, empty state in the conduction band in the excited state of the material.

Interesting is that the spectra from the In $M_{4,5}$ edge in b) and the Ga L_3 edge in c) display no shift. This means between the different materials, either the corresponding core levels and the first allowed empty state shift exactly parallel, or, as seems more plausible, there is no shift in the detected states with the addition of Ga.

The remaining spectra of Cu L_3 in a) and S L_3 in d) show clear shifts, the meaning of which can only be correctly interpreted after the subtraction of the corresponding core level binding energy. The shift in the absorption edge contains no information about which level, the core level or the conduction band state, was effected by the increase in Ga concentration.

It can, however, already be seen from fig. 36 that the incorporation of Ga does affect a change in the electronic levels of Cu(In,Ga)S_2 of some kind. This we will now investigate in more detail.

The pre-edge features in the CIS and CGS Cu L_3 spectra at 930 eV are due to CuO or CuS on the sample surface. A phase containing Cu with a partially unfilled 3d band will bring about such a feature because the oscillator strength between the Cu 2p and Cu 3d band is very high. Even a small amount of this phase in or on the surface of the sample will contribute noticeably to the spectrum [18, 21].

7.3.2 Material Specific Analysis

Before investigating the spectra of the individual elements with respect to each other under consideration of the binding energies, we want to consider the conventional method of moving forward with NEXAFS spectra.

Because a NEXAFS spectrum contains information about the partial density of states seen by the excited atom, a full series of spectra from all atoms will give information about all states in the conduction band, including the nature of their orbital momentum which will be hybridized in the conduction band as investigated for the Cu(In,Ga)Se_2 system by [21]. Here it was shown that the bottom of the conduction band of $CuInSe_2$ is comprised chiefly of In s-states with a significant admixture of Se p-type states and finally Cu p-type states $>$ 3eV above the conduction band edge.

Because of the identical valence structure of Se and S, it is assumed here that the lower conduction band of $CuInS_2$ has the same structure, with the obvious substitution of S for Se and under consideration of the fact that Se has an extra electron shell but the same valence structure. This can also be found in literature [125].

With this information about the conduction band, it was hoped to plot the three or four different spectra for each substance together in a single plot and subtract the correspond-

ing binding energies. The result would be a graph of the different partial densities of states of the three materials plotted versus binding energy, which would, when viewed together, show the structure of the Cu(In,Ga)S_2 conduction band and how it evolves with the addition of Ga. The resulting attempt for CIS is seen in fig. 37 a).

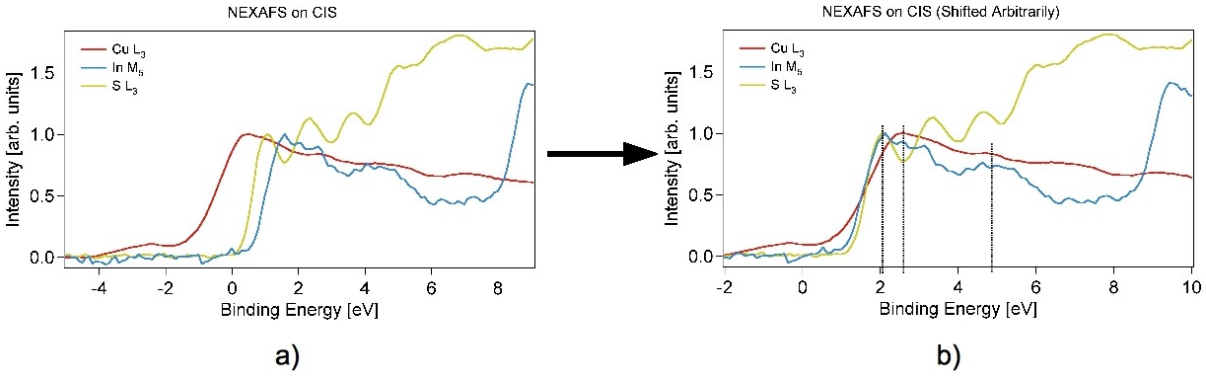


Figure 37: Absorption spectra from the three elements in $CuInS_2$ displayed a) after the subtraction of the corresponding core level binding energies. b) shows an idealized picture of the expected result. Reasons for the discrepancy are given in the text.

Fig. 37 b) shows a shifted version of a) which displays how the result of such an analysis is expected to look. In this idealized version of the conduction band none of the edges extend past the the Fermi Level (0 eV), as the spectra represent states in the conduction band. Furthermore, there are features common to different spectra (marked by the dotted lines in the figure). These correspond to regions of high densities of states in the conduction band into which electrons from different atoms can be excited. For example, the first peak of In and S fall together, meaning that electrons of d-type (from In) and p-type (from S) can both be excited into the bottom of the conduction band. The 2p electrons from Cu are excited first into a level lying slightly higher along with In. Cu and In then share another level around 5 eV.

The value of this plot, if it had been successful for all three materials CIS, CIGS and CGS, is that one would have been able to follow the evolution of the states common to different partial densities of states and would have also seen that new states would emerge as Ga was incorporated into the lattice. Presumably some of the states, most certainly those on the conduction band edge (In s-states), would have moved away from the Fermi Level, indicating and opening of E_g. The value of the information contained in [21] is that one already has some knowledge of which states are to be expected at which energetic positions.

There are two reasons why fig. 37 a) did not result in a plot resembling fig. 37 b). First, the measurements of the absorption edges and those of the core level binding energies have different information depths. The core levels were measured with conventional XPS meaning that the information depths were at most 3 nm, whereas the absorption spectra, being measured with total electron yield, can also count electrons which have been elastically scattered, thereby increasing the depth of the sample out of which the electrons can originate. The highest information depth of total yield was estimated to be between

15-20 nm for the Cu L_3 edge. Because of the known gradients in the samples toward the surface, it is plausible that the binding energies at the surface and at a depth of 20 nm are different. This is underscored by fig. 27 where a difference in the absorption edge can be seen between total electron yield and fluorescence signals, indicating a difference in the electronic configuration of the states between the bulk and the surface. This phenomenon will be referred to hereafter as "surface effects," and could include intrinsic band bending toward the sample surface.

Because band bending would shift all core levels parallel, it could not be responsible for the large shift between absorption edges in fig. 37 a), but it could be responsible for an equal shift of all edges by several tenths of an eV, resulting in, for example, some edges lying below the Fermi Level which was solely determined through the subtraction of the core level binding energies.

The estimated magnitude of the surface effect was a maximum of 500 meV, although values could change from sample to sample. The second and more vital reason for the discrepancy between fig. 37 a) and b) could, however, effect the edge position by more than 1 eV. This source of error concerns the mirror current calibration discussed in sec. 7.2.1. As mentioned already, this calibration ensured that all edges common to a specific element had a common energy scale which was not necessarily absolute. Thus, when combining absorption edges with very different energies and individual energy calibrations, none of which are absolute, the resulting graph contains essentially no information about relative edge position.

Because the groups of edges from each element share a relative energy scale, the physical information contained in the element specific analysis of the absorption edges can be more fully interpreted.

7.3.3 Element Specific Analysis

Although in this section the problems arising from surface effects are still present, we hope to limit their influence, along with the effect of the previously mentioned band distortion, through a few simple, yet well grounded assumptions, especially in the case of the Cu L_3 absorption measurements.

7.3.3.1 Cu L_3 Absorption Edges According to [21], the Cu L_3 measurements probe antibonding states formed from hybridized Cu 3d-4s states which are further hybridized with In-S orbitals, found at the absorption edge, and Cu 4s states at lower binding energies which make the main contribution to the absorption intensity. The absorption edges will be evaluated here after the subtraction of the Cu $2p_{3/2}$ core level binding energies under two different assumptions. The fact that the edges appear below the Fermi Level is for the moment of no consequence as the energy scale is, as already mentioned, still only relative.

Fig. 38 shows the Cu L_3 absorption edges after the subtraction of the Cu $2p_{3/2}$ core level binding energies actually measured on the samples during the NEXAFS measurements. These values were $E_{b,Cu2p_{3/2}} = 932.4\,\text{eV}$, 932.0 eV and 931.8 eV for CIS, CIGS and CGS, respectively. The subtraction of these values, as can be seen in fig. 38, leads to an increase in the shift between all of the absorption edges when compared to fig. 36 a). This is most noticeabe between CIS and CIGS, although the order of the position of the edges remains intact. The position of the absorption edge for CGS compared to that of CIGS is noticeably less than the expected 1 eV discussed at the beginning of the chapter.

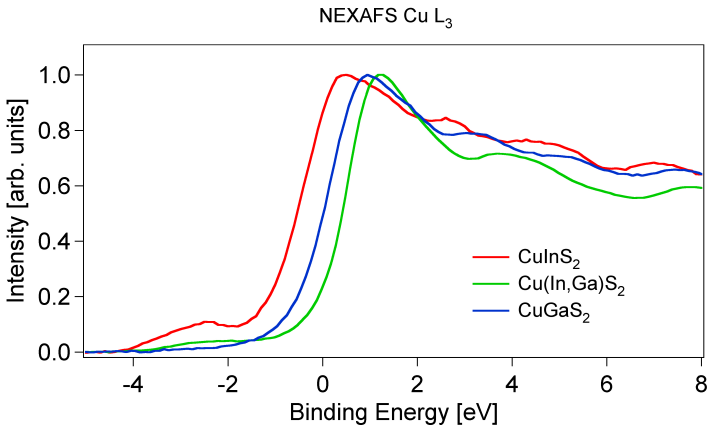


Figure 38: Cu L_3 absorption edges of $CuInS_2$, $Cu(In,Ga)S_2$ and $CuGaS_2$ after the measured Cu $2p_{3/2}$ core level binding energies have been subtracted.

However, because of the difficulties posed by the surface effects, the subtraction of these values is not concrete enough, as the values may easily change from sample to sample.

It was, therefore, decided to look at the Cu $2p_{3/2}$ core level binding energies measured on many samples, along with literature values for CIS, CIGS and CGS and to use binding energies that were most representative of the three samples over longer observation. Not only does this correct for some of the non-reproducibility of the samples, but when one considers that the Cu L_3 NEXAFS measurements done on many different sets of samples all led consistently to the same result presented in fig. 36 a) it would not be reasonable to apply data specific to one set of samples to the analysis of this reproducible measurement.

From the measurements of the Cu $2p_{3/2}$ core level binding energy done for this thesis, combined with similar details from literature [123], the value of E_b was set at 932.0 eV for both CIS and CIGS, whereas E_b for CGS, lying consistently under those of CIS and CGS, was set at 931.8 eV.

The subtraction of these binding energies leads to fig. 39. Because there was no difference in the binding energies of CIS and CIGS, the shift between their absorption edges remains the same as in fig. 36. In the case of the CGS, due to the slightly smaller binding energy, the shift between CIGS and CGS has been slightly enlarged compared to the fig. 36. However, as with fig. 38, the shift between CIGS and CGS still falls well short of the 1 eV expected from the bulk band gap estimates.

The shift between CIS and CIGS is 150 meV while the shift between CIGS and CGS is 400 meV.

If one attempts to define an absolute energy scale for these spectra, the most obvious method would be to measure a metal reference to define a Fermi Level because the first

unoccupied state of a metal corresponds to E_f. This was done with Cu metal sputtered for 45 minutes to ensure a clean surface. This measurement resulted in fig. 40 after the subtraction of the measured binding energy of the Cu $2p_{3/2}$ core level from the metal spectrum. This measured value was $E_{b,Cu}$=932.4 eV and is taken to be correct because there is no band bending in metals and the surface was cleaned. This value also coincides with literature values although these values display a large spread [124]

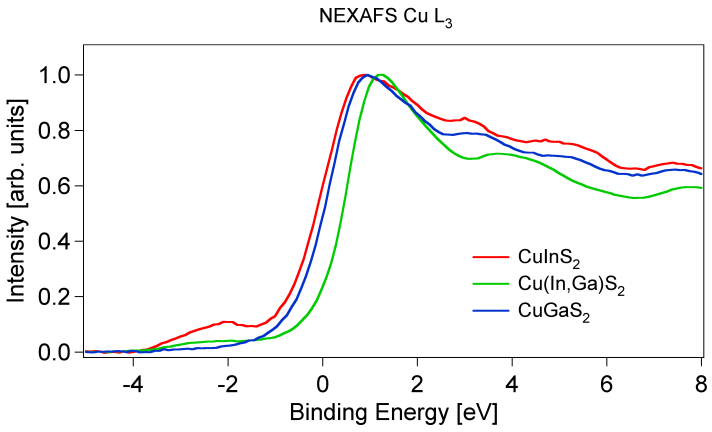


Figure 39: Cu L_3 absorption edges of $CuInS_2$, $Cu(In,Ga)S_2$ and $CuGaS_2$ after Cu $2p_{3/2}$ core level binding energies have been subtracted which attempt to correct for surface effects which cause differences in E_b measured with XPS and those excited during NEXAFS measurements.

Making the initial assumption that the half-maximum of the Cu metal spectrum corresponds to the Fermi Level, as indicated in fig. 40, values corresponding to $E_c - E_f$ can be read off for the three materials. These values are 1.75 eV, 1.90 eV and 2.30 eV for CIS, CIGS and CGS, respectively. When added to the values for $E_f - E_v$ determined from fig. 35, the results are surface band gap values of 2.45 eV, 2.60 eV and 2.70 eV, again for CIS, CIGS and CGS, respectively.

The difficulty of incorporating the Cu metal spectrum in the measurements in this way must, however, also be discussed. Because elemental Cu has 3s states as its first unoccupied levels, the electrons from the Cu 2p cores levels will indeed be excited into the states at the Fermi Level. However, as is the case with CIS, CIGS and CGS, expressed by the *final state rule* (sec. 3.4), there may be some band distortion in the Cu metal measurement different than that in the other three materials. Thus, when comparing the CIS, CIGS and CGS spectra with the Cu metal spectrum, two possible band distortions come into play. The inclusion of the Cu metal reference spectrum as an indication of a real Fermi Level, can, therefore, not be supported on physical grounds.

For this reason, the quantitative results of the the Cu L_3 spectra must be limited to the relative shifts between the spectra themselves. This, however, does not free us from possibly different band distortions in CIS, CIGS and CGS described by the *final state rule*.

If the assumption is made, however, that the $CuInS_2$ and $Cu(In,Ga)S_2$ experience similar band distortions due to the similarity of their lattice structures, the shift between the two spectra is real. This assumption is supported by the only small amount of Ga ($\sim$8%) which was measured on the CIGS surface and the structure of the Cu L_3 spectra following the absorption edge. These structures show the conduction band of both materials to be very similar.

This assumption cannot, however, be carried further to the CGS. Not only is the lattice well known to be different from CIS, but the structure of the conduction band after the absorption edge (>1 eV in fig. 39) can be seen to be different from that of CIS or CIGS. Furthermore, the relatively small shift between CIGS and CGS in fig. 40 suggests that the band distortion in CGS is more pronounced than in CIS and CIGS.

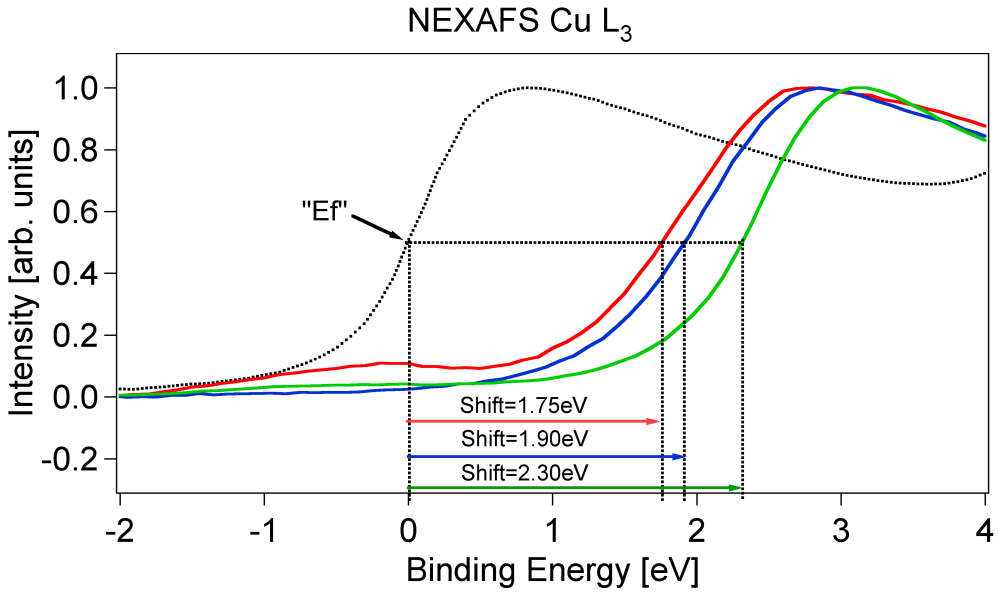


Figure 40: Cu L_3 absorption edges from $CuInS_2$ (red), $Cu(In,Ga)S_2$ (blue), $CuGaS_2$ (red) and Cu metal (black). The metal spectrum represents the Fermi Level in order to quantify the Cu L_3 spectra. See text for further details.

In order to explore the magnitude of the error attached to the NEXAFS measurements, it is useful to consider first fig. 41 which shows multiple Cu L_3 spectra for each material zoomed in at the half-maximum before the subtraction of the binding energies. These measurements were made at four different positions of each sample to investigate both the homogeneity of the sample surface and the reproducibility of the Cu L_3 measurements. It is quite clear that the spread between the four spectra of each material is smaller than the shift between the edges of the samples themselves.

It was also attempted to correlate the fluctuations in the band edges with the positions of the core levels as well as with the local concentrations of Cu, In, S and Ga. However, no correlation between any set of parameters was found which further supports the detachment of the XPS-measured properties of the sample surfaces from those properties measured with NEXAFS.

Because the half-maximum was used to evaluate the energetic position of the edge, as opposed to a linear extrapolation as is the case with UPS valence band measurements, this source of error is not as critical as it is with UPS. It should be called to attention that this method of evaluation was only possible because relative differences were sought. If absolute positions were the final goal, another form of analysis may have been more

appropriate.

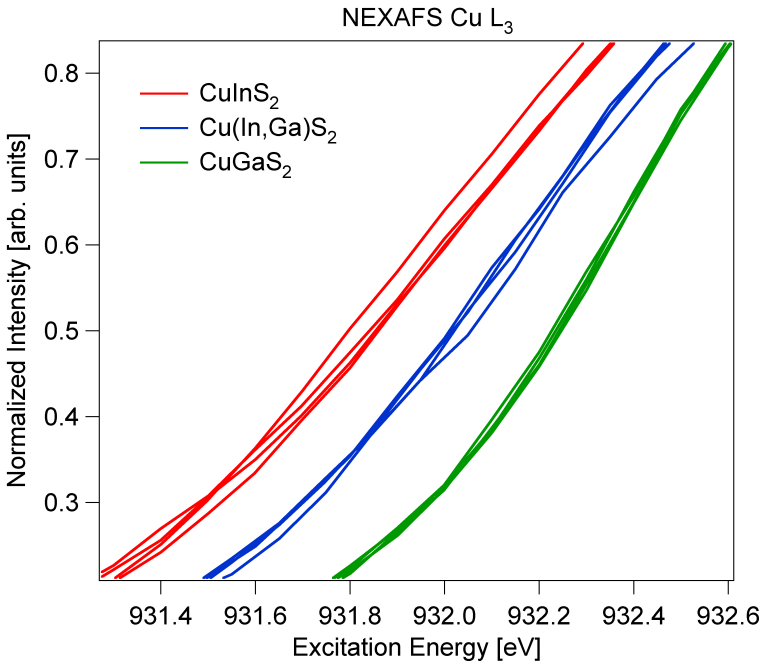


Figure 41: The spread in the values of the absorption edges of CIS, CIGS and CGS at four different positions on each sample can be seen to be under 0.1 eV. This is noticeably smaller than the shifts between the absorption edges of the different elements themselves.

This means that the main source of error for these measurements is caused by the calibration of the spectra using the mirror current discussed in sec. 7.2.1. This has been determined to be ±100 meV for the Cu L_3 spectra after completing the fitting of the corresponding mirror currents. However, as can be seen from fig. 41, where the CIS and CIGS spectra were measured directly after one another, the error in the measurements where no calibration was needed is smaller than ±100 meV. Due to this high reproducibility of these spectra, the final error for the Cu L_3 spectra is ±30 meV

This is, however, different for the S L_3 spectra.

7.3.3.2 S L_3 Absorption Edges Fig. 42 shows the S L_3 edges from CIS, CIGS and CGS which, according to [21], measure the S 3d states in the conduction band. In this case, in contrast to the Cu L_3 spectra, because the binding energies of the S 2p core levels were not studied in as much detail as were the Cu 2p levels, the binding energies measured with the NEXAFS spectra were subtracted from the edges in fig. 36 d), although reasons against doing this have already been given. In the case of S, however, the "surface effects" have the smallest impact. All core levels of Cu, In, Ga and S were measured with 1150 eV excitation energy, giving the S 2p levels of the highest information depth from the four elements. At the same time, the NEXAFS measurements have the lowest information depth due the low excitation energy need to excite the S 2p core level. This observation is supported by the realistic results obtained from the S L_3 spectra after subtraction of the S 2_p core level binding energies.

These values were 161.85 eV, 161.70 eV and 161.45 eV for CIS, CIGS and CGS, respectively, although it can be found in literature, as with Cu 2p, that there is no difference between CIS and CIGS [123]. The subtraction of these binding energies is not completely physically justified, however, it does not alter the order of the spectra when compared to fig. 36 d), leading again to the interpretation of an opening of the band gap through a shift in the conduction band with increasing Ga concentration. These spectra were also calibrated with their corresponding mirror currents, which contained much broader

structures than the Cu L_3 mirror currents, leading to a larger error of ±300 eV, as will be discussed in the next section.

But first, it is interesting to point out several features of the S L_3 spectra.

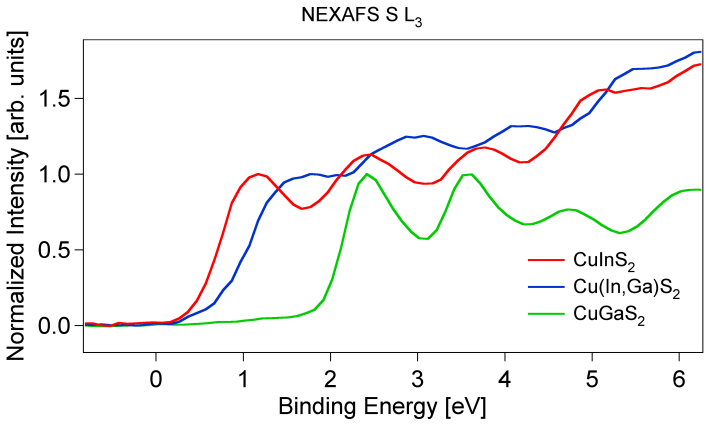


Figure 42: S L_3 absorption edges from $CuInS_2$, $Cu(In,Ga)S_2$ and $CuGaS_2$ after the subtraction of the measured S $2p_{3/2}$ core level binding energies not corrected for surface effects. The large shift between $Cu(In,Ga)S_2$ and $CuGaS_2$ is reflective of the large change in band gap between the two materials.

As already mentioned, the order of the S L_3 spectra also suggests an opening of the band gap with increasing Ga content. If one looks at the differences in the band edge positions one finds differences of 0.4 eV between CIS and CIGS and 1.1 eV between CIGS and CGS. While both shifts are somewhat larger than those found with the Cu L_3 edges, the shift between CIGS and CGS is only slightly larger than the 1 eV shift expected with the bulk band gap estimates. In fact, if one takes the energy scale to be absolute the values of $E_c - E_f$ for CIS, CIGS and CGS, respectively, are 0.7 eV, 1.0 eV and 2.1 eV. This results in surface band gap values, again after the addition of the values for $E_f - E_v$ from fig. 35, of 1.4 eV, 1.7 eV and 2.5 eV for CIS, CIGS and CGS, respectively. These values are much more similar to the bulk band gap values than those calculated with the Cu L_3 edges leading to the conclusion that the effect of the band distortion may be much reduced when using the the S L_3 edge. This is further supported by the larger shift between CIGS and CGS as would be expected to accommodate such a large increase in band gap from 1.6 to 2.4 eV. In fact, this shift is so large that after consideration of the error of ±300 eV it can still be considered real.

It can also be shown with the S L_3 spectra, as was the case with the Cu L_3 spectra, that the structure of the conduction band, as reflected by the portion of the absorption curve after the edge (>1 eV for CIS, >1.5 eV for CIGS and >2.5 eV for CGS), that the conduction bands of CIS and CIGS are much more similar to each other than to that of CGS.

7.3.3.3 S L_3 Mirror Current The energy calibration of the S L_3 edges was difficult because, as can be seen in fig. 43, the structures found here are much wider than in the Cu mirror current spectrum, fig. 34. While the latter has dips of about 2 eV in width, the peaks shown here are at least 5 eV wide and are very noisy (these are smoothed spectra). Due to this, the structures were fitted, although an accuracy of better than ±300 eV could not be reached. And because the S L_3 spectra were not measured one after the other (In was measured in between), an energy-calibration with the mirror currents was essential, leaving the measurements shown in fig. 42 with a relatively large error.

In fig. 43, one finds several arrows indicating where different fits and calibrations were attempted. Shifts determined through fits of one structure did not correspond to shifts determined through fits of another structure, that is, the calibration-shifts derived from one fit were unique to that fit. In total, four calibrations were done, two on the first dip, one from about 158 to 164 eV and another more narrow one from about 160 to 165 eV, both centered on what appears to be the base of the trough at about 162.5 eV. The third fit was of the peak in the middle from 165 to 171 eV also centered around 165.5 eV while the fourth calibration was done on the edge that appears by the arrow to the far right. For this last calibration no shift was necessary as the edges were already aligned, which leads, of course, to the spectra as they were measured. The first three fits, while it was attempted to make them have some kind of physical sense, were very questionable; a small variation in the energy region chosen for the fit led in some cases to several tenths of an eV difference in the edge shift. The alignment of the small edge, while in itself simple, is also questionable because of the noise and, moreover, it is unlikely that no calibration is needed in this case.

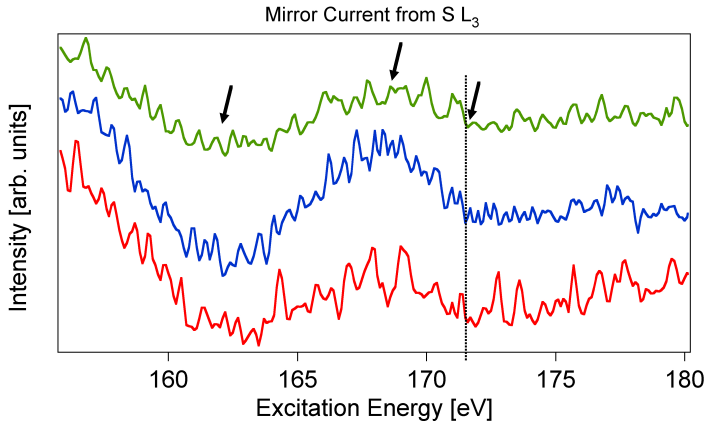


Figure 43: Mirror current spectra (smoothed) measured parallel to the S L_3 spectra. The difficulty in calibrating the S L_3 spectra can be seen here because of the width of the mirror current structures and low signal-to-noise ratio. The arrows indicate features fitted for different calibrations of the S L_3 spectra.

The spectra shown in fig. 42 are the result of the fit of the central feature in fig. 43 at 168 eV because it was seen as the "most comfortable" fit.

However, it is interesting to note that while the four calibration attempts resulted in differing positions for the all three edges, the CGS edge was always separated from the other two edges by between 0.7 and 1.0 eV. This lends credence to the notion that the effect of the core hole indeed decreased by the use of the shallow S 2p core level. The edges from CIS and CIGS, although they crossed one another in some fits due to their different slopes were, in all but a few scenarios, in the same order as the Cu L_3 spectra.

7.3.3.4 In $M_{4,5}$ and Ga L_3 Absorption Edges The In $M_{4,5}$ edge, which like the In L_1 edge measures hybridized In p + S (p,d) states according to [21], and the Ga L_3 edge found in fig. 36 show, in contrast to the Cu L_3 and S L_3 edges, no shift with higher Ga concentrations. As mentioned, this means either no change in the electronic positions of the core levels and end states with the addition of Ga, or an exact parallel shift between these states, keeping their energy difference exactly the same. The second situation is unlikely because shallow levels in the valence and conduction bands are effected by changes in the surrounding atoms of the lattice more than core levels. A parallel shift would cor-

respond to a change in the surrounding lattice effecting the conduction band states and core levels equally.

The In $M_{4,5}$ and Ga L_3 spectra are shown again in fig. 44 a) and b), respectively, after the subtraction of the corresponding core level binding energies. The measured values were 444.80 eV and 444.55 eV for In $3d_{5/2}$ in CIS and CIGS, respectively, while for Ga $2p_{3/2}$ the values for CIGS and CGS were 1117.30 eV and 1117.35 eV, respectively. As was the case with S $2p_{3/2}$, the measured core level binding energies were used without corrections for surface effects.

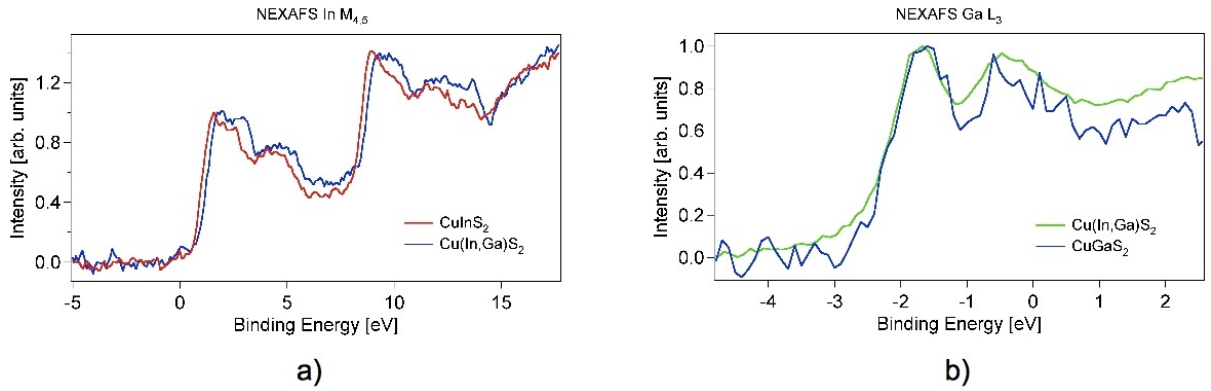


Figure 44: In $M_{4,5}$ and Ga L_3 absorption edges after the subtraction of the measured binding energies which were not corrected for surface effects.

While the Ga L_3 spectra show essentially no shift before or after the subtraction of the binding energy, there is a difference in the measured binding energy of the In $3d_{5/2}$ core level. However, because fig. 36 b) would correspond to a parallel shift between the In $3d_{5/2}$ core level and the end state of the absorption in the conduction band or no change in either state, the difference in measured core level binding energy is more likely a surface effect similar to the that seen in the other core levels in this chapter, causing the binding energy measured with XPS to differ from the binding energy of the core levels excited during the NEXAFS experiments. The same In 3d core level binding energy in CIS and CIGS is also found in literature [123].

Thus, the most likely interpretation of the In $M_{4,5}$ and Ga L_3 measurements is that the effect of the higher Ga concentration on the core level and conduction band binding energies of these two elements is smaller than the ±100 meV error of the measurements.

Therefore, the substitution of Ga for In, that is, one group III element for another, results in only small (<100 meV) changes in the elements' electronics states. This is supported by the lattice structure of $Cu(In,Ga)S_2$ as it can be seen that the two elements have no common bonds.

7.3.4 The Cu L_3 Edge After CdS Deposition

The Cu L_3 absorption edge was also measured on the three absorbers after a short (40 sec, 0.7 nm) CdS deposition in order to investigate any possibly resulting chemical shifts on the absorber surface which may not be detectable by XPS because the shifts here can involve conduction band states in addition to the core levels. And these shifts would have an influence on the conduction band offset between the CdS and CIS. Band bending effects, such as those seen in XPS/UPS (chapter 6), will, however, not be seen in NEXAFS.

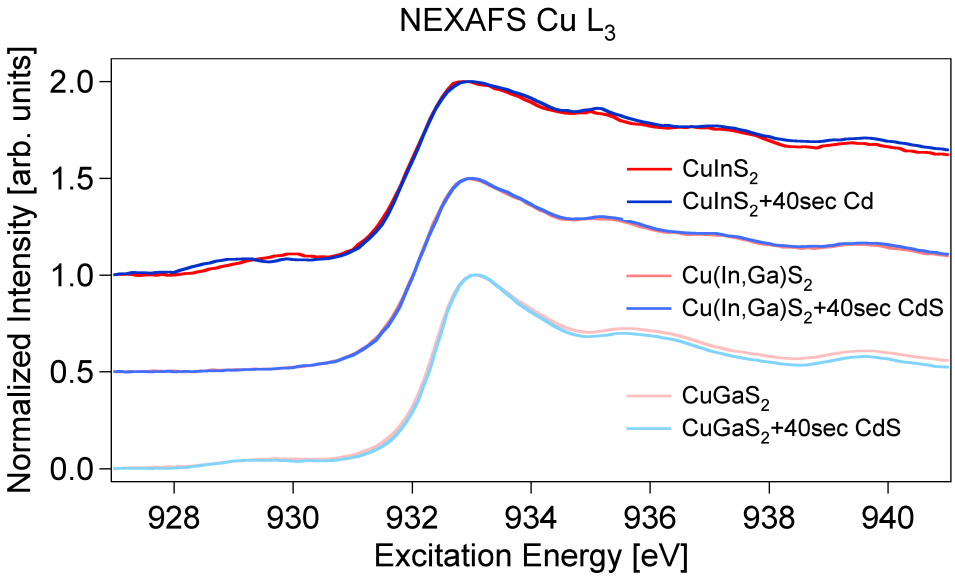


Figure 45: Cu L_3 spectra from $CuInS_2$, $Cu(In,Ga)S_2$ and $CuGaS_2$ before and after CdS deposition. Spectra are normalized to the absorption edge maximum and shifted vertically for clarity.

As can be seen from fig. 45, apart from slight differences in the slope of the edge and light fluctuations in the post-edge region, the spectra before and after the CdS deposition are the same.

Although it is still thought that indeed there is a chemical interaction between the absorber surface and the Cd from the chemical bath with Cd diffusing into the absorber and Cu diffusing into the CdS, the affected area must be small in comparison to the information depth of 15-20 nm limiting the diffusion of the Cd into the absorber surface to several nm. However, it is exactly this thin layer which may play a deciding role in the CIGS/CdS junction.

The In $M_{4,5}$ and S L_3 edges were not measured here. It is probable that Cd occupies a Cu lattice position and therefore binds to S atoms [79, 89, 94], thus making S a good candidate to measure, although differences between the Cd-S bonds in CIS:Cd and Cd-S bonds in CdS may be extremely hard to detect. Cd $M_{4,5}$ edges were not measured on these samples and may be useful when compared to measurements on thicker CdS layers

although the same difficulty in distinguishing between Cd-S bonds would still apply.

7.4 Inverse Photoelectron Spectroscopy (IPES)

The positions of the conduction band edge were also measured with inverse photoelectron spectroscopy (IPES). As discussed in sec. 3.5, IPES, while avoiding the problem of the core hole, has other problems deriving from the introduction of a new charged particle, an electron, into the system. This may lead to a charging of the sample if the excess charge is not conducted away from the sample fast enough. Charging effects, like with XPS, can lead to changes in the electronic positions of the measured states and, thus, the position of the conduction band edge. And as will be seen, the sample currents found during IPES were much higher than those found while doing XPS experiments.

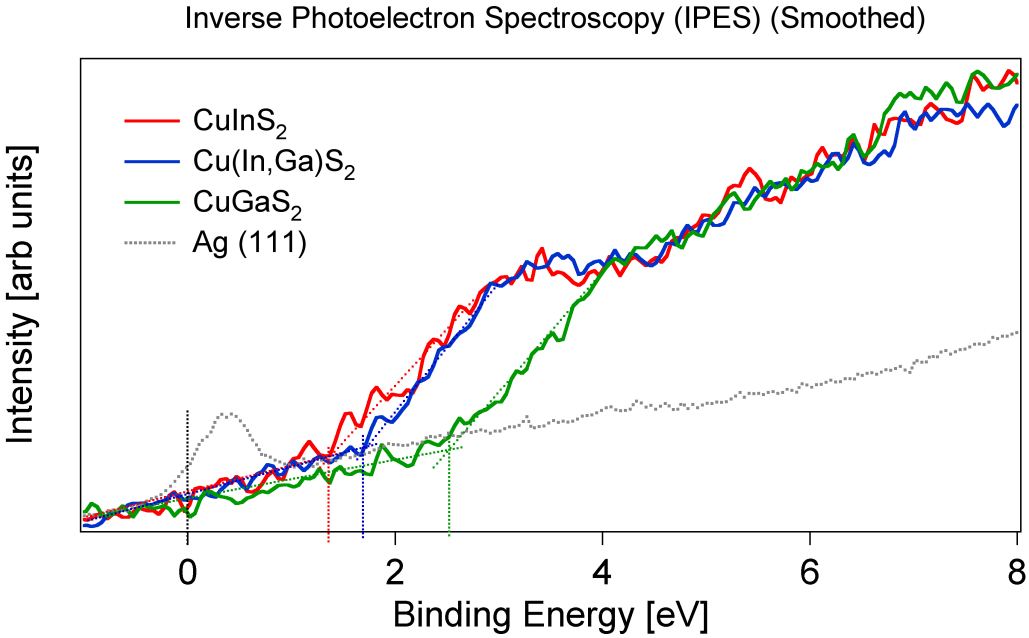


Figure 46: Inverse Photoelectron Spectra for $CuInS_2$, $Cu(In,Ga)S_2$ and $CuGaS_2$ with E_f measured on a Ag (111) crystal. Despite the low signal-to-noise ratio, the large shift between CIGS and CGS can be seen corresponding to the large change in band gap.

In order to avoid charging effects, the current from the electron gun was reduced as far as possible while still retaining a signal. However, as can be seen here, the spectra are noisy, although 25 scans were done with a sample current of $\sim 0.15\,\mu$A (compared with pA or nA in XPS). The next round of measurements will see a larger step size and reduced energy region in order to reduce total measurement time in an attempt to avoid charging.

The curves in fig. 46, in spite of the noise, are meant to be compared to the NEXAFS measurements already discussed. Therefore, analogue to the NEXAFS measurements, the values for $E_c - E_f$ as measured by IPES can be obtained from fig. 46, with the

position of the spectrum being determined by linear extrapolation similar to the UPS valence band measurements. For CIS, CIGS and CGS, respectively, the values are 1.35 eV, 1.70 eV and 2.50 eV. These values added to the values for $E_f - E_v$ from fig. 35 result in surface band gaps of 2.05 eV, 2.40 eV and 2.90 eV for CIS, CIGS and CGS, respectively.

It can immediately be seen here, as in the Cu and S L_3 spectra, that the band gap of CIGS opens with increasing Ga content, as the order of the spectra is the same here as in the NEXAFS spectra.

Both the shift of 0.35 eV between CIS and CIGS and 0.80 eV between CIGS and CGS are more similar to the values determined with the S L_3 edges than those determined with the Cu L_3. Although in this case, as with the S L_3, the shift between CIGS and CGS is indeed due to a real shift in the conduction band between the materials, the difference between the CIS and CIGS is too small to be supported by measurements of such poor quality.

The error in these measurements is very difficult to estimate because of the low signal-to-noise ratio of the IPES spectra. However, because the error should reflect the fact that the shift between CIS and CIGS cannot be fully supported by these measurements, but the shift between CIGS and CGS can, the error has been set at ±400 meV.

The reference for the IPES measurements was freshly sputtered Ag (111), seen as the dotted gray line in the fig. 46. The zero of energy was taken to be the point where the Fermi function equals 1/2, like all XPS and UPS measurements and not at the foot of the Fermi edge structure.

7.5 Evidence for charging with IPES

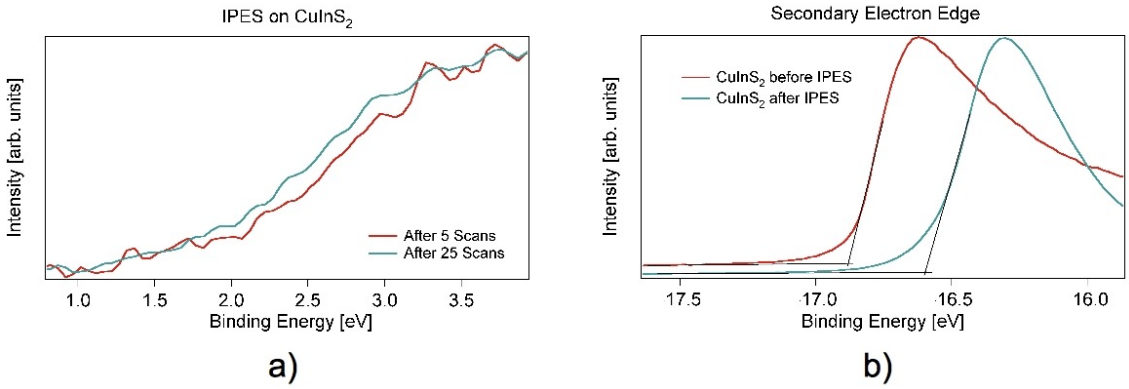


Figure 47: Charging effects in during an IPES experiment. a) shows the shift between the 5th and 25th scan of the IPES measurement while b) shows the corresponding change in the work function of the sample. This change in the sample can be clarified by a surface dipole.

As briefly stated above, the possibility that IPES measurements may be influenced by

charging must be considered. To investigate this, the evolution of the IPES spectra were followed by observing the placement of the edge after 5, 10, 15, 20 and 25 scans. The spectra in fig. 46 displayed no difference in the position of the edge and changes in the work function of no more than 3 meV. As mentioned, the sample currents for these spectra were $\sim 0.15\mu$A. Before these measurements were made, however, other measurements were done at higher electron fluxes. In this case the sample currents were higher, $\sim 1.5\mu$A, and charging effects and/or beam damage were indeed seen.

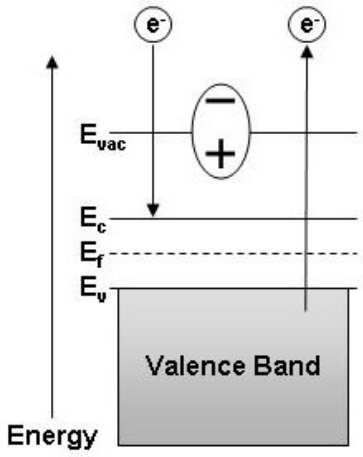


Figure 48: Schematic diagram of a surface dipole induced by electron injection during an IPES measurement leading to a shift in the measured conduction band edge and the secondary electron edge measured with UPS indicating a change in the sample's work function.

Fig. 47 a) shows the initial IPES measurement on CIS at the higher sample current after 5 scans and after 25 scans and a shift of about 150 meV is clearly visible toward smaller binding energies. The corresponding secondary electron edges from UPS measurements before and after the complete IPES measurement are shown in fig. 47 b). Here the shift is somewhat larger, about 300 meV, and corresponds to an increase in the work function of the sample.

A surface dipole induced from electron injection during the measurement as seen in fig. 48 would have such an effect, although from this model one would expect that the shift would be the same in both figs. 46 a) and b). One explanation for this discrepancy is that the shift in the IPES edge is not shown using the first and last (25th) scans, but rather the fifth and 25th in order to display a more coherent edge. The spectrum after one scan was unusable. The work functions, on the other hand, were measured before and after the complete measurement. Also, it is plausible that the charging effect fluctuates in time.

A dipole with the orientation seen in fig. 48 would cost an electron exiting the sample energy, thus giving the appearance of a larger work function while at the same time increasing the energy of an electron from the electron gun entering the system, thereby shifting the position of the conduction band edge toward the zero of energy, E_f.

Another explanation is that the observed effects are not only due to charging but also due to damage to the sample caused by the electron beam. This is supported by the fact that the observed changes were not completely reversible when new measurements were done, although there was a return toward the initial state. One would expect that a charged sample would eventually discharge, while a damaged sample would not revert to its original state.

7.6 Conclusions About the Methods NEXAFS and IPES

The experiments in this chapter, although directed at gathering information about the conduction band of CIS, CIGS and CGS and about the conduction band offset between these materials and CdS, were performed with methods which themselves still require some level of investigation. As was shown here, the interpretation of the results, especially in the case of NEXAFS, can be quite complicated and require assumptions to be made about the system, something which should be avoided if possible.

IPES has become an established method for determining the position of conduction band edges and, unlike NEXAFS, measures the complete density of unoccupied states. However, in order to avoid charging effects with low-conductivity samples during the measurement, the current from the electron gun must be reduced to a point which causes severe deterioration of the signal-to-noise ratio. As was seen, this causes a loss of much of the information contained in the measurements. In addition, the surface band gap attained from IPES and UPS measurements for some samples was suspiciously large; the surface band gap of CIGS increased by 0.8 eV compared to the bulk. Although this could be explained by the existence of a surface phase different from the bulk, it may also be a charging effect or even a surface phase created through damage from the electron beam.

While NEXAFS does not suffer from poor signal quality, even Ga L_3 was measurable in CIGS, other problems make this method difficult to interpret. These are the effects of the core hole on band positions and the LDOS sensitivity of the measurement. With a proper knowledge of the structure of the conduction band the latter problem is, however, less critical.

In the case of ill-defined samples like those investigated here, surface effects can also adversely effect one's ability to measure binding energies or define a proper energy scale for the NEXAFS measurements. The latter is even more profoundly effected by the problem of calibrating the excitation energy. Even with proper elemental references, absolute edge energies are difficult to define as are binding energies, as is evidenced by searches of literature and data banks.

In spite of these problems, however, it seems that at least qualitative conclusions are possible in some cases as was shown here: the opening of the CIGS band gap with increasing Ga content was seen with both methods.

7.7 Conclusions About the Conduction Band

With increasing Ga concentration, it was shown through UPS valence band spectra and conduction band measurements employing NEXAFS and IPES that the band gap of $Cu(In,Ga)S_2$ widens. In the case of $CuInS_2$ and $Cu(In,Ga)S_2$ (with $\sim$8% surface Ga concentration) this is due solely to a shift in the conduction band, although a small shift in the valence band is likely present, which is much smaller than the resolution of the measurement. This is supported by the fact that in $CuGaS_2$ both the valence band and conduction band shift toward lower binding energies, the conduction band compensating

for the shift in the valence band.

The reason for the shift in the valence band in CGS is the S 3p-Cu3d repulsion [94, 97] as the CGS surface is Cu-richer than the other two surfaces.

The change in the conduction band position is not due to a shift of the entire band but only due to the partial densities of states seen by the Cu 2p and S 2p core levels as these displayed a shift with differing Ga concentration. The partial densities of states seen by the In 3d and Ga 2p core levels displayed no shift and are, thus, independent of Ga concentration.

Table 3: Values of E_g for CIS, CIGS and CGS determined by different methods.

Material	UV-VIS (Bulk)	Cu L_3/UPS	S L_3/UPS	IPES/UPS
$CuInS_2$	1.5 eV	2.45 eV	1.40 eV	2.05 eV
$Cu(In,Ga)S_2$	1.6 eV	2.60 eV	1.70 eV	2.40 eV
$CuGaS_2$	2.4 eV	2.70 eV	2.50 eV	2.90 eV

The apparent surface band gaps deduced from the various methods in this chapter are collected in table 3 along with bulk band gap values from optical UV-VIS experiments.

While there is a high degree of deviation, the bulk values correlate with the S L_3 values while the Cu L_3 values correlate with the IPES values. Interesting to note is that all values with the exception of CIS measured with S L_3 indicate an opening of the band gap toward the surface as has been indicated in literature [107, 126].

Although many arguments were given in the chapter why only trends should be considered here, one real shift was noted in the Cu L_3 spectra between CIS and CIGS where the 150 meV$\pm$30 meV shift is attributed to a real opening of the band gap of the same magnitude due to the inclusion of Ga in the CIS lattice. This means that the addition of Ga to the CIS absorber actually exacerbates the step in the conduction band, ΔE_c, between the CIGS and CdS although the open circuit voltage, V_{oc}, increases by $\sim$100 mV.

The next chapter takes a general look at valence band measurements and analysis using different excitation energies. It is meant to make general statements about the methods as opposed to considering the $CuInS_2$/CdS system specifically, although these materials are again the subject of investigation. Because of the importance of these measurements to this thesis, it is fitting to consider possible differences in the experimental methods.

8 General Aspects of Valence Band Measurements and Analysis

The position of the valence band edge plays a very important role in this work. The method of measurement and the analysis of the spectra to determine the valence band edge position is varied in literature and often looked upon critically. In this section, therefore, valence band measurements using different radiation sources made on $CuInS_2$ and ∼35 nm CdS deposited on CIS[22] are considered. The differences are compared and discussed, along with the method of determination of the position of the valence band edge. Although some of the measurements and the materials in question are identical to those in the preceding chapters, the statements made here are meant to be applied to valence band measurements in general and how the current method of analysis of such spectra, UPS, XPS, XES or otherwise, still poses some difficulties.

The method used to evaluate the measured UPS valence band edges in this thesis has mainly been to extrapolate the last linear section of the spectrum thought to belong to the upper most valence band and determine the intersection of this linear extrapolation with the background signal. This point is the valence band edge (see sec. 3.2.5). To be sure, there is no way of knowing from the spectrum alone if this is the correct position of the valence band edge, however, other knowledge about the system, such as the band gap or other characteristics learned through literature searches, can help to narrow down the possibilites. It is also helpful to perform many measurements on the same or similar samples and observe the differences in the measured spectra. A true valence band edge, determined by the material under study will be a recurring phenomenon in the UPS spectra while other features caused by, for example, a contaminated surface, will not be recurring.

Although the method of linear extrapolation is not always justified on physical grounds, it is the method of choice in the literature, thus making new experiments also evaluated with this method, such as those in this thesis, directly comparable to work already done. Apart from this, there are also certain physical reasons why this method of evaluation can be justified. For example, the extremely thin line width of UPS excitation energies (3 meV for He I [11]) has essentially no influence on the line shape. Furthermore, the electron analyzer set at 2.5 eV pass energy will have a slightly larger, yet still very small effect on the measured spectral features. However, there is still some broadening, the effect of which cannot be completely known until a valence band density of states has been obtained. And this is, of course, the objective of the UPS measurements.

To complete the argument for the linear extrapolation, however, the valence band edge consists of many overlapping non-localized states, which, as a sum lead to a flank moving toward the valence band edge. And in UPS measurements it can be seen that this flank approaches zero, as it must at the valence band edge. Often a small amount of smearing can indeed be seen at the position of the valence band edge where the upper most valence band and the background come together. This smearing is calculated away when using the linear extrapolation method as can be seen in fig. 3 b).

[22] This sample is often simply referred to as "CdS" hereafter.

As mentioned, the method of choice when trying to increase the level of physical meaning of the analysis of valence band spectra would be to have a density of valence states for the system under scrutiny which would then be broadened to account for excitation and instrumental line widths and weighted to account for the different ionization cross sections of the different electrons in the spectrum. However, a measured density of states is the result of proper valence band measurements, not available until after the analysis of said measurements is completed. Another possibility is calculated band structures. While usually offering the correct order of electronic states, these calculations often show discrepancies between measured and calculated electronic positions. Density functional theory calculations of the density of valence states for CIS and CdS were in fact attempted during this thesis without success.

Another approach would be to assume a general density of states. If one limits the investigation of the valence band to just the valence band edge in order to determine its position, which is the important value in this thesis, a very physically sensible solution would be to consider a general density of states arising from the periodic nature of the lattice found in both materials under investigation here [128, 129].

The parabolic density of states at the valence band edge in a semiconductor arising through the effective mass approximation is a plausible, simple ansatz [35].

8.1 The Parabolic Band Approximation in a Semiconductor

In the effective mass approximation the electron dispersion near the minimum or maximum of a parabolic band is given by

$$E(k) = E_0 \pm \frac{\hbar^2}{2m^*}(k_x^2 + k_y^2 + k_z^2) \tag{26}$$

where m^* is the effective mass of the electrons in the band and is given by $m^* = \frac{\hbar^2}{d^2E/dk^2}$ [35].

This is very similar to the result of the free electron in a metal with the substitution of the effective mass m^* for the real mass m.

The number of states between the energies $E(k)$ and $E(k) + dE$ is given by

$$dZ = \frac{1}{2}\frac{\pi k^2}{(\pi/L)^3}dk \tag{27}$$

where L is the length of the crystal, assumed here to be cubic.

With $dE = (\hbar^2 k/m^*)dk$, the density of states per crystal volume, $D(E)$, can be computed after taken into account the electron spin:

$$D(E) = \frac{dZ}{dE} = \frac{(2m^*)^{3/2}}{2\pi^2\hbar^3} E^{1/2} \tag{28}$$

Thus, near the valence band edge the density of states can be approximated by a parabola, $D(E) \sim E^{1/2}$ [35]. This is obviously not true for deeper lying states: as can be seen from the valence band spectra from any semiconductor, the valence band densities of states become very complicated very quickly.

The only problem remaining is that UPS is a very surface sensitive method whose signal may be dominated by the broken symmetry and electronic states of the sample surface, therefore making eq. 28 less physically probably. However, if one were to use a higher excitation energy, such as Mg Kα, gaining more of the signal from the first 3 nm of the sample and not just the first atomic layers, the use of eq. 28 as a density of states at the valence band edge may be more justified, although the sample surface still makes the largest contribution to the total intensity.

This is what has been done here: valence bands of CIS and thick CdS layers on CIS are measured with XPS and UPS and the resulting valence band shapes and positions of the valence band edges compared.

As with the UPS spectra, the energy scale of XPS measurements must be calibrated with a Fermi Level measurement. For consistency, a Fermi distribution function

$$f(E) = \frac{1}{e^{(E-E_f)/k_bT} + 1} \tag{29}$$

was fitted to Au Fermi Level spectra measured with XPS in order to determine the zero of energy.

In the following sections when discussing the fits of the various spectra which were made using the program Maple 11, the Fermi Level was represented by the following equation

$$f := x \rightarrow \left(b * \left(1 - \frac{1}{1 + exp\left(\frac{x-s}{n}\right)} \right) + y \right) \tag{30}$$

meaning that the function f is defined to be a function of x. The equation itself is actually the Fermi function for unfilled states $(1 - f(E))$ because of how maple loaded the spectra.[23] Further differences to eq. 29 are the factor b enabling the scaling of the step in the Fermi function to fit the measured spectrum, y which accounts for background and s which shifts the energy where $f(E)$ is equal to 1/2. In the final fit, s was always equal

[23]Maple loaded the spectra as the mirror image of the normal representation; the spectra have been flipped back for display here.

to zero[24] but initial stages of the fitting process required a finite value of s in order to determine the shift required to bring the Fermi Level of the measurement to the zero of the energy scale. The remaining factor is n, which was set to $n = 0.0259\,\mathrm{eV}$, being equal to kT at 300°K.

The XPS valence band spectra were fitted in a similar fashion using the Maple input

$$p := x \rightarrow piecewise\left(x > q, ((4r(x-q))^{1/2} + p, x < q, p\right) \tag{31}$$

to represent the parabolic density of states, $D(E) \sim E^{1/2}$, at the valence band edge.

This equation, p, also defined as a function of x, is plotted piecewise. For $x > q$, a parabola is scaled with the factor $4 * r$ to fit the measured spectrum analogous to b above.[25] The next variable, q, like s, shifts the position of the parabola in order to obtain the best fit to the spectrum and p, like y above, takes the background into account. For this reason, the entire function is set equal to p for $x < p$, that is, after the density of states has gone to zero. After the fit is finished the value of q is equal to the valence band edge.

In both the case of the Au Fermi Level and the valence band edge, the raw functions, eqs. 30 and 31, had to be broadened with a Gauss function in order to attain a realistic fit.

This was done in Maple with the following equation:

$$g := x \rightarrow \left(\frac{1}{a(2\pi)^{1/2}} exp\left(-\frac{x^2}{2a^2}\right)\right) \tag{32}$$

This function, g, again defined to be a function of x, is a simple Gauss distribution

$$g(x) = \frac{1}{a\sqrt{2\pi}} e^{-\frac{1}{2}\frac{(x-m)^2}{2a^2}} \tag{33}$$

normalized so that $\int_{\infty}^{\infty} g(x)dx = 1$. The "spread" a is related to the full width at half maximum (FWHM) through

$$FWHM = 2a\sqrt{2ln2} \tag{34}$$

[24] In fact, s could not be set to zero because Maple could no longer make the necessary calculations to complete the fit. s was, thus, routinely set to something on the order of 10^{-4}, well below the accuracy of the measurement.

[25] There is no special reason why the factor of 4 was not absorbed into r for the fitting process. This form of the equation comes directly from the definition of a parabola, $y = \sqrt{4ax}$, making $2r$ equal to the focal parameter.

as can be shown through a simple calculation. m can be used to shift the center of the Gauss distribution. This was, however, not needed here as will be explained in the sec. 8.2 and m was always set to zero.

When performing XPS measurements, as stated in eq. 2, the measured line width consists of contributions from the intrinsic line width of the measured peak, the line width of the excitation source and the analyzer resolution. The way the line widths, or distributions describing the line widths, interact in order to result in the measured line shapes is a mathematical process called a convolution.

8.2 The Convolution

The convolution, $(f * g)$, of two general functions $f(t)$ and $g(t)$ is defined to be [127]

$$(f * g)(t) = \int_{-\infty}^{\infty} f(\tau)g(t-\tau)d\tau \tag{35}$$

or, as inputed into maple

$$h := x \rightarrow int(f(x)g(t-x), x = x_1..x_2) \tag{36}$$

Here, again, h is defined to be a function of x where x_1 and x_2 define the limits of the integration. These do not necessarily have to be set to infinity, but must cover the desired region over which the convolution is to be carried out.

At this point τ and t are simply variables without any physical units. Important, however, is that they represent two possibly different values of the same variable, for instance time or energy. Thus, the argument $(t-\tau)$ would represent a time or energy difference which changes, in the case of the convolution, with t.

The convolution, therefore, describes the amount of overlap between two functions as one moves past the other, as is the case when an electron analyzer, set in changing energy mode, "moves" past the the resulting kinetic energy of each core level after excitation.[26]

This is illustrated in fig. 49, where two Gaussians, both centered at zero ($m = 0$), and their product are shown for different values of t. In each part of the figure, a)-e), the yellow curve represents the function $f(\tau)$ and the green curve $g(t-\tau)$ in eq. 35. As the variable t changes, $g(t-\tau)$ is seen to "wander" past $f(\tau)$, the two functions lying directly over one another at $t = 0$. And finally, the red curve represents the product of the two, $f(\tau)g(t-\tau)$ (but not the integral of the product!!).

[26]The core level with its rather simple shape will be used here for the purposes of illustration, although this chapter deals with the valence band. This is because the shape of the core level is much more convenient than envisioning a convolution of a Gauss function with the complex form of a valence band. However, the processes are analogous.

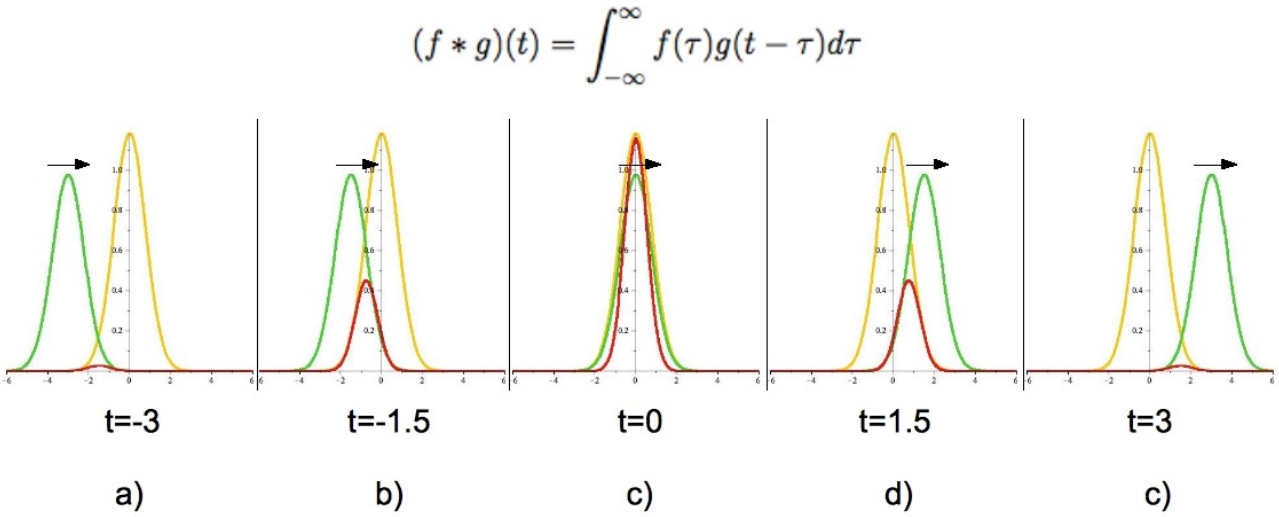


Figure 49: The functions $f(\tau)$ (yellow) and $g(t-\tau)$ (green) plotted as a function of τ with different values of t. The red curve is the product of the two functions f and g, the area under which is equal to $\int f(\tau)g(t-\tau)d\tau$ in eq. 35. The area of each red curve at a specific value of t is thus one point in the curve when $(f * g)$ (eq. 35) is plotted against t.

The area under the red curve is, however, the integral of the product of the functions $f(\tau)$ and $g(t-\tau)$ at a distinct value of t, which is exactly the term $\int f(\tau)g(t-\tau)d\tau$ in eq. 35. Therefore, the areas under the five red curves in fig. 49 a)-e) represent eq. 35 at five different values of t and, thus, represent five different points of the resulting convolution of the functions $f(t)$ and $g(t)$.[27]

If one were to plot eq. 35 vs. the variable t, the result would be the convolution, the individual points of which are the various areas under the red curves in fig. 49 at all corresponding values of t.

A good animated example of the convolution can be found at [130].

An interesting aspect of the convolution between Gauss distributions is that the resulting function is also a Gaussian whose spread, the variable a in eq. 33, is the square root of the sum of the squares of the spreads of the Gaussians involved in the convolution [131]:

If $f(x)$ and $g(x)$ are Gauss functions with spreads equal to a_f and a_g, respectively, then

$$(f * g)(t) = \frac{1}{(a_f^2 + a_g^2)\sqrt{2\pi}} e^{-\frac{1}{2}\frac{x^2}{(a_f^2+a_g^2)}} \tag{37}$$

[27]It can now be seen why m was set to zero in eqs. 32 and 33 above. As long as the integration limits, that is, τ, are selected so as to provide a *complete* overlap of the the Gauss function and the parabolic density of states, it does not matter where the Gauss distribution is actually centered. It is only the overlap at distinct *relative* positions between the two functions that is important.

the resulting spread being

$$a_{f,g} = \sqrt{a_f^2 + a_g^2} \tag{38}$$

The convolution with a third Gauss function $h(x)$ with spread a_h results then in

$$((f * g) * h)(t) = \frac{1}{\sqrt{(a_f^2 + a_g^2 + a_h^2)2\pi}} e^{-\frac{1}{2}\frac{x^2}{(a_f^2+a_g^2+a_h^2)}} \tag{39}$$

The FWHM of eq. 39 is thus, from eq. 34

$$FWHM = 2\sqrt{2ln2}\sqrt{a_f^2 + a_g^2 + a_h^2} \tag{40}$$

Comparison with eq. 2 in sec. 3.2, with the function f describing the line width of the excitation energy, g the that of the analyzer and h that of the measured electronic level, shows eq. 2 to be true up to the constant $2\sqrt{2ln2}$. However, this is again assuming that all distributions can be described by Gauss distributions. In fact, however, the intrinsic form of the measured line has a Lorentz form and when this is convoluted with a Gauss distribution, as would be the case during a measurement, the result is a Voigt profile. The FWHM of the convolution of a Gauss function and Lorentz function is more complicated than eq. 40.

Using the functions $f(x)$ and $g(x)$ once more, $f(x)$ remaining Gaussian in form while $g(x)$ is now Lorentzian, with the same symbol, a_f still representing the Gaussian spread while the FWHM of the Lorentzian is given by $2\Gamma_g$, the FWHM of the resulting convoluted function will be [132]

$$FWHM_{voigt} = 0.5139\Gamma_g + \sqrt{0.2134\Gamma_g^2 + a_f^2} \tag{41}$$

Despite all of this, eq. 2

$$\Delta E \sim (\Delta E_{ex}^2 + \Delta E_{an}^2 + \Delta E_{in}^2)^{1/2} \tag{42}$$

still conveys, in an albeit somewhat naive manner, the nature of the FWHM of the measured line shape and which values make important contributions to it.

In the analysis of the following XPS valence band and Fermi Level spectra, the Au Fermi Level was always fitted first. Because the intrinsic shape of this spectral feature is known, being determined through eq. 29 with the intrinsic broadening determined through kT,

the fitting of the Fermi Level demanded a Gauss function containing the broadening from the excitation source and the analyzer, both of which are actually Gauss functions, whose convolution also results in a new Gauss function. While fitting the Au Fermi Level, however, it was realized that the Gauss function needed to produce a good fit had a FWHM larger than would be expected from the broadening caused by Mg Kα and an electron analyzer run at 20 eV pass energy, as will be discussed below. Nevertheless, the Gauss distribution resulting from the fit of the Fermi Level was then used to broaden the valence band spectra of CdS and CIS, the intrinsic shapes of which are assumed to be described by the parabolic density of states described in eq. 28.

8.3 Valence Band Comparison: He I, He II, Mg Kα and Synchrotron Radiation

8.3.1 XPS Au Fermi Level Measurements

Fig. 50 a) shows a fitted Au Fermi Level spectrum measured with Mg Kα radiation. While this spectrum suffers, in contrast to the same measurement on a synchrotron, from a rather low count rate and satellite lines coming from the Mg source (see sec. 8.3.2 below), one of the sources contributing to its broadening, namely the excitation energy, is known to a high accuracy. In the case of the synchrotron measurement, although the broadening from the electron analyzer is the same as with the Mg measurements, the line width of the excitation energy is not as easy to obtain. For this reason the Mg measurement illustrates the problems encountered with the fitting of the Fermi Level better than the synchrotron measurements.

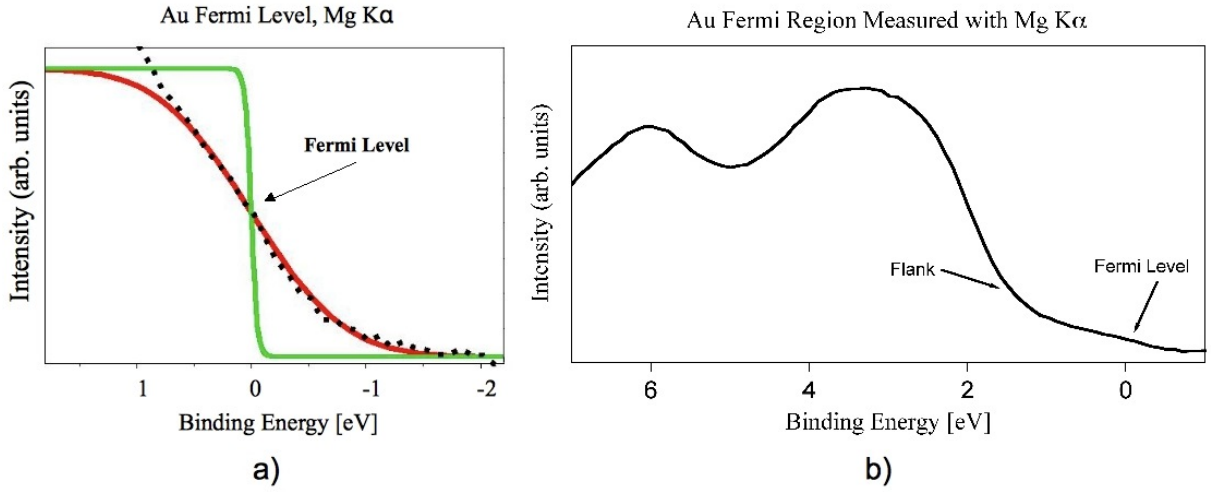


Figure 50: Au Fermi Level measured with Mg Kα radiation with satellites subtracted. a) shows the Fermi Level measurement (dotted line), the Fermi Function (green line) and the broadened fit (red line). In b) the Flank from the Au 5d and 6s orbitals can be seen. It is evident that part of this flank contributes to the signal at the Fermi Level causing increased broadening.

In the figure, satellite contributions to the spectrum have been removed. Although it

was seen that the subtraction of the satellites indeed influenced the form of the Fermi "Region" of the Au measurements, the position of the Fermi Level was nevertheless reasonable as will be discussed below.

The FWHM of the Gauss distribution used to broaden the Fermi Level measurement was expected to be about 0.73 eV including a 0.70 eV contribution from the Mg Kα line width and a 0.2 eV line width from the analyzer set at a pass energy of 20 eV.[28]

The FWHM needed to fit the Fermi Level spectrum well, was, however, at 1.51 eV, much larger.

The reason for this additional broadening can be seen in fig. 50 b). The flank extending down to the Fermi Level from the Au 5d and 6s orbitals alters the actual intensity from the electrons at the Fermi Level itself leading to increased broadening, as is evident from the FWHM of the Gauss function needed to fit the Fermi Level.

Using the zero of energy as determined through the fitting of the Fermi Level, the accuracy of this calibration was tested, in spite of the extra broadening, by determining the position of the Au $4f_{7/2}$ peak. The binding energy of this peak was found to be at 83.75 eV, in good agreement with literature values (83.70-84.25 eV) [124].

Thus, this zero of energy is an adequate calibration for the XPS valence band measurements.

The Au Fermi Level measurements made with synchrotron radiation extended to a maximum binding energy of 16 eV so that the corresponding Fermi Level fits could not, therefore, be checked against the position of the position of the Au $4f_{7/2}$ peak. However, when the zero of energy of both the synchrotron and Mg Fermi Level measurements were aligned, the positions of the Au 5d and 6s orbitals of both measurements were the same to within 100 meV. Thus, the Fermi Level fit to determine the zero of energy was also used for the measurements made with synchrotron radiation.

Due to the slightly poorer resolution of the synchrotron radiation compared to Mg Kα at the settings used for the measurement, the FWHM of the Gauss distribution used to fit the synchrotron Au Fermi Level was, at 1.82 eV, slightly larger than the Gaussian used for the Mg measurements. This increased broadening is due not only to the increased line width from the synchrotron, but also to an increased influence of the flank from the Au 5d and 6s electrons.

One other source of error brought about by the Au Fermi Level measurements with XPS brings us back to the *initial* and *final state rules* from sec. 3.4. Due to the core hole created by the high excitation energy, a distortion of the electronic states at the Fermi Level is possible and would lead to a systematic error for the XPS measurements.

[28] The value of 0.2 eV is derived from the standard rule of thumb that the FWHM of an electron analyzer is about 1% of the pass energy. The exact resolution of the analyzer used here at 20 eV pass energy is, however, not known.

To conclude this section, one final comment is needed about the application of the Gaussian determined by the Fermi Level fits to the XPS valence band spectra. It may be more appropriate to apply a Gaussian with a FWHM equal to 0.73 eV as was expected from the broadening due to the Mg Kα line width and the electron analyzer. However, as will be seen in the next section, the CIS and CdS valence bands also have other spectral features close to the band edge, similar to the Au 5d and 6s states near the Fermi Level. These may also cause a broadening of the valence band edge in addition to the Mg Kα line width and the electron analyzer.

Although the effect of these states on the valence band edges of CIS and CdS are probably different than the effect of the Au 5d and 6s electrons on the Fermi Level, the difference cannot be estimated without further investigation. Therefore, although it probably introduces a small additional error, different for CIS and CdS, the Gaussian used to fit the Fermi Level was also used to fit the valence band edges of CIS and CdS.

8.3.2 Mg Kα and Synchrotron Radiation

In this section, valence band spectra measured with He I, He II, Mg Kα and Synchrotron (1253.6 eV)[29] radiation are compared. Because of the problematic non-reproducibility of the samples, all spectra, when compared with one another, were measured on the same sample. The XPS valence band edge measurements have an error of $\pm$100 meV.

An important initial step before beginning analysis of the spectra measured with Mg Kα radiation was to check for and remove any satellite features which may augment the form of the valence band. These satellites arise from other emission lines of the Mg anode, which have a different energy and much lower intensity than the main Mg Kα_1 emission line. Satellites where subtracted here using the program Unifit [133].

Fig. 51 shows the valence band spectra from CIS and CdS measured with Mg Kα radiation. Both the curves with and without satellites are displayed.

Two satellite lines effect the spectra. Mg Kα_3 is 8.4 eV higher in energy than Mg Kα_1 and Mg Kα_4 is 10.2 eV higher [133]. Due to the binding energy of the In 4d (17 eV) and Cd 4d (11 eV) core levels for CIS and CdS, respectively, the satellite emission lines have different effects on the measured spectra.

In the case of the CIS, the In 4d satellite is projected onto a region of the valence band prior to the band edge. This double-feature can be seen in fig. 51 at $\sim$9 eV. The Cd 4d satellite, on the other hand, is projected exactly onto the valence band edge and, if it were not subtracted, would destroy any information contained therein. The difference in the position and form of the CdS VB edge can clearly be seen before and after satellite subtraction.

All subsequent Mg Kα spectra shown have had the satellites subtracted.

[29] This synchrotron energy was chosen because it is the same as the main Mg Kα emission line.

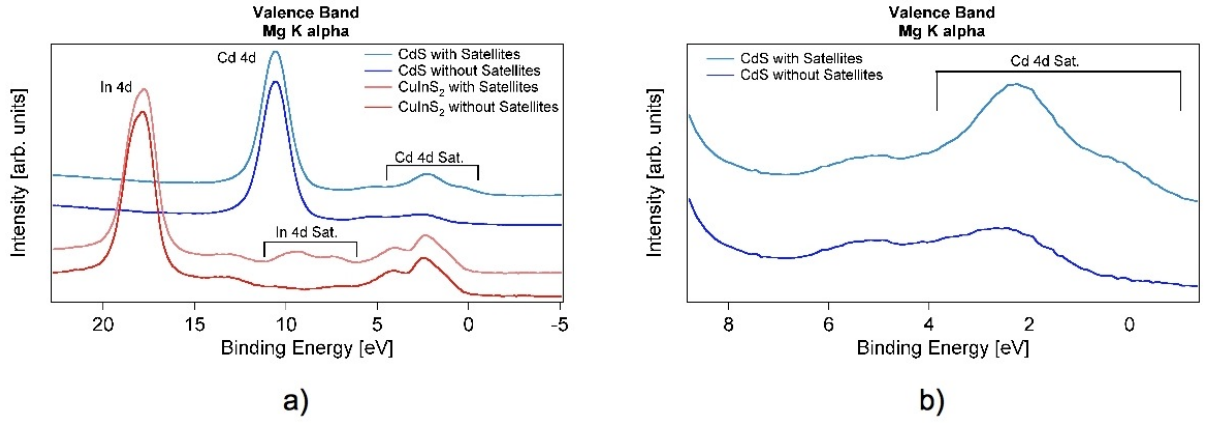


Figure 51: a) CIS and CdS valence bands measured with Mg Kα radiation, shown before and after satellite subtraction. While the satellites do not effect the valence band edge of the CIS, the valence band edge of the CdS is drastically altered. A blow up of the CdS valence band is shown in b).

In order to investigate whether the satellite subtraction was successful and whether an increased intensity has an effect (beam damage, charging) on the valence band spectra, measurements were made on CIS and CdS using Mg Kα and monochromatic synchrotron radiation at 1253.6 eV. The experiments were done in succession on the same samples and the results are shown in fig. 52.

Starting with the CIS samples on the left side of fig. 52, the spectra have the same valence band edge, 0.60 eV, although the shape of the edge is somewhat different, the difference being due to the different resolutions of the two excitation sources. The higher resolution, therefore, makes the peak leading into the valence band edge on the left side of both CIS spectra, at 2 eV, sharper in the Mg Kα spectrum. Furthermore, a linear extrapolation (not shown) of these spectra resulted in a valence band edge position of 0.00 eV for the CIS measured with Mg Kα and -0.25 eV above the Fermi Level for the synchrotron spectrum, the difference being, again, due to the higher resolution of Mg Kα causing less smearing of the edge. The difference in results of both linear extrapolations and the implication of a highly p-doped CIS surface or even a metallic CIS surface, which would shunt the solar cell if it were real, supports the use of the convolved fits which result in the same value for the valence band edge in each spectrum.

With the CdS (the right side of fig. 52), the situation is more complicated. The fits result in slightly different valence band edge positions, 1.40 eV for the Mg Kα measurement and 1.25 eV for the synchrotron measurement, although the discrepancy is within the margin of error of the measurement. This time, however, the synchrotron measurement seems to have the sharper feature at 2.50 eV. One reason for this could be the subtraction of the satellites. The intensities of the valence bands with Mg Kα radiation are very low with a rather low signal-to-noise ratio. It is therefore possible that satellite removal does not uniformly effect the spectrum. However, if we again consider the linear extrapolation (not shown), the Mg Kα spectrum results in a valence band edge 0.8 eV below the Fermi Level, while the value for the synchrotron measurement is 0.35 eV. Not only can

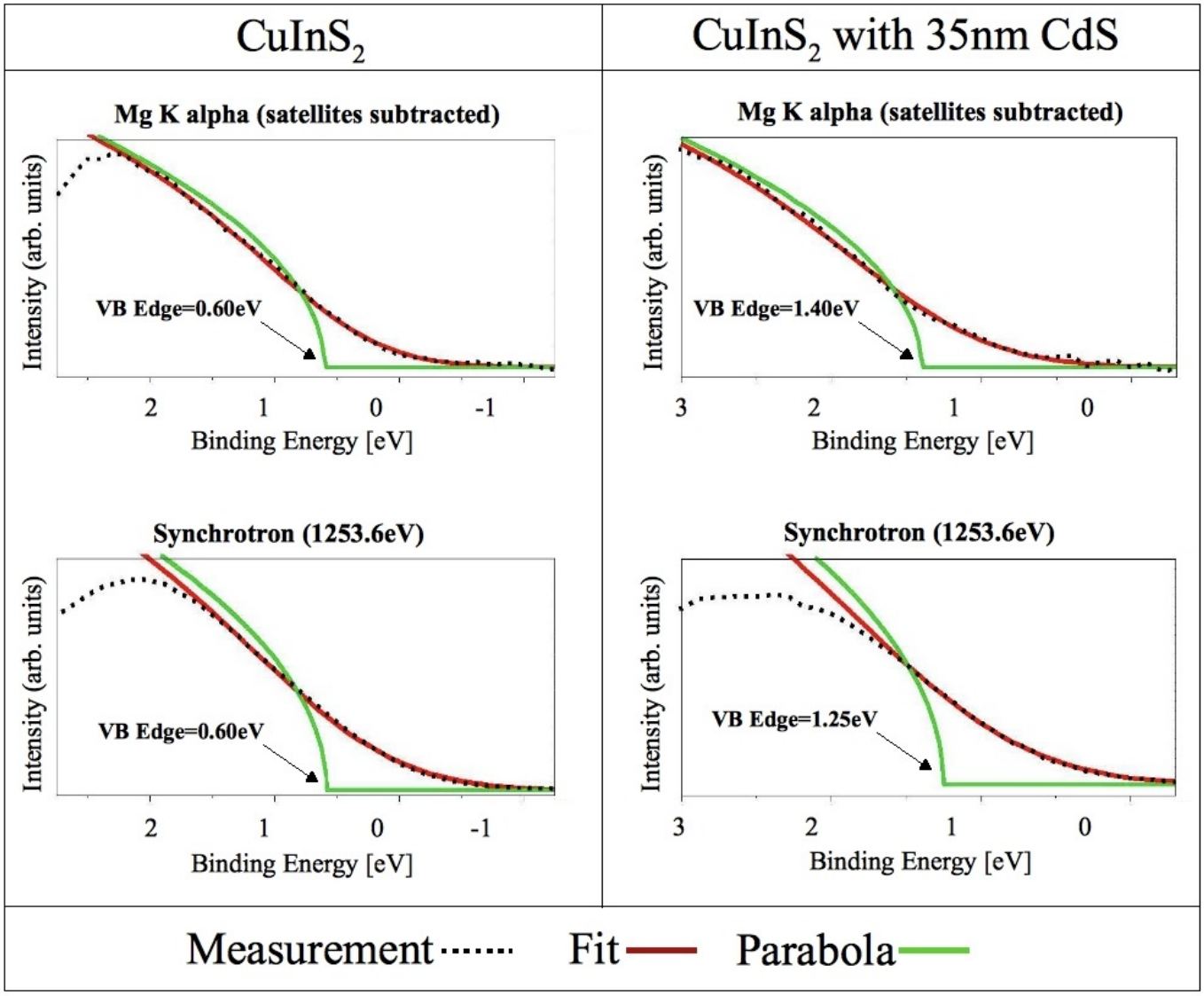


Figure 52: A comparison of the CIS and CdS valence band edges measured with Mg Kα and synchrotron (1253.6 eV) radiation and fitted using a parabola broadened with a Gauss distribution. While the values for the valence band of CIS are the same, a difference is seen between the CdS measurements.

the difference in these two values not be rectified with the error in the measurement, but they also imply p-doped CdS. This would imply, in the extreme case, a conduction band offset of zero between the CIS and CdS, but more likely a spike, which contradicts measurements made of $E_{g,eff}$ and measured values of V_{oc} (see chapter 6). However, the fact that the synchrotron measurement is indeed more smeared than the Mg Kα measurement due to lower resolution can again be seen with the values of the linear extrapolation.

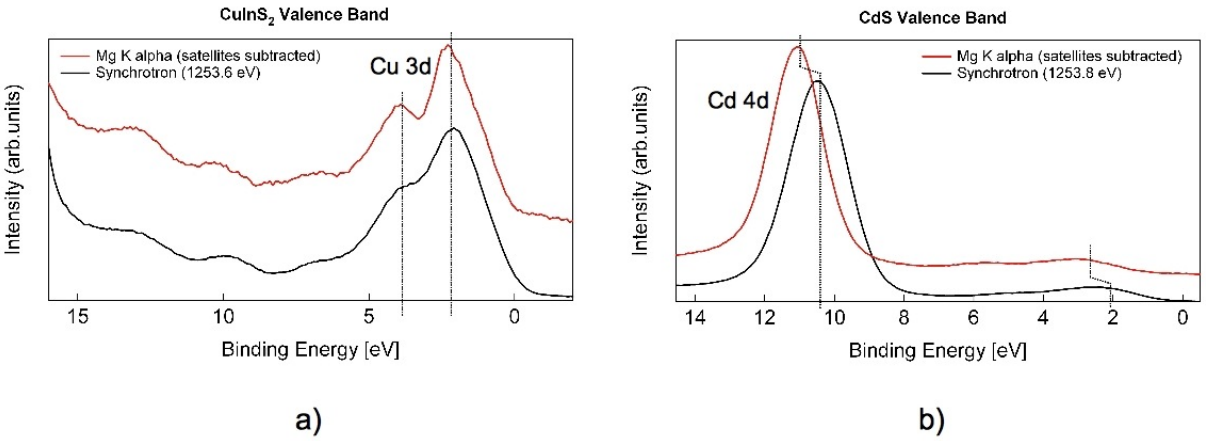


Figure 53: A comparison of the valence bands of CIS and CdS measured with Mg Kα (satellites subtracted) and synchrotron (1253.6 eV) radiation. The higher resolution of Mg Kα is evident as is a shift in the CdS bands when measured with Mg Kα and synchrotron radiation. The parallel shift of the bands points to charging of the sample.

If we turn to fig. 53, the entire upper valence band is presented for a) CIS and b) CdS. In the CIS spectra one sees immediately that the resolution using Mg Kα is indeed better: the double Cu 3d structure at 2-3 eV comprising the valence band edge is much more smeared out in the synchrotron measurement. A slight shift may also present, as can also be seen in the Cu 3d feature, which may be due to slight differences in the Au calibrations. However, some features seem to be at exactly the same position. The "shift" may therefore be due to the low signal-to-noise ratio of the Mg Kα spectrum augmenting some features' true shape. The high intensity of the synchrotron is also easily seen as both measurements contain 40 scans. This explains the smoother appearance of the synchrotron measurement, along with the fact that the lower resolution will also make a spectrum appear smoother.

Fig. 53 b) shows a similar comparison, this time for CdS. Apart from the same differences in signal-to-noise ratio as mentioned for part a), it can be seen here that the shapes of the valence bands are essentially the same, but the spectra are shifted relative to one another. This is most visible on the crest immediately preceding the valence band edge at 3 eV and on the positions of the Cd 4d core level at 11 eV.

The parallel shift in the entire band leads to the conclusion that charging is the clarification for the difference in band positions between the Mg and synchrotron measurements; beam damage would have resulted in a band of differing appearance. There may also

be a small shift due to the different Fermi Level calibrations. This shift clarifies in part the 0.15 eV difference in the fitted valence band edges in fig. 52, however, the shift seen here is 0.60 eV and actually over compensates for the discrepancy. It is possible that the satellite subtraction at the valence band edge once again comes into play here and has masked part of the 0.60 eV shift seen in the rest of the band. This shift will be seen again in the next section and the discussion will be completed at that point.

Despite the small discrepancies between the Mg Kα and synchrotron spectra and the effects of satellite subtraction, the next experiments compare spectra measured with He I and He II to those measured with Mg Kα. However, the differences seen between the UPS and Mg Kα spectra far outweigh those seen between Mg Kα and synchrotron and help to shed light on the discrepancies already seen.

8.3.3 Mg Kα and Ultraviolet Radiation

As mentioned before, the results shown here using different radiation sources are from the same samples. However, the samples used differ from those used above in sec. 8.3.2 and results should not be compared.

Beginning again with the valence band edges, fig. 54 compares the difference between spectra measured with UPS (He I, He II) and Mg Kα radiation for CIS and CdS, the He I and II spectra having, as usual, an error of $\pm$100 eV.

The left side of fig. 54 again contains the CIS spectra. The He I and II spectra here both have a valence band edge at 0.80 eV while the Mg Kα edge is very similar, lying at 0.75 eV. The linear extrapolation of the Mg Kα curve results in a situation similar to that discussed in sec. 8.3.2.

The measurements on CdS represent, as above, a more complicated situation. The position of the valence band edge is at 2.00 eV for He I and He II, but at 1.20 eV for Mg Kα. This is a very large difference of 0.80 eV, far outside the range of the error. And in this case, as well, a linear extrapolation of the CdS valence band edge measured with Mg Kα would only exacerbate this discrepancy.

As in sec. 8.3.2, one can find an explanation for the differences in valence band edges, especially in the case of the CdS, in fig. 55, where the entire valence bands of CIS and CdS measured with He I, He II and Mg Kα radiation are shown.

Fig. 55 a) compares the different measurements on CIS. The position of the In 4d core level is immediately seen to be at different binding energies when comparing the He II and Mg Kα spectra.[30] The difference in energy is 0.25 eV, which is more than the 0.05 eV separating the valence band edges. The shifts are, however, in the same direction, pointing again to small charging effects in the case of the Mg measurement. The difference between the two shifts could be due to the fact that the position of the In 4d peak in the He II spectrum is influenced by the secondary electron cutoff creating a difficult background for

[30] The He I excitation energy at 21.2 eV is not high enough to excite this level into the vacuum.

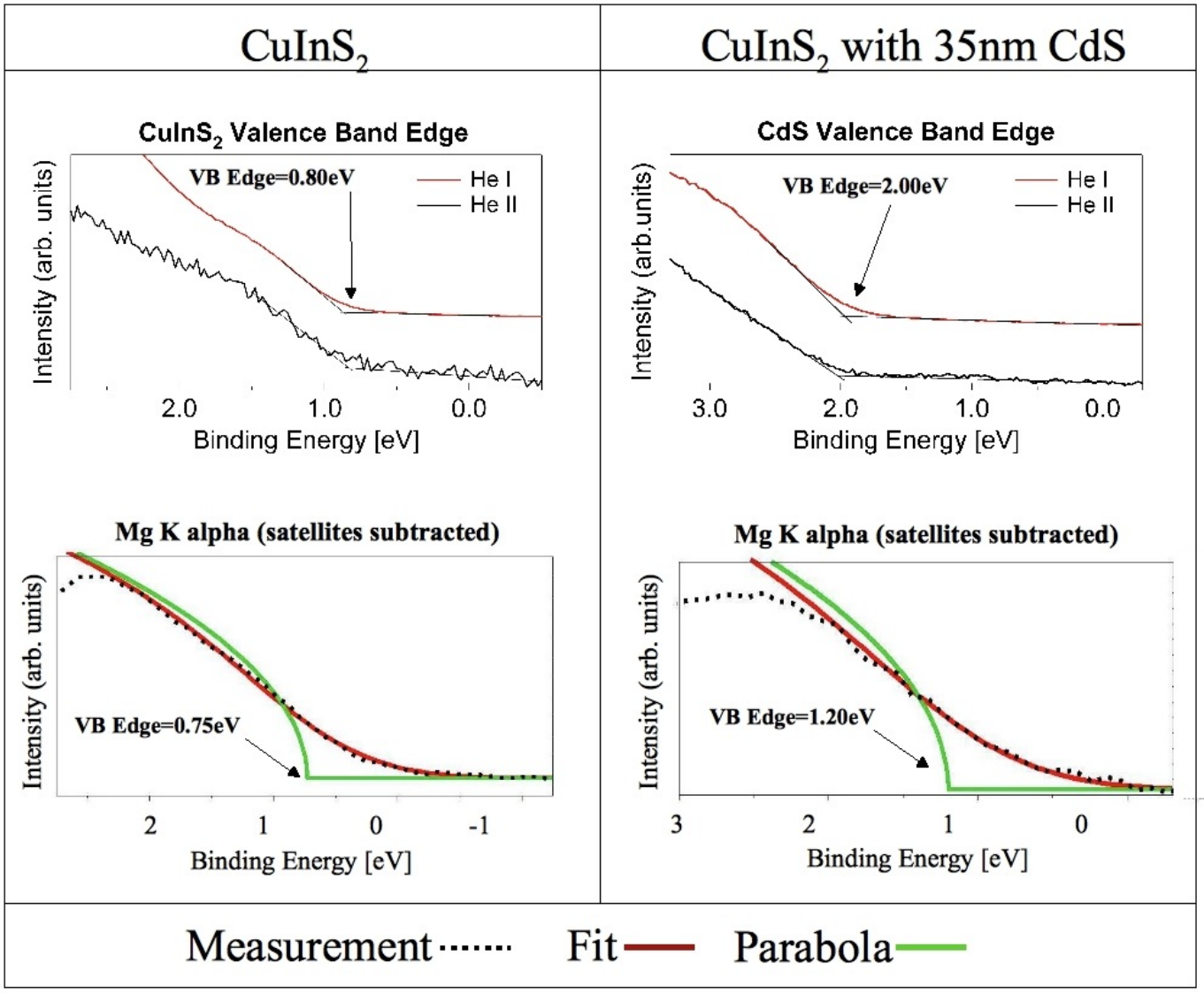


Figure 54: A comparison of the valence band edges of CIS and CdS measured with He I, He II and Mg Kα (satellites subtracted) radiation. While the position of the valence band edge of all three measurements on CIS is very similar, 0.75-0.80 eV, the CdS measurements show a drastic difference. Whereas the valence band edge for the UPS measurements is 2.00 eV, the same feature has an energy of only 1.20 eV when measured with Mg Kα radiation, resulting in a difference of 0.80 eV.

fitting or to a slight deformation of the valence band in the Mg measurement due to the core hole created by the high excitation energy.

Also, the fitting of the valence band edge, as discussed at the end of sec. 8.3.1 may contain an error due to fitting which cannot be estimated here.

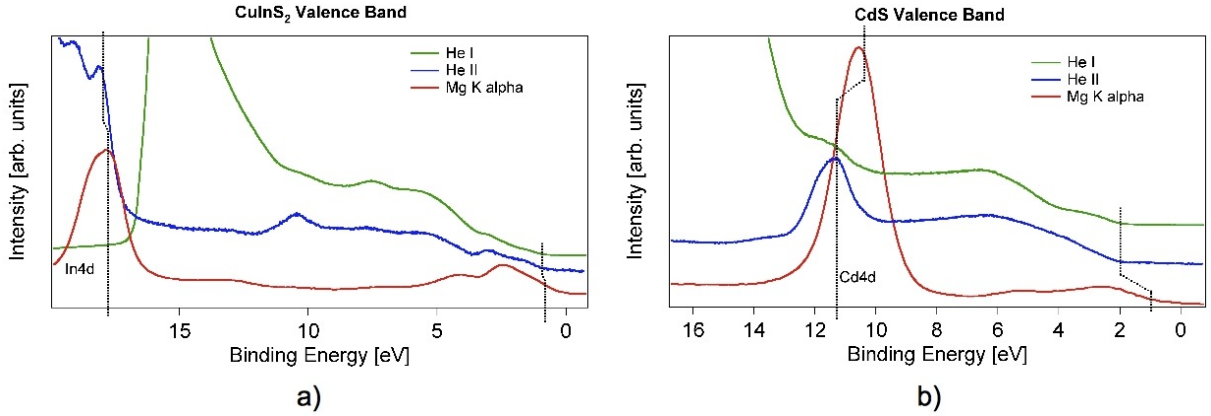


Figure 55: A comparison of the valence bands of CIS and CdS measured with He I, He II, and Mg Kα (satellites subtracted) radiation. The Mg Kα spectra from both materials are shifted compared to the He I and He II spectra, both of whose features are aligned, pointing to charging effects in both samples.

Turning to the CdS in fig. 55 b), a similar phenomenon can be found although the shifts are much larger in this case. Examining the Cd 4d core level,[31] the binding energies are shifted by 0.75 eV between the Mg and UPS experiments. This corresponds almost exactly to the shift of 0.80 eV between the valence bands showing very clearly a parallel shift of the entire CdS valence band measured with the different radiation sources. This points clearly to charging effects. Slight deformations of the bands may also be present due to the core hole present in the Mg measurement.

8.4 Surface Photovoltage

The shifts seen between Mg Kα and synchrotron measurements for the CdS and between Mg Kα and UPS measurements from both materials can be explained through reduced band bending on the CIS surface which also effects the position of the Fermi Level in the CdS [134, 135, 136].

Fig. 56 a)[32] shows the $CuInS_2$/CdS junction in thermodynamic equilibrium in the dark. The band bending in the CIS may be partly intrinsic and may be partly due to the CdS

[31] This core level can indeed be excited by He I radiation.

[32] The symbols in fig. 56 have the following meanings: $E_{v,d}$ and $E_{v,l}$ are the positions of the CdS valence band edge in the dark and under illumination, respectively. E_f^{e*} is the electron quasi Fermi Level. U_{ph} is the photovoltage. eV_d and eV_l are the amounts of band bending on the CIS surface in the dark and under illumination, whereby $eV_d - eV_l = U_{ph}$.

deposition (see chapter 5) and is caused by holes leaving the CIS surface in the former case and electrons entering the CIS surface from the CdS in the latter case. The extra negative charge on the CIS surface leads to the depletion region shown in the figure.

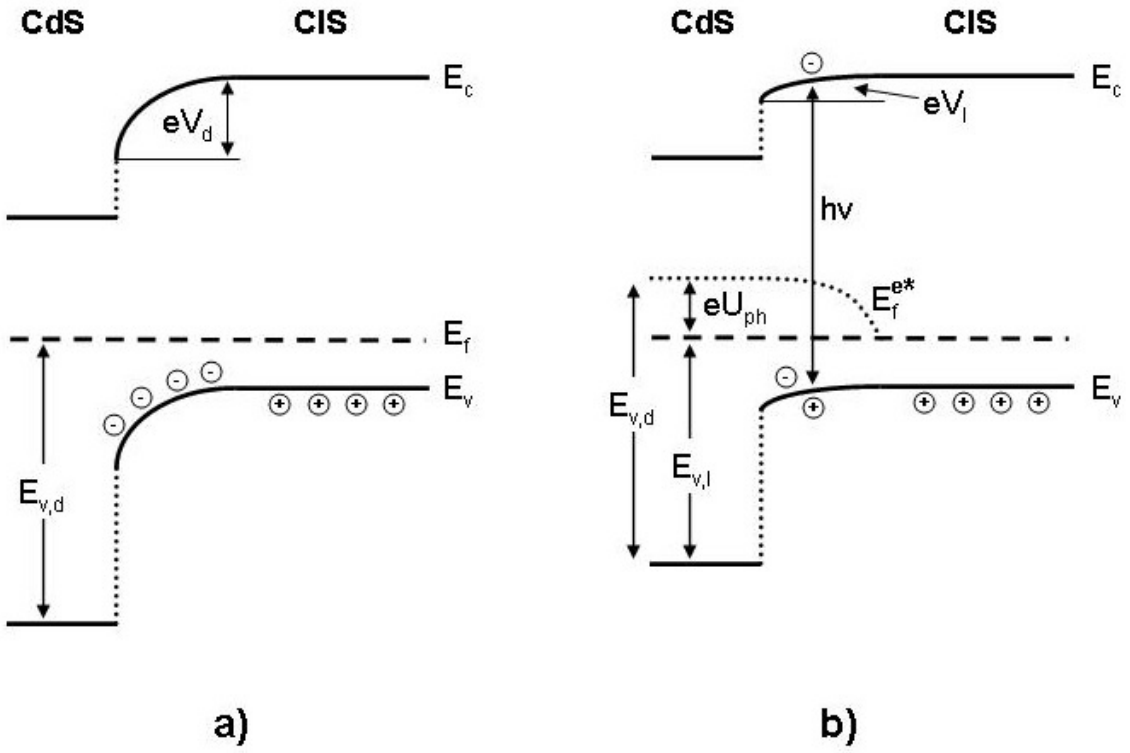


Figure 56: a) The $CuInS_2$/CdS junction in thermodynamic equilibrium in the dark and b) under illumination. The electron-hole pairs created through the absorption of the light reduce the band bending through a surface photovoltage, U_{ph}, on the CIS surface and change the position of the materials' valence band edge in relation to the Fermi Level. The additional minority carriers (electrons) cause a splitting of the Fermi Level shown by the quasi-Fermi Level for the electrons E_f^{e*}. Charges shown inside the band gap are fixed charges while those in the bands are mobile.

Under illumination the creation of electron-hole pairs through light absorption ($h\nu \geq E_g$) causes the presence of more holes in the valence band which compensate the negative charge and reduce the band bending. At the same time, the non-eqilibrium state leads to a splitting of the Fermi Level into a quasi-Fermi Level for the electrons, E_f^{e*}, and for the holes, $E_f^{h^+*}$. Because the material is p-type, the additional hole population will not cause $E_f^{h^+*}$ to split off from the equilibrium Fermi Level, E_f.

The change on the CIS surface leads directly to a corresponding change in the CdS. Because the CdS layer is so thin, the position of the Fermi Level on the CIS surface will be carried through to the surface of the CdS. This is similar to the CdS deposition-induced band bending discussed in chapter 5 but moves the Fermi Level in the opposite direction.

The measured valence band edge is, therefore, closer to the Fermi Level in the measure-

ments where the exposure to X-ray light causes a surface photovoltage (SPV), U_{ph}.

An analogue view of this is sample charging. A poorly contacted sample will become positively charged because the continuous loss of electrons through photoionization of the atoms cannot be compensated by outside charge entering the sample. This will lead to a measured increase in the binding energies of all spectral features because it will be more difficult for an electron to leave the sample. The reverse scenario, that the perceived binding energies of the spectral features decrease, would then be due to an excess of negative charge in the sample. As can be seen in fig. 56, while the holes produced through photon absorption can diffuse to the back contact, the electrons will collect at the sample surface causing the charging. The number of electrons will increase until the recombination rate equals the electron-hole production rate.

The SPV was always larger in CIS when CdS had been deposited on the surface. This can be explained through the band diagram in fig. 56. If the photo-generated electrons diffuse into the CdS they will be more difficult to conduct away than from the sample surface because of the step in the conduction band which now becomes a spike if they are to leave the CdS. Furthermore, the poor conductivity of CdS would exacerbate the problem.

8.5 Conclusion: Valence Band Form

Valence bands and valence band edges measured with Mg Kα, synchrotron (1253.6 eV), He I and He II radiation were investigated to determine the effects of the different excitation energy sources. UPS measurements were analyzed using the linear extrapolation method while XPS spectra were fitted with a parabolic density of states broadened with a Gauss distribution determined from fits made on Fermi Level spectra also measured with XPS. The convolved fits of XPS measurements were in some cases able to compensate for the discrepancies seen in the valence band spectra measured with different excitation energy sources although the shifts in valence band edges were not always equal to those observed in the corresponding core levels. An accurate determination of the valence band edge should move in parallel with the core levels in cases where charging or band bending account for the observed shifts. However, the convolved parabolic density of states fits were more realistic than applying a linear fit to the XPS measurements.

Mg Kα and synchrotron measurements on CIS had very similar results. Both valence band edges lay at 0.60 eV below the Fermi Level, the convolved fit being able to compensate for the increased broadening from the synchrotron radiation and no shift was seen in the core levels. With the CdS there was a small discrepancy between the Mg Kα and synchrotron measurements. The valence band edge measured with Mg Kα was at 1.40 eV while the synchrotron measurement resulted in 1.25 eV. A Cd 4d core level shift of 0.60 eV due to an increased surface photovoltage (SPV) in the synchrotron measurement over compensated for the difference in valence band edges.

These shifts were more clearly seen when comparing Mg Kα measurements with those made with UPS (He I, He II). Both UPS measurements resulted in a valence band edge

0.80 eV below the Fermi Level for CIS, while the valence band edge lay at 0.75 eV in the Mg Kα measurement. Although the convolved fit for the latter measurement resulted in a similar energy of the valence band edge for all three excitation sources, an observation of the In 4d core levels showed a shift of 0.25 eV which over compensated for the differences in the valence band edges.

The Mg Kα and UPS measurements on CdS showed a very large shift in the valence band edges. While the UPS measurements both resulted in a valence band edge 2.00 eV below the Fermi Level, the position determined with Mg Kα was 1.20 eV, the convolved fit not being able to compensate for the difference in edge position. However, an observation of the Cd 4d core levels resulted in a shift of 0.75 eV due to the increased SPV in the Mg Kα measurement. The convolved fit combined with the observation of an increased SPV was able to totally compensate for the differences seen between the UPS and Mg Kα measurements.

Apart from the differences in surface photovoltage seen between spectra measured with the individual excitation energy sources, other factors also made the determination of an absolute valence band energy difficult. The fitting of the Fermi Level was affected by an increased broadening from the Au 5d and 6s electrons. This problem proliferated itself when moving to the XPS valence band edges because broadening due to spectral features near the valence band edge is also possible, although to a different extent than with the Fermi Level measurements. This surely resulted in a small error of the position of the valence band edge measured with XPS, although the magnitude of the error cannot be estimated without further investigation. In addition, a distortion of the valence bands through the presence of a core hole in the XPS measurements may also effect the results.

9 Conclusion

9.1 Summary

The goal of this thesis was to investigate the role of Cd and Ga in the Cu(In,Ga)S_2/CdS interface as a heterojunction and as a component of the thin layer solar cell with the structure Glass/Mo/Cu(In,Ga)S_2/CdS/i-ZnO/n^+-ZnO. The importance of this junction stems from the consistently high solar cell efficiencies achievable with the CdS buffer on all Cu(In,Ga)(S,Se)$_2$ absorbers which regularly top the efficiencies of cells with alternative buffers, especially in large-scale production settings. However, a basic understanding of the CdS buffer's function and, thus, its superiority demands further investigation.

The work presented here approaches this task in essentially two steps. The first was an investigation of the formation of the junction and which chemical and electronic characteristics are influenced by the formation process. In the second step, after junction formation, the electronic positions of the valence and conduction bands were investigated on each side of the junction to examine the influence this junction has on the electronic properties of the solar cell.

In addition, the success of the second step depended on the application or fundamental investigation of experimental methods which have only recently been employed for analysis of the Cu(In,Ga)S_2/CdS system and are not yet fully understood. For the valence bands this was near-UV constant final state yield spectroscopy (CFS) and for the conduction bands Near Edge X-Ray Absorption Fine Structure (NEXAFS). Detailed analysis of the merits of both methods has shown that they can be valuable tools for the investigation of surfaces of single materials and also of junctions formed from these materials.

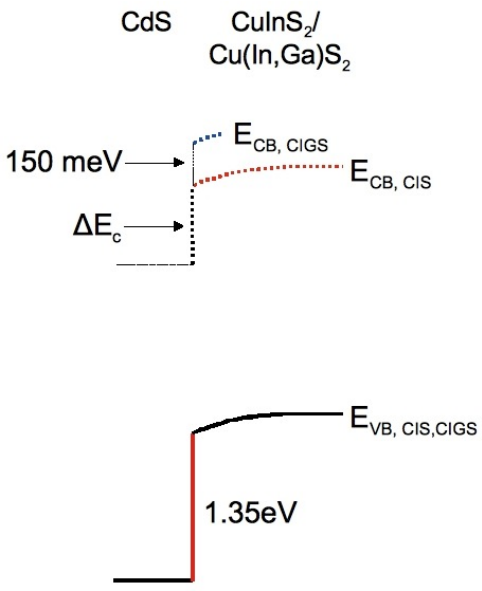


Figure 57: The $CuInS_2$/CdS and Cu(In,Ga)S_2/CdS junctions as determined from the results of this work and explained in the text.

For reference, fig. 57 shows several of the results discussed here. The displayed value for the valence band offset is a mean value from all of the measurements done and the position of the CIGS conduction band is meant to be for the surface of the absorber only and does not, therefore, extend into the bulk. The Fermi Level has not been included to emphasize the different measured positions of E_f in the junction in different samples after CdS deposition.

It has been proffered that the CdS buffer layer could have several different roles in the solar cell. These include improved band alignment and/or lattice matching between the CIS and the window layer and passivation of the CIS surface. More specific to the role of

the Cd, it may stay on the CIGS surface and pin the Fermi Level at an electronic position vital to the functionality of the solar cell or it may diffuse into the absorber and act as a donor. Because the Cd enters the system during chemical bath deposition of CdS on CIS, the role of the Cd was the subject of the first step of the investigation. The deposition of a full CdS buffer also creates a Cd-containing layer ($CuInS_2$:Cd) on the CIS surface which, unlike CdS, is non-soluble in HCl. Because it is thought that Cd occupies cationic sites in the CIS lattice, the Cd-S bonds in the $CuInS_2$:Cd should be different than those found in CdS. Furthermore, the Cd may indeed diffuse into the CIS absorber as this possibility could not be excluded through experiments in this work. The diffusion of Cu into the CdS layer was also observed during the deposition process, although it does not reach the surface of a full CdS buffer layer.

In spite of the junction formation process incorporating Cd into the CIS surface, no evidence was found to support Cd doping the CIS surface n-type or that the Fermi Level is pinned to a specific electronic position important for solar cell functionality after CdS deposition. After CdS was etched away from the CIS surface leaving behind the CIS:Cd layer, the electronic state of this surface was the same as that of HCl-etched CIS surfaces which had previously been etched only with potassium cyanide (KCN) without CdS deposition. A doping of the CIS surface from Cd incorporation would have shown a difference in the Fermi Level position in these samples.

When investigating the CIS/CdS junctions deriving from different CdS depositions, it was observed that the position of the Fermi Level in the junction was not reproducible. The cause of this is differing amounts of band bending on the CIS surface during the CdS deposition. The production of the same interface states able to pin the Fermi Level leads to a consistent position of the Fermi Level on the sample surface and was not observed here. The band offset between the two materials was, however, consistent in each deposition with a value of $E_{v,CIS} - E_{v,CdS}$=1.25 eV$\pm$0.20 eV. This means that the position of the Fermi Level on the CIS surface can also be calculated by the position of the Fermi Level in the CdS layer and it has been shown that the Fermi Level position in the CdS was not reproducible. The deposition of highly n-doped ZnO may then be responsible for the final amount of band bending in the different layers of the solar cell. This limits the role of the CdS layer in the $Cu(In,Ga)S_2$ solar cell to lattice matching, interface defect reduction or to optimizing the band alignment between CIGS and the window layer.

In the second step, the role of Ga was investigated after the junction was formed. Ga widens the band gap of the absorber with increased concentration thereby effecting the band alignment at the interface and leads to an increase in the open-circuit voltage, V_{oc}, of the solar cell by up to $\sim$100 meV.

The valence band offsets between CdS and three different absorbers, $CuInS_2$, $Cu(In,Ga)S_2$ ($\sim$8% surface Ga content) and $CuGaS_2$ were measured with the combined XPS/UPS method and resulted in values of $E_{v,absorber} - E_{v,CdS}$=1.25 eV$\pm$0.20 eV, 1.35 eV$\pm$0.20 eV and 1.30 eV$\pm$0.20 eV, respectively. Thus, within the error of the measurement, there was no dependence of the valence band offset on Ga content. In the case of the CIS/CdS junction, this result was confirmed through the use of near-UV CFS, a method until now used only to investigate the a-Si/c-Si heterojunction. The first application of this method

to the CIS/CdS junction allowed a direct measurement of the valence band offset at this interface and resulted in a value of 1.45 eV±0.20 eV. Although it was hoped that this method would also increase the accuracy of the band offset values, an experimental error of ±0.20 eV was achieved which is equal to the error of the combined XPS/UPS method.

In contrast to the valence band offsets, the absolute position of the CIS, CIGS and CGS valence and conduction bands were dependent on Ga concentration. While the valence band edges of $CuInS_2$ and $Cu(In,Ga)S_2$ were both at 0.70 eV below the Fermi Level, the valence band edge of $CuGaS_2$ was at 0.40 eV below the Fermi Level. In the latter case, the increased repulsion of the Cu 3d states by the S 3p states in the Cu-rich CGS surface led to the change in valence band position.

Increasing Ga concentration also led to a shift in the conduction band edge to lower binding energies between all three absorbers. Although no conclusive absolute positions could be obtained a qualitative opening of the band gap with increased Ga concentration was observed, even under consideration of the shift in valence band edges. This investigation was done using NEXAFS and although this method had already been used to investigate some kinds of $Cu(In,Ga)(S,Se)_2$ absorbers the fundamental physical restrictions of the method with regards to the CIGS system were taken into account for the first time here. The effect of band distortion due to the core hole and the fact that NEXAFS measures only a local density of states were considered and results were compared to optical and inverse PES methods to assess compatibility. In spite of these difficulties a relative, quantitative change of 150 meV±30 meV between the conduction band edges of CIS and CIGS was observed. If the conduction band edge of CdS is unaffected by the Ga content of the absorber then this result shows an exacerbation of the conduction band offset between the CIS and CdS with the addition of Ga. A first approximation using bulk band gaps showed the conduction band offset between CIS and CdS to be a step of ΔE_c ∼400 meV which results in an effective band gap, $E_{g,eff}$ of ∼1.1 eV, and can limit the open circuit voltage, V_{oc}, of the solar cell. Although the increase in conduction band offset by the measured 150 meV±30 meV with the addition of Ga would not be expected to lower V_{oc} because E_{eff} at the interface remains unchanged, it would not be expected to increase it, either. Yet, this is exactly what is observed: the addition of Ga raises V_{oc} by ∼100 meV.

What is the reason for this change? Although the CdS may act to improve lattice matching and band alignment between the CIS and the window layer, these are not further optimized by the addition of Ga because an ∼8% addition of Ga will not effect the lattice parameters to a large extent and the band alignment between the two materials becomes worse. This means that the addition of Ga must reduce the defect density on the CIGS surface or that defects present on the CIGS surface are more easily passivated with the application of a buffer layer. Another possibility is that the role of a solar cell's $E_{g,eff}$ is not as central to the functioning of the cell as previously thought. For instance, if the splitting of the quasi-Fermi Levels could be increased by the larger band gap of CIGS and is not limited by $E_{g,eff}$, then this could be a source of the increase in V_{oc}.

9.2 Outlook

Further work on this junction should be centered on obtaining absolute values for the surface positions of the conduction bands of CIS, CIGS, CGS and CdS. This non-trivial act would eliminate the reliance on bulk band gap values which is a large source of uncertainty about band alignment.

This can begin by building on the experiments presented here. The fundamental problems of the core hole effects and LDOS-sensitivity of the NEXAFS measurements need to be further investigated and better understood, possibly with theoretical models, in order to obtain absolute quantitative results. The physical interpretation of measurements, i.e. how the system reacts to the excitation needed to perform them, especially when considering conduction band edges, must be more thoroughly debated instead simply piping more and more samples through methods we do not fully understand.

The CFS measurements should be repeated and also performed on CIGS/CdS junctions in order to further investigate the difficulties encountered here and to expand results. Higher excitation energies able to probe the CdS valence band edge would make this an invaluable tool for the characterization of chalcopyrite absorber/buffer junctions. In the case of IPES, effects of charging and damage from the electron beam must be more closely scrutinized. IPES values are very scattered in literature and even from experiment to experiment. Perhaps more progress would be made by investigating well-understood model systems instead of systems such as $Cu(In,Ga)S_2$ absorbers used here. For example, epitaxial CIGS layers with no surface band bending could be measured and results compared to optical measurements of the band gap.

The study of the diffusion of Cd into the CIS during CBD is also of central importance. The depth to which Cd diffuses and the lattice positions occupied by Cd in the CIS may be vital to understanding the role of Cd in this junction. Most of the results in this thesis focused on what the Cd *does not* do when the real information sought is what the Cd *does* do. Thus, experiments with sensitivity to the chemical environment of specific atoms, such as NEXAFS, should be performed on samples where the possibility of measuring a surface CdS layer can be excluded. Even the experiments done here with CIS:Cd where no Cd signal was obtained should be repeated with more sensitive detectors or with longer measurement times because weak signals can easily be lost due to low signal-to-noise ratios.

The conclusion that Cd has no effect on the electronics of the CIS surface seems too simple, especially when one considers that the valency of Cd is different from the other cations in the system. It would be very surprising if the incorporation of this atom into the CIS lattice had no effect on the electronic properties of the resulting phase. It could be that the effect of the incorporated Cd was compensated in some way, which leads again to the necessity of understanding exactly how the Cd dopes the CIS.

And finally, another common way to investigate junction characteristics is with experiments involving charge transport characteristics through the junction. These include current-voltage and voltage-capacitance measurements and although some of these ex-

periments for this system can also be found in literature, none were attempted here. However, the correlation of these experiments with those involving photoelectron spectroscopy would be very interesting, especially when done on the same samples in order to avoid the problem of non-reproducibility. The ability of PES to investigate interfaces stops when the thickness of the top layer being deposited on the substrate (in this case the CdS) extends past the information depth of the specific PES method used. Charge transport experiments do not suffer from this. On the other hand the results of transport experiments are not limited to the interface only but are influenced by the entirety of the material on either side of the junction, that is, by the entire sample. And to disentangle the bulk effects from the interface effects is another challenge.

Appendices

A Raw Data for measured [Cu]/[In] Ratios During HCl etching

This appendix is a supplement to sec. 5.1.2.1 and shows the In $3d_{5/2}$ and Cu $2p_{3/2}$ core levels used to calculate the [Cu]/[In] ratio in fig. 21 after 6, 9 and 12 sec of etch time in HCl.

Because the measurements made after 3 sec of etch time showed neither a Cu nor an In signal, it is shown here that the peaks used for the first three points in fig. 21 at 6, 9 and 12 sec are indeed of a quality suited for fitting.

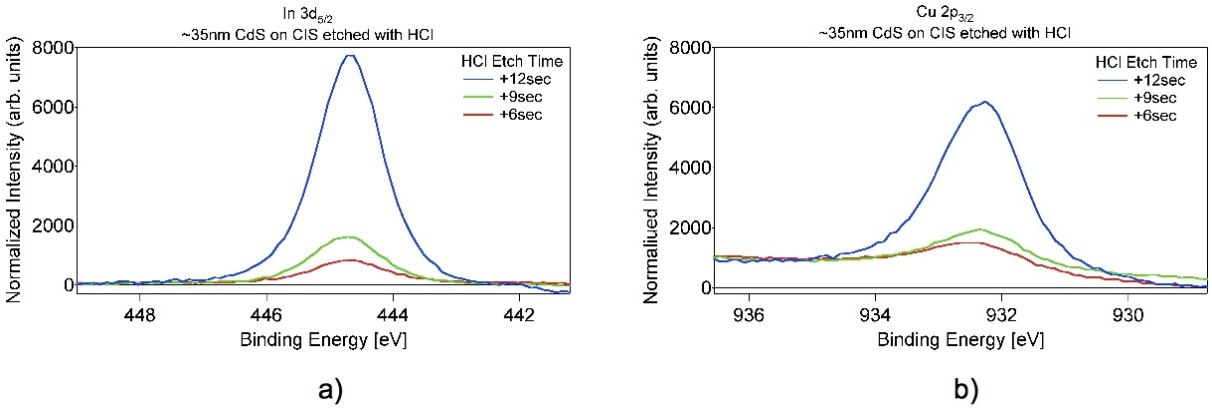


Figure 58: a) In $3d_{5/2}$ and b) Cu $2p_{3/2}$ core levels used to calculate the [Cu]/[In] ratio in fig. 21 after 6, 9 and 12 sec of etch time in HCl. The peaks have been normalized only by the number of scans used to make the individual measurements.

Fig. 58 shows a) the In $3d_{5/2}$ and b) Cu $2p_{3/2}$ core levels as measured. The peaks have been normalized only by the number of scans used during the measurement making their relative areas (and changes in the areas) directly accessible. The number of scans used for the In peaks was 22, 12 and 7 scans for 6, 9 and 12 sec of etch time, respectively while for the same times the number of scans for Cu was 30, 30 and 12, respectively.

Although it is somewhat difficult to see in the Cu measurements because of the differing backgrounds between 6 sec and 9 sec, the areas of these two peaks are relatively similar while the corresponding In peaks differ by a greater amount and is reflected in the changing [Cu]/[In] ratio in fig. 21. After 12 sec of etch time the difference is also noticeable.

B XPS investigation of HCl-etched CIS after CdS deposition: Al Kα versus Mg Kα Excitation Energies

This appendix is a supplement to sec. 5.1.2.1.

After two HCl etch steps, at 21 and 153 seconds, the CIS sample with the CIS:Cd layer was measured with Al Kα radiation in addition to Mg Kα radiation in order to take advantage of the two different information depths offered by the respective excitation energies. If indeed the Cd was limited to the surface or a near-surface region of the absorber, it may be possible to detect a difference in the concentration ratios because a larger volume of Cd-free material can be measured with Al Kα than with Mg Kα.

At 21 seconds, the ratios involving Cd had values of [Cd]/[Cu]=0.26 and [Cd]/[In]=0.09 when measured with Mg Kα while the values measured with Al Kα were [Cd]/[Cu]=0.13 and [Cd]/[In]=0.11.

At 153 seconds, the same ratios had values of [Cd]/[Cu]=0.11 and [Cd]/[In]=0.04 when measured with Mg Kα and [Cd]/[Cu]=0.08 and [Cd]/[In]=0.04 when measured with Al Kα.

Therefore, in both cases the [Cd]/[Cu] ratio decreased with the higher excitation energy while the [Cd]/[In] signal stayed the same or increased very slightly. While it may be plausible to interpret this as being due to a layer of CIS:Cd thinner than, or whose concentration is changing rapidly compared to the information depth of Al Kα (3-4 nm), it is unlikely for two reasons.

Because the information depth of In is higher than that of Cu due to the lower binding energy and thus higher resulting kinetic energy of In 3d electrons, any change in a thin CIS:Cd layer would likely be more pronounced in the [Cd]/[In] ratio. Also, when one looks at the [Cu]/[In] ratios measured with Mg Kα and Al Kα radiation, they are seen to be higher for the Al measurement at both times, 21 and 153 seconds.[33] Thus the [Cd]/[Cu] ratio may decrease due to an increase in Cu concentration rather than a decrease in Cd concentration with depth.

However, the values of the [Cd]/[Cu] and [Cd]/[In] ratios are too small to be viewed with any matter of accuracy and the changes observed between the ratios with the two different excitation energies are even smaller. The results of this experiment are, thus, inconclusive.

[33] The values are $[Cu]/[In]_{21,Mg}$=0.35, $[Cu]/[In]_{21,Al}$=0.84, $[Cu]/[In]_{153,Al}$=0.36, $[Cu]/[In]_{153,Al}$=0.5.

C Details of the Density Functional Calculation of Cd in CIS

This appendix is a supplement to sec. 5.2.

The significant factors influencing band bending at the CIS/CdS junction are various types of chemical disorder, in particular, penetration of Cd into the CIS absorber. Therefore, in this first-principles calculation the random substitution of Cu atoms (on their regular lattice positions in CIS) by Cd atoms is studied. Assuming that the penetration length of the Cd into the CIS is longer than the typical CIS lattice parameter[34] the electronic properties at each point of the concentration profile have been considered *locally*, i.e. based on the bulk calculation for the corresponding concentrations. To account for the random chemcical disorder the so-called Coherent Potential Approximation (CPA) [137, 138] was used which delivers the best local solution (without information about the short local order) which is most successful in the case of equirandom solutions. Since the implementation of the CPA theory is naturally formulated in the Green's Function language, the CFT-based KKR (Korringa-Kohn-Rostocker) method was used within the SPR-KKR Munich code [139]. The exchange-correlation potential is treated with the standard Local Density Approximation (LDA) using the Vosko-Wilk-Nusair parameterization [140].

Because the amount of Cd needed to switch from p- to n-type CIS should be rather small (within a few percent), we stay with the experimental CIS lattice parameters for the entire range of Cd-Cu concentrations. The basic information needed from the calculation is the density of states (DOS) in the vicinity of the Fermi energy.[35] This allows us to determine the band gap size and the position of the chemical potential.[36] The latter can be determined from the equality for T≠0:

$$\int_{E_{\mathrm{VB}}}^{E_{\mathrm{VT}}} n(E)\left(1-f_{\mu,T}(E)\right)dE \;=\; \int_{E_{\mathrm{CB}}}^{E_{\mathrm{CT}}} n(E) f_{\mu,T}(E) dE$$

where $n(E)$ and $f_{\mu,T}$ are the ground state DOS and Fermi-Dirac distribution for the given temperature T, respectively, and μ is the chemical potential. $E_{\mathrm{VB,VT,CB,CT}}$ are the bottom and top of the valence band, and the bottom and top of the conduction band, respectively. For the relatively small temperatures ($T < 300\mathrm{K}$), the integration limits are well confined within a few eV around the Fermi energy.

[34] This assumption is made although the HIKE measurements in sec. 5.1.3 allowed for diffusion of Cd up to ∼1 nm into the CIS and the lattice parameter for CIS is a=5.52 Å. Higher diffusion lengths were not considered. The "undetectable" Cd discussed in the same section may diffuse deeper into the absorber.

[35] The Fermi energy refers to the highest occupied state which is called the valence band edge in the rest of the thesis.

[36] The chemical potential refers to what is called the "Fermi Level" in the rest of the thesis.

D Logarithmic Analysis of the CIS/CdS Valence Band Offset: Inconclusive Measurements

This appendix is a supplement to sec. 6.3 and considers the two samples discussed in that section which did not lead to a successful analysis of the band offsets.

In sec. 6.3, the two samples with the thinnest CdS layers (40 seconds, 1 minute) failed to give reliable results for the band offset. In both cases, the reasons are the same: the linear extrapolation was not possible and the logarithmic fit gave a questionably low value for the valence band offset.

The first problem is shown in fig. 59, where the absence of a linear region for fitting can be seen. The regions (intensities) shown were chosen in the same way the region of fig. 32 b) was chosen: the downsized version of fig. 30 b) in the logarithmic analyses of each sample gives the respective intensity of the valence band edge for that measurement. The reduction in intensity for each measurement is, as in fig. 30 b), reasonable for over layers of the respective thicknesses.

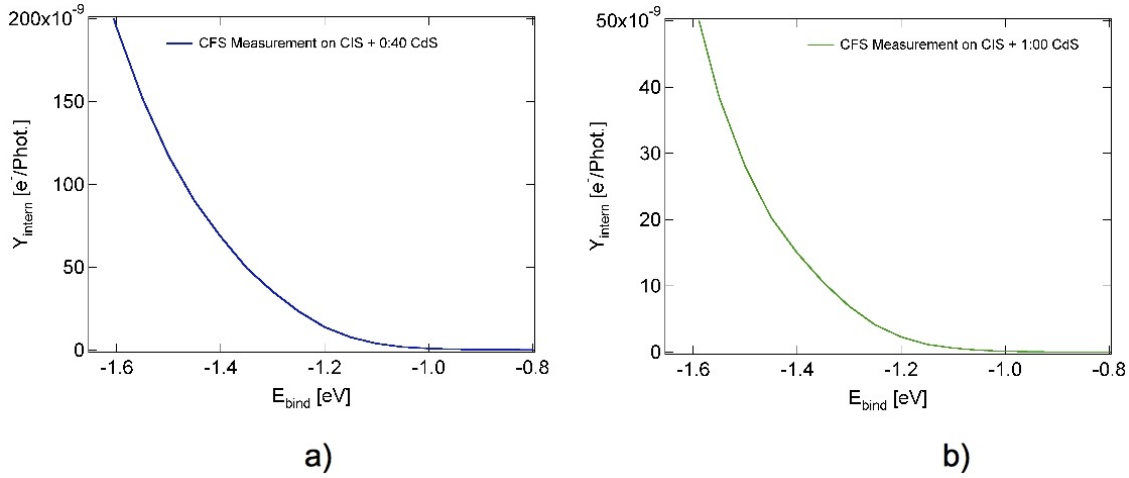


Figure 59: The CFS valence band measurements on CIS covered with a) 40 seconds and b) 1:00 minute of CdS. Neither measurement has a linear portion suitable for fitting at the intensity expected for the valence band edge.

Another possible reason for these washed-out band edges other than that given in sec. 6.3 is also based on the high information depth of CFS. These two samples possibly have regions of CIS not covered by CdS and these regions may have slightly different Fermi-Level positions than the regions covered by CdS. Because the CFS measurement averages the position of the Fermi-Level over the entirety of the illuminated part of the sample ($\sim$1cm^2), the high information depth of CFS making the Fermi-Level in the entire region measurable, the measurements in these two cases may be composed of signals from the CIS with quite different Fermi-Level positions (compare before and after the CdS deposition, fig. 31). Zooming in or out on these spectra, one finds that the curvature seen at this intensity does not disappear, although it seems that at higher binding energies, the

curve may indeed flatten. However, it does not.

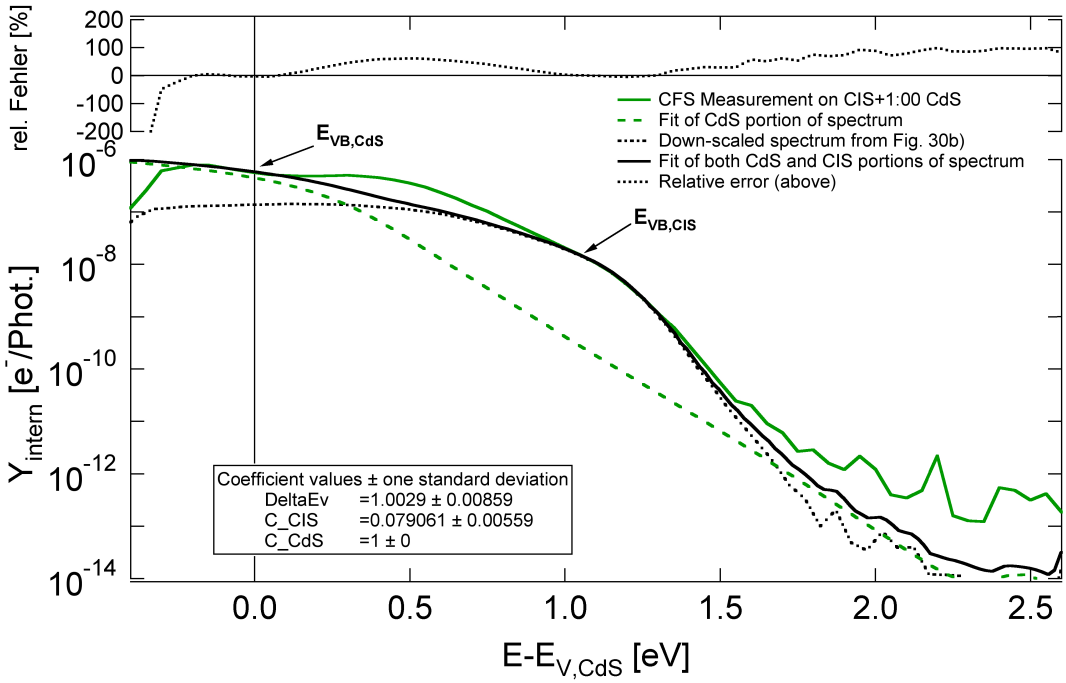


Figure 60: Logarithmic plot of the CIS sample with 1:00 minutes of CdS deposition. This is the same plot found in fig. 59 b). The band offset determined through the logarithmic investigation was 1.00 eV±0.20 eV. See explanation in text in sec. 6.3

In addition, it can be seen that the two spectra in fig. 59 have very similar energetic positions, supporting the findings found earlier, that any band bending caused in the CIS from the CdS deposition comes in the first 40 seconds of the CBD and remains static from then on.

Seeing as the CFS measurement as well as the XPS/UPS measurement of the CIS with 4 minutes of CdS showed the CIS valence band edge at about 1.1 eV, it would not be far fetched to expect the valence band edge of the other two samples to also be at about 1.1 eV. And indeed, when observing fig. 59, a band edge at 1.1 eV is entirely imaginable as the measurements do seem to approach zero around this value.

On the other hand, when looking at the failed logarithmic plot in fig. 60, the result is seen to be a band offset of about 1 eV. This would mean, however, after taking the CdS valence band edge at about 2.45 eV into account, that the CIS valence band edge would have to lie at about 1.45 eV. When looking at fig. 59 b), it can be seen that this is not the case.

It seems unlikely that the absence of the linear portion of fig. 59 b), would cause the fit in fig. 60 to shift by ∼0.40 eV. However, if this is not the case, it would mean that there are two separate causes contributing to the failure the measurement to produce a reliable,

consistent result. This also does not seem likely.

It can, however, be seen in fig. 61 that the shoulder into which the CFS spectrum from fig. 30 b) is fitted at 1.20 eV for the 40 second and 1:00 minute CdS samples (marked with arrows) is clearly shifted to the left of the same, yet broader feature at 1.35 eV in the spectrum for the 4:00 minute sample (also marked with an arrow).

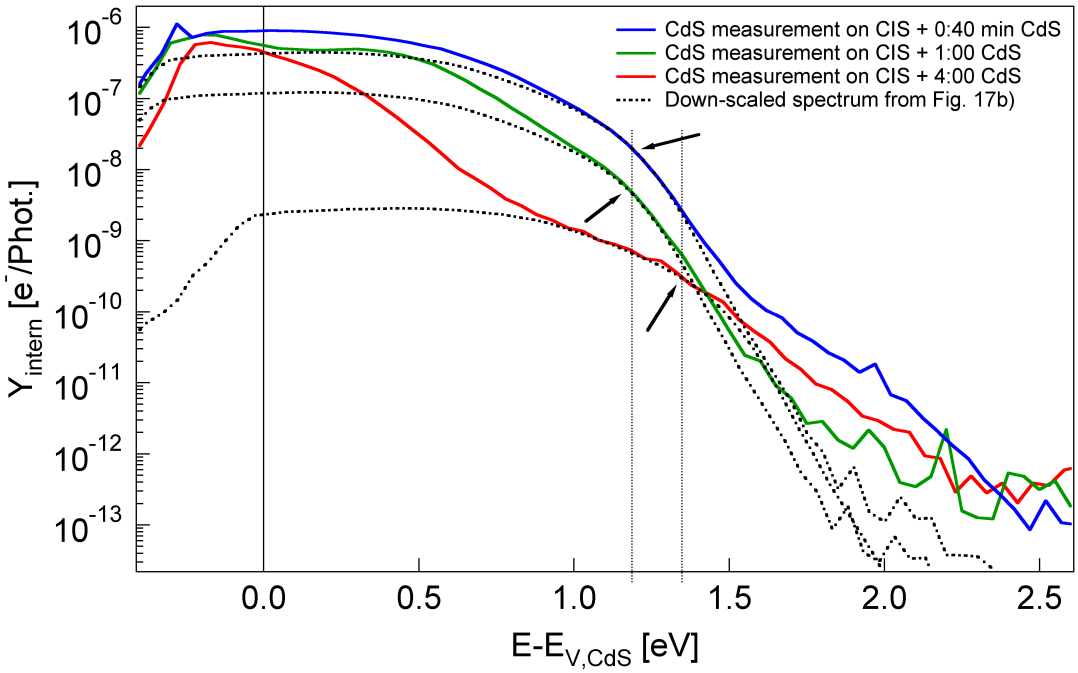


Figure 61: Logarithmic CFS plots of CIS with 40 sec, 1:00 min and 4:00 min of CdS deposition. The samples with the 40 sec and 1:00 CdS layers led to anomalous band offset values while the result from the sample with the 4:00 CdS layer was in agreement with the combined XPS/UPS method and literature values. The shoulder into which the CFS measurement on bare CIS (dotted black line, fig. 30 b)) was fitted (black arrows) appears at different positions in the spectra.

The increased down-scaling needed to fit fig. 30 b) properly into the logarithmic plots along with the increase in the feature to the left of E-$E_{V,CdS} = 0$ (the CdS valence band) shows the growth of the CdS layer very clearly. Furthermore, the presence of the CdS signal at the same position in the spectra from the 1:00 minute and 4:00 minute samples confirms the fact that neither spectrum was mistakenly shifted during analysis, thereby producing the different band offsets.

The origin of the rise in intensity in the spectrum from the 1:00 minute CdS sample at 0.5 eV is not clear. Considering that this sample lies between the other two, any features of this spectrum should represent an intermediate state between the other two samples.

Because the results of the measurements on the CIS samples with 1:00 and 2:00 min-

utes CdS discussed here represent a substantial amount of the observations made in this chapter, they could be considered as possibly reliable results, especially because they are consistent with each other. However, the physical reasoning given above is enough to substantiate the claim that they are "failed" experiments and should for that reason be discounted. They are, however, not be overlooked as there may be explanations for the results beyond those discussed here which contain information about the CFS method and/or the CIS/CdS junction itself.

References

[1] R. Klenk, Thin Solid Films **387**, 135-140 (2001)

[2] S. Licht, B. Wang, S. Mukerji, T. Soga, M. Umeno, H. Tributsch, J. Phys. Chem. B. **104**, 8920-8924 (2004)

[3] H. Tributsch, B. Neumann, Inter. J. Hydrogen Energy **32**, 2679-2688 (2007)

[4] E. Weliczko, Home Power Magazine **127**, 98-101 (2008)

[5] J. Kaneshiro, N. Gaillard, R. Rocheleau, E. Miller, Solar Energy Materials and Solar Cells **94**, 12-16 (2010)

[6] T. Zdanowicz, T. Rodziewicz, M. Zabkowska-Waclawek, Solar Energy Materials and Solar Cells **87**, 757-769 (2005)

[7] A. Einstein, Annalen der Physik **17**, 132-148 (1905)

[8] D. Cahen, A. Kahn, Advanced Materials **15**, 271-277 (2003)

[9] Handbook of Surface and Interface Analysis: Methods for Problem-Solving, 2nd Ed., J. C. Riviere, S. Myhra, Ed., CRC Press, Boca Raton, Florida, USA (2009)

[10] Topics in Applied Physics: Photoemission in Solids, M. Cardona, L. Ley, Ed, Springer-Verlag, Berlin, Germany (1978)

[11] Practical Surface Analysis, D. Briggs, M. P. Seah, Ed., John Wiley & Sons, New York, New York, USA (1983)

[12] S. Tanuma, C. J. Powell, D. R. Penn, Surf. Inter. Anal. **21**, 165 (1993)

[13] M. Gorgoi, S. Svensson, F. Schäfers, G. Öhrwall, M. Mertin, P. Bressler, O. Karis, H. Siegbahn, A. Sandell, H. Rensmo, W. Doherty, C. Jung, W. Braun, W. Eberhardt, Nuclear Instruments and Methods in Physics Research Section A: Accelerators, Spectrometers, Detectors and Associated Equipment **601**, Issues 1-2, 48-53 (2009)

[14] A. Zangwill, *Physics at Surfaces*, Press Syndicate of the University of Cambridge (1988)

[15] M.B. Trzhaskovskaya, V.I. Nefedov, V.G. Yarzhemsky, Atomic Data and Nuclear Tables **77**, 97-159 (2001)

[16] D.P. Woodruf, Nuclear Instruments and Methods in Phys. Res. A **547**, 187-195 (2005)

[17] Lawrence Berkley Nation Laboratory website: http://www.lbl.gov

[18] M. Grioni, J.B. Goedkoop, R. Schoorl, F. M. F. de Groot, J.C. Fuggle, Phys. Rev. B **39**, 1541-1545 (1989)

[19] A. Nilsson, N. Mårtensson, Physica B **208 & 209**, 19-22 (1995)

[20] A. Nilsson, J. Stöhr, T. Wiell, M. Alden, P. Bennich, N. Wassdahl, M. G. Samant, S. S. P. Parkin, Phys. Rev. B,**54**, 2917-2921 (1996)

[21] R. Bacewicz, A. Wolska, K. Lawniczak-Jablonska, Ph. Sainctavit, J. Phys.: Condens. Matter **12**, 7371-7379 (2000)

[22] P. Fons, K. Sakurai, A. Yamada, K. Matsubara, K. Iwata, T. Baba, Y. Kimura, H. Nakanishi, S. Niki, J. Phys. Chem. Solids **64**, 1733-1735, (2003)

[23] FEFF Homepage and Documentation for FEFF8: http://leonardo.phys.washington.edu/feff/html/documentation.html

[24] B. Marsen, L. Steinkopf, H. Wilhelm, I. Lauermann, M. Gorgoi, H.-E. Mahnke, T. Unhold, R. Scheer, H.-W. Schock, J. Appl. Phys., submitted (2009)

[25] J. Wüsten, Diplomarbeit, Universitt Kaiserslautern, Germany, AG Prof. Dr. Ch. Ziegler (2003)

[26] L. Weinhardt, Diplomarbeit, Bayerische Julius-Maximilians-Universität, Würzburg, Germany, AG Prof. Dr. E. Umbach (2001)

[27] J. Reichardt, Diplomarbeit, Humbolt-Universität Berlin, Berlin, Germany, AG Prof. M.-Ch. Lux-Steiner (2003)

[28] Topics in Applied Physics: Photoemission in Solids II, L. Ley, M. Cordona, Ed., Springer-Verlag, Berlin, Germany (1979)

[29] Bessy website: http://www.bessy.de

[30] W. Schottky, Phys. Zeit. **31**, 913 (1930)

[31] W. Schottky, Naturwissenschaften **26**, 843 (1938)

[32] J. Wallmark, Proc. Inst. Radio Eng. **45**, 474, (1957)

[33] M. Marder, *Condensed Matter Physics*, John Wiley & Sons, Inc., New York, USA (2000)

[34] H.-J. Lewerenz, H. Jungblut, *Photovoltaik: Grundlagen und Anwendung*, Springer-Verlag, Berlin, (1995)

[35] H. Ibach, H. Lüth, *Festkörperphysik*, Springer Verlag, Berlin, Germany, (1999)

[36] *Electronic Structure of Semiconductor Heterojunctions*, G. Margaritondo, Ed., Kluwer Academic Publishers, Dordrecht, Holland (1988)

[37] A. van der Ziel, *Solid State Physical Electronics*, Prentice-Hall, Engelwood Cliffs (1957)

[38] N. F. Mott and R. W. Gurney, *Electronic Processes in Ionic Crystals*, Oxford University Press, New York (1940)

[39] W. Schottky, Zeits. f. Physik **118**, 539 (1941)

[40] H. A. Bethe, M.I.T. Radiation Laboratory Report 43-12 (November 23, 1942)

[41] H. Y. Fan, Phys. Rev. **62** (1942)

[42] R. Dingle, W. Wiegemann, C. H. Henry, Phys. Rev. Lett. **33**, 827-830 (1974)

[43] A. C. Gossard, IEEE J. of Quantum Electronics **QE-22** (1986)

[44] F. Capasso, K. Mohammed, A. Y. Cho, IEEE J. of Quantum Electronics **QE-22** (1986)

[45] A. D. Katnani, G. Margaritondo, Phys. Rev. B **28**, 1944-1956 (1983)

[46] M. Sebastiani, L. Di Gaspare, G. Capellini, C. Bittencourt, F. Evangelista, Phys. Rev. Lett. **75**, 3352-3355 (1995)

[47] R. L. Anderson, *Solid State Electronics*, Pergamon Press, Great Britain **5**, pp. 341-351 (1962)

[48] J. L. Freeouf, J. M. Woodall, Surface Science **168**, 518-530 (1986)

[49] B. K. Agrawal, S. Agrawal, R. Srivastava, P. Srivastava, Physica E **11**, 27-34 (2001)

[50] J. Tersoff, Phys. Rev. B **30**, 4874-4877 (1984)

[51] R. C. Miller, A. C. Gossard, D. A. Kleinman, O. Munteaunu, Phys. Rev. B **29** 3740-3743 (1984)

[52] S. H. Wei, A. Zunger, Phys. Rev. Lett. **59**, 144-147 (1987)

[53] S. J. Fonash, *Solar Cell Devices*, Academic Press, New York (1981)

[54] H. Dember, Physik. Z. **32** 554 (1931)

[55] W. W. Harvey, Surface Science **2**, 456-463 (1964)

[56] E. Lorenzo, *Solar Energy: Engineering of Photovoltaic Systems*, Progensa, Sevilla (1994)

[57] R. Scheer, Trends in Vacuum Science and Technology **2**, 77-112 (1997)

[58] S. Siemer, J. Klaer, I. Luck, J. Bruns, R. Klenk, D. Bräunig, Solar Energy Materials and Solar Cells **67**, 159-166 (2001)

[59] C. Kaufmann, T. Unold, D. Abou-Ras, J. Bundesmann, A. Neisser, R. Klenk, R. Scheer, K. Sakurai, H.-W. Schock, Thin Solid Films **515**, 6217-6221 (2007)

[60] J.L. Shay, B. Tell, H. M. Kasper, Appl. Phys. Lett. **19**, 366-368 (1971)

[61] S. Wagner, J.L. Shay, P. Migliorato, Appl. Phys. Lett. **25**, 434-435 (1974)

[62] D. Schmid, M. Ruckh, H. W. Schock, Solar Energy Materials and Solar Cells **41-42**, 281-294 (1996)

[63] R. Mainz, R. Klenk, M. Ch. Lux-Steiner, Thin Solid Films **515**, 5934-5937 (2007)

[64] Ch. von Klopmann, J. Djordjevic, E. Rudigier, R. Scheer, J. of Crystal Growth **289**, 121-133 (2006)

[65] S. C. Abrahams, J. L. Bernstein, J. Chem. Phys. **59**, 5415 (1973)

[66] S. Merdes, B. Johnson, R. Sáez-Araoz, A. Ennaoui, J. Klaer, I. Lauermann, R. Mainz, A. Meeder, R. Klenk, Proceedings of the 2009 MRS Spring Meeting, San Francisco, USA

[67] R. Klenk, S. Bakehe, R. Kaigawa, A. Neisser, J. Reiß, M.Ch. Lux-Steiner, Thin Solid Films **451-452**, 424-429 (2004)

[68] R. Klenk, J. Klaer, R. Scheer, M.Ch. Lux-Steiner, I. Luck, N. Meyer, U. Rhle, Thin Solid Films **480-481**, 509-514 (2005)

[69] M. Weber, R. Scheer, H. J. Lewerenz, H. Jungblut, U. Störkel, J. Electrochem. Soc. **149**, G77-G84 (2002)

[70] H. Metin, R. Esen, J. Crystal Growth **258**, 141-148 (2003)

[71] D. Abou-Ras, G. Kostorz, A. Romeo, D. Rudmann, A. N. Tiwari, Thin Solid Films **480-481**, 118-123

[72] V. Nadenau, D. Hariskos, H.-W. Schock, M. Krejci, F.-J. Haug, A. N. Tiwari, H. Zogg, G. Kostorz, J. Appl. Phys. **85**, 534-542 (1999)

[73] M. J. Furlong, M. Froment, M. C. Bernard, R. Cortès, A. N. Tiwari, M. Krejci, H. Zogg, D. Lincot, J. Crystal Growth **193**, 114-122 (1998)

[74] M. Weber, J. Krauser, A. Weidinger, J. Bruns, C.-H. Fischer, W. Bohne, J. Röhrlich, R. Scheer, J. Electrochem. Soc. **146**, 2131-2138 (1999)

[75] M. A. Contreras, M. J. Romero, B. To, F. Hasoon, R. Noufi, S. Ward, K. Ramanathan, Thin Solid Films **403**, 204-211 (2002)

[76] R. Hunger, M. V. Lebedev, K. Sakurai, T. Schulmeyer, Th. Mayer, A. Klein, S. Niki, W. Jaegermann, Thin Solid Films **515**, 6112-6118 (2007)

[77] K. Kushiya, H. Hakuma, H. Sano, A. Yamada, M. Konagai, Solar Energy Materials and Solar Cells **35**, 223-229 (1994)

[78] K. A. Jones, J Crystal Growth **47**, 235-244 (1979)

[79] T. Nakada, Thin Solid Films **361-362**, 346-352 (2000)

[80] A. Niemegeers, M. Burgelman, A. De Vos, Appl. Phys Lett. **67**, 843 (1995)

[81] A. Klein, T. Löher, Y. Tomm, C. Pettenkoffer, W. Jaegermann, Appl. Phys. Lett. **70**, 1299-1301 (1997)

[82] J.-F. Guillemoles, L. Kronik, D. Cahen, U. Rau, A. Jasenek, H.-W. Schock, J. Phys. Chem. B **104**, 4849-4862

[83] K. Ramanathan, H. Wiesner, S. Asher, D. Niles, R. N. Battacharya, M. A. Contreras, R. Noufi, Proc. 2nd World Conf. Photovoltaic Solar Energy Conversion, 477 (1998)

[84] T. Wada, S. Hayashi, Y. Hashimoto, S. Nishiwaki, T. Sato, T. Negami, M. Nishitani, Proc. 2nd World Conf. Photovoltaic Solar Energy Conversion, 403 (1998)

[85] M. Bär, Dissertation, Technische Universität zu Berlin (2003)

[86] M. Kostoglou, N. Andritsos, A.J. Karabelas, J. of Colloid and Interface Science **263**, 177-189 (2003)

[87] A. Rockett, D. Liao, J. T. Heath, J. D. Cohen, Y. M. Strzhemechny, L. J. Brillson, K. Ramanathan, W. N. Shafarman, Thin Solid Films **431-432**, 301-306 (2003)

[88] K. Fukuzaki, S. Kohiki, H. Yoshikawa, S. Fukushima, T. Watanabe, I. Kojima, Appl. Phys. Lett. **73**, 1385-1387 (1998)

[89] T. Yamamoto, I. Luck, R. Scheer, App. Surf. Sci. **159**, 350-354 (2000)

[90] N. G. Dhere, A. A. Kadam, A. H. Jahagirdar, S. S. Kulkarni, L. Weinhardt, D. Groß, C. Heske, E. Umbach, J. Phys. and Chem. of Solids **66**, 1872-1875 (2005)

[91] H. Mönig, Dissertation, Helmholtz-Zentrum Berlin für Matrialien und Energy, (2009)

[92] H. Mönig, Ch.-H. Fischer, A. Grimm, B. Johnson, C. A. Kaufmann, R. Caballero, I. Lauermann, M. Ch. Lux-Steiner, J. Appl. Phys. **107**, 1 (2010)

[93] H. Mönig, I. Lauermann, A. Grimm, C. Camus, C. A. Kaufmann, P. Pistor, Ch. Jung, T. Kropp, M. C. Lux-Steiner, Ch.-H. Fischer, Appl. Surface Science **255**, 2474-2477 (2008)

[94] S. B. Zhang, S.-H. Wei, A. Zunger, Phys. Rev. B. **57**, 9642-9656 (1998)

[95] Y.-J. Zhou, C. Persson, S. Lany, A. Zunger, App. Phys. Lett. **85**, 5860-5862 (2004)

[96] I. Lauermann, Ch. Loreck, A. Grimm, R. Klenk, H. Mönig, M. Ch. Lux-Steiner, Ch.-H. Fischer, S. Visbeck, T. P. Niesen, Thin Solid Films **515** 6015-6019 (2007)

[97] S.-H. Wei, A. Zunger, Phys. Rev. B **37**, 8958-8981 (1988)

[98] K. Okamoto, S. Kawai, R. Kiriyama, Jap. J. Appl. Phys. **8**, 718-724 (1969)

[99] H. Nozaki, K. Shibata, N. Ohhashi, J. Solid State Chem. **91**, 306-311 1991

[100] Y. Hashimoto, K. Takeuchi, K. Ito, Appl. Phys. Lett. **67**, 980-982 (1995)

[101] R. Scheer, I. Luck, H. J. Lewerenz, Proceedings of the 12th European Photovoltaic Solar Energy Conference, Amsterdam, the Netherlands, pg. 1751 (1994)

[102] R. Scheer, R. Klenk, J. Klaer, I. Luck, Solar Energy **77**, 777-784 (2004)

[103] P. E. Lippens, M. Lannoo, Phys. Rev. B **39**, 10935-10942 (1989)

[104] S. Wei, A. Zunger, J. Appl. Phys. **78**, 3846-3856 (1995)

[105] T. Yamamoto, H. Katayama-Yoshida, Jap. J. Appl. Phys. **35**, L 1562-L 1565 (1996)

[106] J. Lüning, J. Rockenberger, S. Eisebitt, J.-E. Rubensson, A. Karl, A. Kornowski, H. Weller, W. Eberhardt, Solid State Comm. **112**, 5-9 (1999)

[107] L. Weinhardt, O. Fuchs, D. Groß, G. Storch, E. Umbach, N. G. Dhere, A. A. Kadam, S. S. Kulkarni, C. Heske, Appl. Phys. Lett. **86**, 062109-062111 (2005)

[108] C. L. Perkins, F. S. Hasoon, H. A. Al-Thani, S. E. Asher, P. Sheldon, Proceedings from the 31st IEEE Photovoltaic Specialists Conference and Exhibition, Lake Buena Vista, Florida, USA, Pub. IEEE Operations Center, Piscataway, New Jersey, USA (2005)

[109] R. Hunger, T. Schulmeyer, M. Lebedev, A. Klein, W. Jaegermann, R. Kniese, M. Powalla, K. Sakurai, S. Niki, Thin Solid Films **515**, 6112-6118 (2007)

[110] Y. Ogawa, S. Uenishi, K. Tohyama, K. Ito, Solar Energy Materials and Solar Cells **35**, 157-163 (1994)

[111] Y.B. He, T. Krämer, I. Österreicher, A. Polity, B.K. Meyer, M. Hardt, Semicon. Sci. and Technol. **20**, 685-692 (2005)

[112] K. Winer, L. Ley, Phys. Rev. B **36**, 6072-6077 (1987)

[113] M. Schmidt, A. Schoepke, L. Korte, O. Milch, J. Fuhs, Non-Cryst. Solids **338-340**, 211-214 (2004)

[114] L. Korte, A. Laades, A. Schmidt, J. Non-Cryst. Solids **352**, 1217-1220 (2006)

[115] L. Korte, M. Schmidt, J. Non-Cryst. Solids **354**, 2138-2143 (2008)

[116] M. Schmidt, L. Korte, A. Laades, R. Stangl, Ch. Schubert, H. Angermann, E. Conrad, K. v. Maydell, Thin Solid Films **515**, 7475-7480 (2007)

[117] M. Bär, A. Ennaoui, J. Klaer, R. Sáez-Araoz, T. Kropp, L. Weinhardt, C. Heske, H.-W. Schock, Ch.-H. Fischer, M.C. Lux-Steiner, Chem. Phys. Lett. **433**, 71-74 (2006)

[118] P. Pistor, R. Klenk, Proceedings of NUMOS (Numerical Modelling of Thin Film Solar Cells), Gent, Belgium, pg. 28-30, (2007)

[119] R. Klenk, J. Klaer, R. Scheer, M.Ch. Lux-Steiner, I. Luck, N. Meyer, U. Rühle, Thin Solid Films **480-481** 509-514 (2005)

[120] A. Ennaoui, M. Bär, J. Klaer, T. Kropp, R. Sáez-Araoz, M.Ch. Lux-Steiner, Progress in Photovoltaics **14**, 499-511 (2006)

[121] T. Schulmeyer, R. Kniese, R. Hunger, W. Jaegermann, M. Powalla, A. Klein, Thin Solid Films **451**, 420-423 (2004)

[122] A. Vollmer, Helmholtz-Zentrum Berlin, Private Communication (2009)

[123] T. Abe, S. Kohiki, K. Fukuzaki, M. Oku, T. Watanabe, Appl. Surface Science **174**, 40-42 (2001)

[124] NIST XPS Database: http://srdata.nist.gov

[125] J. E. Jaffe, A. Zunger, Phys. Rev. B **28**, 5822-5847 (1983)

[126] D. Schmid, M. Ruckh, F. Grunwald, H. W. Schock, J. Appl. Phys. **73**, 2902 (1993)

[127] R. J. Beerends, H. G. ter Morsche, J. C. van den Berg, E. M. van de Vrie, *Fourier and Laplace Transfroms*, Cambridge University Press (2003)

[128] I. Konovalov, L. Makhova, J. Appl. Physics **103**, 093721 (2008)

[129] I. Konovalov, R. Szargan, Appl. Phys. Lett **82**, 2088 (2003)

[130] http://mathworld.wolfram.com/Convolution.html

[131] P. A. Jackson, *Deconvolution*, Academic Press, Inc., Orlando (1984)

[132] J. J. Olivero, R. L. Longbothum, J. Quant. Spectrosc. Radiat. Transfer **17**, 233-236 (1977)

[133] R. Hesse, T. Chassé, R. Szargan, Fresnius J. Anal. Chem. **365**, 48-54, (1999)

[134] W. Jägermann, C. Pettenkofer, B. A. Parkinson, Phys. Rev. B **42** 7487-7496 (1990)

[135] A. Schellenberger, R. Schlaf, C. Pettenkoffer, W. Jaegermann, Phys. Rev. B **45** 3538-3545 (1992)

[136] A. Schellenberger, Dissertation, Freie Universität zu Berlin (1992)

[137] B. Gyorffy, Phys. Rev. B **5**, 2382 (1972)

[138] W. H. Butler, Phys. Rev. B **31**, 3260 (1985)

[139] H. Ebert, M. Battocletti, Solid State Comm. **98**, 785 (1996)

[140] S. H. Vosko, L. Wilk, M. Nusair, Canad. J. Phys. **58**, 1200 (1980)

Danksagung

Viele haben mir geholfen (manche freiwillig, manche gezwungenermaßen) in den letzten drei Jahren diese Arbeit erfolgreich abzuschließen.

Es liegt an Euch, dass ich diese Erfahrung nicht nur für einen Doktoranden relativ stressfrei gemacht habe, aber auch, dass ich meistens großen Spaß an der Sache hatte.

Besonders zu danken habe ich im einzelnen:

Alte und neue CISSY-Gruppenmitglieder: bei Euch ist man schlichtweg gut untergebracht. Als Doktorand hört man immer sehr viele Horrorgeschichten und ich weiß immer noch nicht warum. Die erlebt man bei Euch einfach nicht.

Alte und neue Mitglieder der Pettenkoffer Gruppe, insbesondere Christian, Carsten, Eike und Andreas: für die hilfreichen Gespräche. Spektroskopiker, die an CIS arbeiten, sind seltene Tiere.

KD-CIS Projekt: für die finanzielle Unterstützung und die Treffen, bei denen ich immer sehr viel gelernt habe.

Lars Korte: für die Zusammenarbeit bei den Bandoffsetmessungen, zu denen Du sehr viel beigetragen hast. Dies hat unter anderem zu einer Veröffentlichung und einem ganzen Kapitel meiner Arbeit geführt.

Antje Vollmer: für die Betreuung während der Strahlzeiten an der SurICat und für die guten wissenschaftlichen Ratschläge. Davon habe ich auch ein schönes Kapitel in meiner Arbeit.

Jo Klaer: für die endlosen Reihen von Proben, die ich brauchte und von Dir bekommen habe. Da geht die Arbeit immer besser voran, wenn man mit was Gutem anfängt.

Martha Lux-Steiner: für die Chance, meine Arbeit bei Ihnen anzufertigen trotz schlechter Note in Experimentalphysik. Über das Leben habe ich auch einiges gelernt.

Harry Mönig: dafür, dass ich mindestens eine Zeit lang einen richtigen Mitstreiter hatte. Wir hatten viele Gespräche, die uns beide vorangebracht haben. Yes We Can!!

Alex Grimm: Bürounterhaltung erster Klasse, Alter! Mein Alltag war oft einfach ein Genuss. Ahoi! Dazu hast Du die CISSY immer instand gehalten (auch wenn ich was kaputt gemacht habe), was natürlich unschätzbar ist.

Christian-Herbert Fischer: für die Betreuung und Unterstützung. Wenn Du ein Ergebniss gut gefunden hast, hat es mir immer Mut gemacht. Ich wusste dann immer, ein erfahrener Wissenschaftler hatte das Ergebnis schon ein Mal gesehen.

Iver Lauermann: Was soll ich hier sagen? Jedes mal, als ich eine der obengenannten Horrorgeschichten gehört habe, musste ich einfach den Mund halten: ich wusste wie gut ich es hatte. Ich war stets Mitarbeiter bei Dir und nicht nur Doktorand. Jeder sollte eigentlich ein Mal die Gelegenheit haben zu wissen wie das ist.

Mirtha, Charlie, Julia, Pati, Frauke, Maπ, Scott, Jake, Serge: near or far away, thanks for the support. It was a vital ingredient.

Adam: thanks for blazing the way and having to try everything out first. That always made my life easier.

Mom and Dad: thanks for supporting me in all my endeavors, whether they were weird or normal. It has brought me a long way. You only get allotted one mom and one dad, and i got the right one both times.

Publications

The following results contained in this thesis have been published:

B. Johnson, L. Korte, T. Lußky, J. Klaer, I. Lauermann, J. Appl. Phys. **106** 073712 (2009)

The following publications were completed during work on this thesis with other collaborators in similar areas and are not contained in this thesis:

P. Pistor, N. Allsop, W. Braun, R. Caballera, C. Camus, Ch-H. Fischer, M. Gorgoi, A. Grimm, B. Johnson, T. Kropp, I. Lauermann, S. Lehmann, H. Mönig, S. Schorr, A. Weber, R. Klenk, Phys. Status Solidi A **206** 1059-1062 (2009)

S. Merdes, B. Johnson, R. R. Sáez-Araoz, A. Ennaoui, J. Klaer, I. Lauermann, R. Mainz, A. Meder, R. Klenk, Proceedings from the 2009 MRS Spring Meeting, San Francisco, USA

H. Mönig, Ch.H. Fischer, A. Grimm, B. Johnson, C. A. Kaufmann, R. Caballero, I. Lauermann, M. Ch. Lux-Steiner, J. Appl. Phys., **107**, 1 (2010)

The following posters containing results from this thesis have been presented at conferences:

B. Johnson, I. Lauermann, H. Mönig, A. Grimm, T. Kropp, S. Merdes, A. Volmer, C.-H. Fischer, NEXAFS Study of the Effect of Ga on the Conduction Band Edge in Cu(In,Ga)S_2, 2009 E-MRS Spring Meeting, Strasbourg, France

B. Johnson, L. Korte, T. Lußky, J. Klaer, I. Lauermann, Investigation of the Electronic Structure of the $CuInS_2$/CdS Heterojunction Using Near-UV Constant Final State Photoelectron Spectroscopy, 24th EU PVSEC, Hamburg, Germany (2009)

B. Johnson, I. Lauermann, J. Klaer, A. Volmer, C.-H. Fischer, Cd and Cu Diffusion in the $CuInS_2$/CdS Heterojunction formed with Chemical Bath Deposition, 2010 E-MRS Spring Meeting, Strasbourg, France

I declare that i have written this thesis with my own hand without the help of unallowed outside sources. All passages containing results from other works have been cited as such.

Benjamin Johnson

Berlin−June 3, 2010